Predicting the Pit-to-Crack Transition of Offshore Wind Turbine Foundations

A mechanistic determination

J.D. Rodenburg

Technische Universiteit Delft

Predicting the Pit-to-Crack Transition of Offshore Wind Turbine Foundations

A mechanistic determination

by

J.D. Rodenburg

to obtain the degree of Master of Science
at the Delft University of Technology,
to be defended publicly on Thursday July 9, 2020 at 2:00 PM.

Student number:	4369122	
Project duration:	October 1, 2019 – July 9, 2020	
Thesis committee:	Prof. ir. J.J. Hopman,	TU Delft, chairman
	Dr. ir. J.H. den Besten,	TU Delft, supervisor
	Dr. ir. R.J.M. Pijpers,	TNO, supervisor
	Ir. R. Dekker,	TU Delft, mentor
	Dr. C.L. Walters	TU Delft

Abstract

The number of wind farms is rising, and is expected to keep rising in the coming years to reach the nearing climate goals. More and more wind farms are built offshore, where the wind turbines have to persist harsh environmental conditions. One of the environmental processes that foundations of offshore wind turbines have to persist, is corrosion. Corrosion is the spontaneous degradation of material due to chemical, biochemical, and electrochemical interaction between metals and alloys and the environment. One of the most dangerous forms of corrosion is pitting corrosion, because it is hard to predict, it is hard to detect, and it can lead to failure of a structure in combination with a mechanical load due to a minimal weight loss. Pitting corrosion acts locally and results in a small defect (pit) at the surface of a metal or alloy. The combination of pitting corrosion and a fatigue load is called corrosion fatigue, and should be taken into account in design and maintenance studies of offshore wind turbine foundations.

The current knowledge on corrosion fatigue is insufficient to accurately implement fatigue life predictions of structures in free corrosion conditions in engineering solutions. Especially the transition from a corrosion pit to a fatigue crack, which is also the transition from a corrosion dominated (time-dependent) process, to a fatigue dominated (cycles-dependent) process, is relatively unknown. This results in an uncertain prediction of the structural life of offshore wind turbines, and could result in the application of excessive mitigation techniques, or the dismantling of offshore wind turbines before the end of its structural life.

In this research study, a combined analytical/numerical model is presented that implements mechanisms of both the fatigue, and the corrosion process to determine the moment in time and location in the corrosion pit of the pit-to-crack transition. The hypothesis used to build the model, is that the pit-to-crack transition occurs at the moment that a fatigue crack initiates. Assumptions are made to be able to predict the level of stress and strain at the surface and below the surface of a corrosion pit using a FEM model. Using the stress and strain levels, damage is accumulated until the failure criterion is reached, i.e. when a fatigue crack will initiate. In this research study, elliptical pit shapes are considered, with and without a certain roughness at the surface of the corrosion pit.

From the results it is found that a more sharp shaped corrosion pit is a more favourable location for fatigue crack initiation, than a more blunt shaped corrosion pit. The number of cycles to fatigue crack initiation resulting from the developed model are higher, than the number of cycles to failure found by the DNV GL B1 SN-curve for free corrosion conditions. Also, the DNV GL SN-curve is more steep, than a fitted curve through the data points resulting from the developed model. Through a sensitivity study and by considering the number of assumptions and simplifications made in this research study, it is concluded that the spread and uncertainty of the outcome of the developed model is too large to be able to draw conclusions based on the comparison between the results and the DNV GL SN-curves. More research on the input parameters of the developed model will give more certainty and a better validity to the model. It is found that the effect of surface roughness to the fatigue crack initiation life is not substantial, because it affects the stress and strain levels only up to a relatively small depth. The location of fatigue crack initiation is in the pit bottom for blunt shaped corrosion pits ($AR_\mathrm{p} < 0.5$), and in the pit wall for sharp shaped corrosion pits ($AR_\mathrm{p} > 0.5$). For circular shaped corrosion pits, the difference between the fatigue crack initiation life at the pit wall and the pit bottom is negligible.

It is concluded that the model gives a comprehensive basis for the prediction of the pit-to-crack transition, but more (experimental) research on the input parameters will be necessary to be able to give a substantiated estimate of structural life of offshore wind turbine foundations.

Acknowledgements

This thesis on the prediction of the pit-to-crack transition of offshore wind turbine foundations has been written for the fulfilment of the Master of Science degree in Marine Technology at the Delft University of Technology. The research has been performed in collaboration with research institute TNO, at the department Structural Reliability in Delft.

During the last nine months I have acquired knowledge of the corrosion and fatigue processes, but also of the process of setting up, and managing a research study. Acquiring these skills would not have been possible without my supervisors and committee members, whom I all owe lots of thanks.

First, I would like to show my appreciation to Dr. Ir. Richard Pijpers (TNO), who has been my daily supervisor. With a great deal of knowledge on the technical aspects of this research work, and the processes involved with doing research, I have learned a lot from you. By involving me in the project this thesis is part of, and your enthusiasm about this topic and the work you do, you have inspired and motivated me to perform this research study, and to continue in this line of field afterwards. I first came into contact with the topic of fatigue due to a course of Dr. Ir. Henk den Besten (TU Delft, 3mE). Your never-ending, whilst enthusiastically brought flow of information on the topic of fatigue during this course has awaken an interest in this topic in me, and has inspired me to acquire more knowledge in this line of field. By asking critical, sharp questions, you have always pushed me to think about everything I say or write down, which has helped a lot to guarantee the quality of this thesis. Because I started these nine months with even less knowledge of the corrosion part than the fatigue part of corrosion fatigue, I am glad that Ir. Richard Dekker (TU Delft, CiTG) was willing to help me to get started on this topic. While I was busy figuring out what would be the scope of this thesis, we have had some meetings in which you asked me the right questions which helped me to get to a thesis subject which interested me, and was an addition to science. Last but not least, I would like to thank the two latest additions to the committee, Dr. Carey Walters (TU Delft, 3mE), and Prof. Ir. Hans Hopman (TU Delft, 3mE) for their interest in my thesis, and sharing their in-depth knowledge.

Next to my graduation committee, I would like to thank Richard Pijpers' colleagues of the 'staalteam' at TNO, who have given me a warm welcome. Special thanks go to Ir. Sjoerd Hengeveld (TNO), who made me enthusiastic about doing my master thesis research at TNO, and with whom I have had some valuable moments 'sparring' about my research. Furthermore, I would like to thank my family and friends for being there for me. Sport breaks, coffee (tea for me) breaks, walking breaks, all were very much appreciated. It is most important for me to thank my lovely Simone, who has been there for me at all times. You had to listen to me talking about topics that are not of your interest or knowledge, but you have always tried to stay focussed (awake) and ask questions. Being around you made and still makes me feel happy. Luckily I can give it all back to you when you start your thesis.

I hope you all enjoy reading this research report.

J.D. Rodenburg
Delft, June 2020

Contents

Nomenclature

α	Back stress	MPa
ϵ	Strain	mm/mm
ϵ_0	Onset of strain hardening	mm/mm
ϵ_a	Strain amplitude	mm/mm
$\epsilon_\mathrm{a}^\mathrm{e}$	Elastic strain amplitude	mm/mm
$\epsilon_\mathrm{a}^\mathrm{p}$	Plastic strain amplitude	mm/mm
ϵ_f'	Fatigue ductility coefficient	-
γ	Rate of change in kinematic hardeing factor	-
ν	Poisson's ratio	-
ρ	Density	kg/m^2
σ	Stress	MPa
σ_0	Change in size of the yield surface	MPa
σ_f'	Fatigue strength coefficient	MPa
σ_max	Maximum stress in a loading cycle	MPa
σ_nom	Nominal or applied stress	MPa
a	Corrosion pit depth	mm
a_micro	Micro-pit depth	mm
AR_p	Pit aspect ratio $\left(\frac{\mathrm{a}}{2\mathrm{c}}\right)$	-
b	Fatigue strength exponent	-
b	Rate in yield surface change	-
C	Initial kinematic hardening factor	-
c	Corrosion pit width (radius)	mm
c	Fatigue ductility exponent	-
D	Fatigue damage	-
E	Young's modulus	MPa
E_0	Electrode potential	V
F	Faraday constant	$9.65{\cdot}10^4$ C/mol
I	Anodic current	A
i	Current density	A/m^2
K	Stress intensity factor	MPa m$^{1/2}$

K'	Cyclic strength coefficient	MPa
K_{T}	Stress concentration factor (SCF)	-
l	Crack length	mm
m	Atomic mass	kg
n	Cyclic strain hardening exponent	-
N_{f}	Total fatigue lifetime	-
N_{i}	Fatigue crack initiation lifetime	-
Q_{∞}	Maximum change in yield surface size	MPa
R	Gas constant	8.3145 J/k/mol
R	Stress ratio	-
r	Corrosion rate	mm/yr
T	Temperature	°C
t	Time	s
V_{m}	Molar volume	m^3/mol

1

Introduction

1.1. General background

During the last decade, society has become aware of a nearing energy transition due to the rising attention for climate change. Fossil fuels (coal, oil and gas) are polluting and their reserves finite. More and more energy needs to be generated to fulfil society's rising demand for electricity to propel ships, drive cars, trucks and bicycles, heat houses, and feed the rising amount of electrical devices. Due to global warming, the transition from polluting energy generation plants using coal, oil, and gas, to renewable energy sources, is high on the political agenda. Therefore, the demand for so called greener energy generation methods like solar and wind power is high, which can be seen from the growing capacity of these energy generation methods in the European Union in figure 1.1. Of this amount of wind energy capacity, the capacity of offshore wind energy generation in Europe is rising, as can be seen from figure 1.2. Due to their large surface, oceans are a preferable location for wind turbines, but they are a hazardous environment as well. Loading due to waves, currents and harsh weather create challenges in the design of offshore wind turbines. Another challenge is the impact of the aggressive corrosive environment of the salt seawater on the foundations of offshore wind turbines. Current offshore wind farms are mostly built in shallow waters, and consist of either a monopile, tripod or a jacket foundation which is either drilled or grouted into the sea bed depending on the soil configuration, see figure 1.3. Wind turbines and their foundations are typically built to last up to 25 years in sea. Therefore, in the design of wind turbines, environmental degradation needs to be taken into account in calculations of the lifetime of the structure. Structural life calculations of steel structures consist of fatigue calculations, which determine lifetime until failure of a structure due to the growth of cracks caused by a cyclic stress. For design studies, this can result in an increase of member size or choosing mitigation measures.

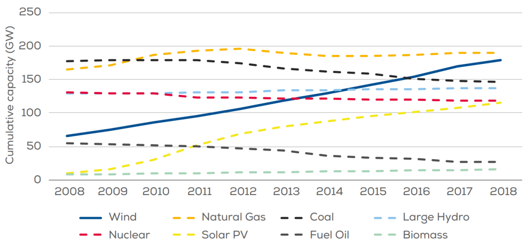

Figure 1.1: Total power generation capacity in the European Union 2008-2018 [1]

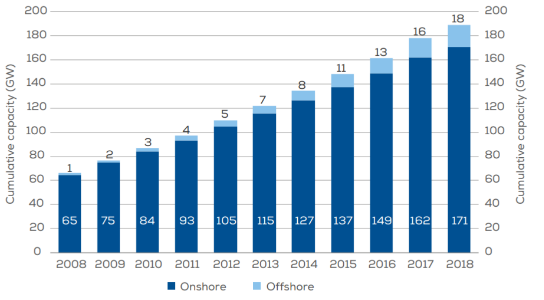

Figure 1.2: Cumulative onshore and offshore wind installations in the European Union [2]

Corrosion is a chemical process that acts synergetic in combination with structural stress as a degradation mechanism. This phenomenon has come under attention of society in the last decades due to severe incidents. A few examples are given below [4]:

- December 15, 1967, bridge over the Ohio river collapsed resulting in the loss of 46 lives and 11 people seriously injured. The cause for the collapse was found to be stress corrosion cracking.

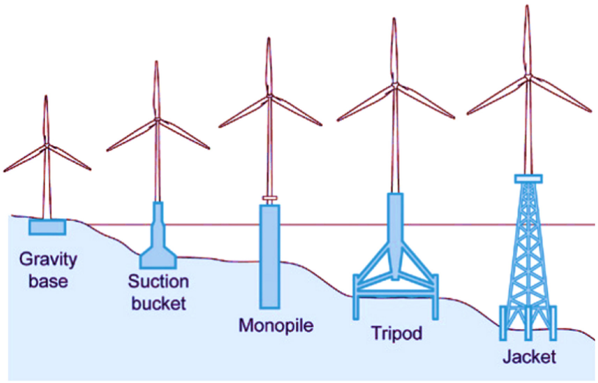

Figure 1.3: Wind turbine foundation types [3]

- April 28, 1988, aircraft crash in Hawaii resulting in the loss of 1 live and 65 people injured. Due to corrosion, cracking occurred resulting in a large segment of the upper fuselage of the aircraft being torn off while airborne.
- April 10, 1992, aircraft crash in the Bijlmer area in Amsterdam resulting in the loss of 43 lives. A corrosion pit in combination with fatigue loading caused an internal safety pin in one of the engines of the aircraft to fracture, separating one of the engines and hitting another engine.
- December 12, 1999, sinking of a tanker on the coast of France resulting in an oil spill creating an environmental disaster. Significant corrosion of the internal structure of the vessel was found.
- August 9, 2000, explosion of a gas pipeline in New Mexico resulting in the loss of 12 lives. Gas was released due to damage in the gas pipeline which was found to be caused by corrosion.
- May 19, 2015, oil spill in California, USA, from a crude oil pipeline. The wall thickness of the pipeline was found to be reduced by 45% due to corrosion. As a result cracks propagated in the pipeline wall.

All of these incidents contributed to the rising amount of attention and therefore research in the topic of corrosion and corrosion fatigue.

1.2. Problem description

Degradation of material due to corrosion is a worldwide problem, and has an economic impact on not only the offshore wind market. Kruger [5] found, based on research done for several countries, that the total cost of repairs, maintenance, and prevention works due to metallic corrosion is 3-5% of the Gross National Product of countries. These figures proof that it is important that the complete corrosion process is well understood. This includes the interaction with other degradation mechanisms, such as fatigue. Currently, in design and maintenance studies, assumptions are made in calculations regarding corrosion, which could be either underestimating, or overestimating the effect of corrosion. For a market as the offshore wind industry, which is increasing in size and capital, it is therefore of great importance to know what the effect of corrosion fatigue on the lifetime of the structures is.

Roughly two relevant types of corrosion can be identified for typical offshore wind turbine foundations: (i) localized corrosion, and (ii) global corrosion. Global corrosion is also called uniform corrosion and acts over the complete surface of a structure that is in contact with a corrosive environment. Uniform corrosion rates are relatively well-known and are relatively easy to implement in design studies of structures. Localized corrosion only acts on a small scale. A type of localized corrosion is pitting corrosion, which can result in small holes or pits in the surface of a material in the order of several millimetres. This type of corrosion is unpredictable in shape and size, and is hard to detect. Pitting corrosion is particularly dangerous in combination with stress, because the pit acts as a stress concentrator. When this stress is a cyclic stress, fatigue cracks can be initiated at the pit surface. This interaction can make a structure fail although only a minimal weight loss has occurred.

Fatigue is, just as corrosion, an established research field on its own. Fatigue lifetime can roughly be divided into two phases: (i) crack initiation life, and (ii) crack propagation life. The two phases combined represent the fatigue lifetime until failure of a structure. The interaction of the two degradation mechanisms acting at the same time can be seen as a competition. At a certain moment in time, a fatigue crack will initiate and propagate faster than the pit is expanding. This moment is called the pit-to-crack transition.

Because many parameters are involved in the combined corrosion fatigue process, it is hard to detect the influence of each parameter, which is required to understand the complete process. Therefore, it is of importance to split up the complete process into smaller parts. To split up the corrosion fatigue process into a corrosion dominant part, and a fatigue dominant part, it is of essence to be able to determine the pit-to-crack transition.

Determining the pit-to-crack transition experimentally for realistic conditions is challenging, because corrosion pit growth is time-dependent, while fatigue crack initiation is cycles-dependent. It is fairly possible to speed up the fatigue process by a higher load frequency, but it is more difficult to speed up the corrosion process in a realistic way. Most numerical or analytic corrosion fatigue models that are available in literature, do not implement a pit-to-crack transition, but regard the corrosion fatigue process as one process. Models that consider the pit-to-crack transition make assumptions that simplify the process in such a way, that it typically does not result in a usable outcome.

1.3. Scope of work

This study focusses on the prediction of the transition from a corrosion pit into a fatigue crack in a steel structure in a corrosive environment. Both the location of the transition in the corrosion pit, and the moment of the transition in time will be studied. A model will be created that is a combination of numerical and analytical models. In the end the results of the model will be compared to the method of corrosion fatigue life prediction implemented by standards used for designing wind turbine foundations.

This study will determine the pit-to-crack transition from a mechanistic point of view. The hypothesis is that the location and moment in time of the pit-to-crack transition is equal to the location and moment in time of fatigue crack initiation in the corrosion pit, and that fatigue crack initiation life and location can be determined using the accumulation of damage at and below the surface of a corrosion pit.

An extensive study on the parameters of importance to the pit-to-crack transition based on this hypothesis, and the choice and comparison of sources for these parameters will be performed. This includes a sensitivity study to determine the extent in which the parameters influence the pit-to-crack transition results.

Damage is accumulated based on the history of strain and stress in the material. It is expected that the corrosion process influences the stress-strain behaviour of a material resulting in a more brittle material due to hydrogen absorption, but due to the lack of data this is not implemented in this study. Using the strain-life method, which couples strain and stress in the material to a life prediction, the damage can be determined. The influence of the corrosion process on this method is available in literature, and therefore taken into account in the pit-to-crack transition model.

Stress and strain in the material will be determined using numerical models in Abaqus Finite Element Analysis (FEA), which allows Python scripting so parametric studies can be performed efficiently. The results will be analysed and mathematical descriptions of the results will be defined so that correlations can be found between them. This way less numerical models have to be created, which saves up computational time and makes the model easier to use in engineering solutions.

Ideally, this model is or can be coupled to a pit growth model to model the simultaneous occurrence of corrosion pit growth and fatigue crack initiation, but this study will not go into detail of the chemical aspects of the pitting corrosion process. Assumptions will be made on the pit growth rate and shape based on literature. Primarily, fatigue crack initiation life and location will be determined of perfectly elliptical shaped pits. Later, irregularities will be added to the elliptical pit surface to determine its effect on the fatigue crack initiation life and location.

1.4. Thesis organisation

This thesis is built up from five chapters after this introduction.

- Chapter 2 shows a review of the state-of-the-art and background of corrosion, fatigue and corrosion fatigue. Current methods to predict corrosion fatigue life and the pit-to-crack transition are discussed. A special emphasis is given to the corrosion and fatigue methods implemented in this study.

- Chapter 3 shows the implementation of the pitting corrosion fatigue model. First, the input parameters are given and discussed. Next, the used corrosion and fatigue modelling methods are discussed, which are summarized into a pit growth model, a Finite Element Method (FEM) model, and a damage accumulation model. The chapter discusses the verification of the FEM model as well.

- Chapter 4 presents the pit-to-crack transition results of the developed corrosion fatigue model for two cases. The pit-to-crack transition has been determined for perfectly elliptic pits growing while subjected to an elastic cyclic loading, and for an elasto-plastic fatigue loading. For each case, the stress and strain distribution at the surface of the corrosion pit and below the surface of the corrosion pit will be discussed.
- Chapter 5 presents the pit-to-crack transition results of the developed corrosion fatigue model for perfectly elliptic corrosion pits including a certain surface roughness. The influence of surface roughness on the fatigue crack initiation life and location is discussed.
- Chapter 6 elaborates on the extent of influence of the input parameters on the corrosion fatigue model through a sensitivity study.
- Chapter 7 presents the conclusions of this research work and summarizes recommendations for future work. A brief reflection on the goals of this study will be given in this chapter.

2

Background and literature review

Chapter 2 reviews the state-of-the-art of current research and knowledge on the subject of corrosion fatigue and the pit-to-crack transition. To fully understand the driving mechanisms of the pit-to-crack transition, both the corrosion process and fatigue process are studied.

2.1. Corrosion

Popov [6] defined corrosion as '*the spontaneous destruction of metals and alloys caused by chemical, biochemical, and electrochemical interaction between metals and alloys and the environment*'.

In this section, the corrosion process will be reviewed, first in a general way from the chemical point of view, later a comparison between different types of corrosion is made.

2.1.1. Chemical process

Corrosion is an electrochemical reaction, which means that two half-cell reactions are needed for corrosion to occur. In one of the two half-cell reactions, electrons are the product of the reaction. This is called an anodic reaction, and in corrosion science this is called the oxidation reaction. In this reaction the loss of metal-ions occurs. Structural steel is used for wind turbine foundations. The most common grade in wind turbine foundations is hot rolled S355 [7], also indicated as S355J, S355JO or S355J2, and fabricated according to the standard NEN-EN 10025-2 [8]. For the main component of steel, the oxidation half-cell reaction is given in equation (2.1).

$$\textbf{Anodic side} \qquad \mathrm{Fe(s)} \rightarrow \mathrm{Fe^{2+}(aq)} + 2\mathrm{e^-} \tag{2.1}$$

For the other half-cell reaction, electrons are reactants of the reaction. This is called a cathodic reaction, and in corrosion science this is called the reduction reaction. In seawater, equation (2.2) to equation (2.4) are most common to occur.

$$\mathrm{2H^+ + 2e^- \rightarrow H_2} \tag{2.2}$$

$$\textbf{Cathodic side} \qquad \mathrm{2H_2O + O_2 + 4e^- \rightarrow 4OH^-} \tag{2.3}$$

$$\mathrm{4H^+ + O_2 + 4e^- \rightarrow 2H_2O} \tag{2.4}$$

It is also possible, if another metal is in the vicinity of the anodic reaction, that the other metal acts as the cathode. For a given metal-ion M, with a given number of protons z, a reaction with n electrons can take place according to equation (2.5).

$$\mathrm{M}^{z+} + n\mathrm{e}^- \rightarrow \mathrm{M}^{(z-n)+} \tag{2.5}$$

Which half-cell reaction will act as the cathodic reaction depends on the standard electrode potential (E_0) of the reaction. The half-cell reaction with the lowest value of E_0 will act as the cathode most easily.

Next to the anodic and cathodic reaction, two other components need to be present for corrosion to occur: (i) a metallic path that provides passage for electrons between the anode and the cathode, and (ii) an electrolyte, which is a non-metallic substance that provides medium for the passage of charge carriers. In equation (2.6) the most common total chemical reaction of corrosion of a steel can be found. Occasionally, chloride (Cl^-) ions are included in this equation because chloride accelerates the corrosion process. In figure 2.1 a visualisation of the path of ions and electrons for corrosion in a pit (which will be dealt with in section 2.2) can be found, in which chloride is shown as well.

$$Fe^{2+} + 2H_2O \rightarrow Fe(OH)_2 + 2H^+ \tag{2.6}$$

Passive layer

A passive layer, which typically is an oxide film, is a protective layer on the surface of a metal. This layer is formed spontaneously once the metal surface makes contact with the electrolyte. Reactants are prevented from making contact with the metal, so corrosion can not take place. In figure 2.1 the passive layer can be found including a porous cap over an area where the passive film has been decayed. Through this porous cap, or rust cap, chloride ions and water molecules can be exchanged.

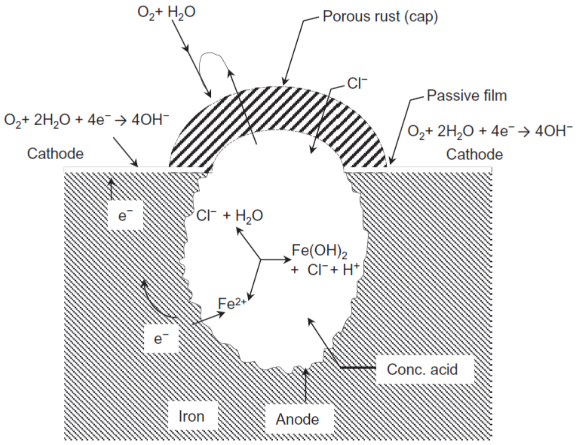

Figure 2.1: Visualisation of corrosion process in a pit [6]

2.1.2. Uniform corrosion

Uniform corrosion is corrosion over the complete surface which is in contact with the environment. Using Faraday's law (equation (2.7)) the (ideal) uniform corrosion rate r can be calculated, which is the amount of metal thickness lost per time unit.

$$r = \frac{mi}{nF\rho} \tag{2.7}$$

Where m is the atomic mass of the metal ions, i the current density which can be found using polarization (or Evans) curves, F is the Faraday constant, and ρ the density of the metal. Different other analytic models exist that estimate the uniform corrosion rate or weight loss, based on or validated by field or experimental data, but will not be discussed.

2.1.3. Localized corrosion

Three types of localized corrosion are the most prevalent; (i) pitting corrosion, (ii) crevice corrosion and (iii) stress-corrosion cracking (SCC) [9]. Pitting corrosion occurs due to chloride ions breaking down the passive film locally. Crevice corrosion, or contact corrosion, occurs below the contact surface of a metal with another metal or a non-metal. Stress corrosion cracking is the initiation and propagation of a crack in a metal due to the combined effect of a static stress and chemical reactions.

This research work focusses on pitting corrosion, because pitting corrosion is a common and potentially dangerous form of corrosion in marine structures [10]. This is because (i) corrosion pits are hard to detect due to a rust cap on the surface of the material (see figure 2.1) and an unpredictable pit shape (see figure 2.2), (ii) the location of nucleation of a corrosion pit is unpredictable (pits can initiate at any location), and (iii) pits can cause a structure to fail although only a minimal weight loss has occurred [6]. In figure 2.3, corrosion rates of uniform and pitting corrosion are compared using data of North Sea conditions in Melchers pit growth model, which will be dealt with in section 2.2.4. It can be seen that the maximum pit depth increases significantly faster than the mean uniform corrosion depth over the whole time domain. In combination with a static stress, a pit can be an inhibitor of SCC, and in combination with a cyclic stress, a pit can be an inhibitor of a fatigue crack. Because fatigue is a common loading type in offshore structures, SCC is not looked at in this research work specifically. The next section deals with pitting corrosion in more detail.

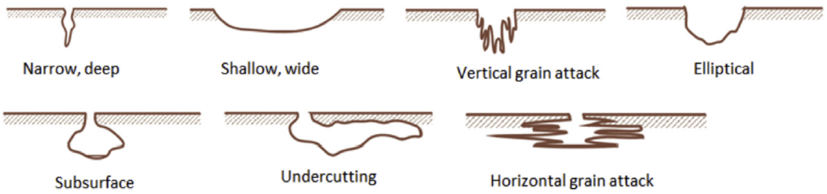

Figure 2.2: Variations in cross sectional shape of pits [10]

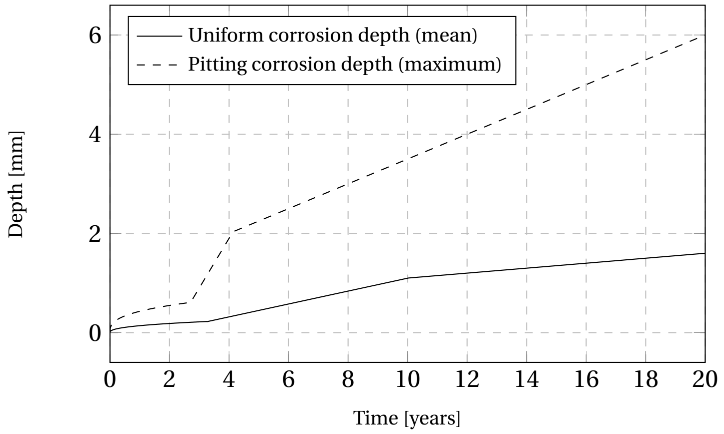

Figure 2.3: Comparison of uniform and pitting corrosion rates for North Sea conditions [11, 12]

2.2. Pitting corrosion

As mentioned in section 2.1.3, pitting corrosion is one of the most deteriorating forms of corrosion. To be able to understand and assess pitting corrosion models, first the phases of the evolution of a corrosion pit and the factors influencing this process need to be understood.

Baroux [13] simplified the pitting corrosion process into three steps: (i) passive layer breakdown and pit nucleation, (ii) metastable pit development resulting in either repassivation (pit growth arrest) or pit stabilization, and (iii) stable pit growth. In figure 2.4, the mechanism for the onset of a stable pit is shown, which includes all three steps.

The local breakdown of the passive layer can have many causes, e.g.: chloride ion formation, local film thinning, voiding or inclusions and collapse of the film, or local stress gradient [13]. Grain boundaries may be a more sensitive location as a pit initiation location. A local interruption of the passive layer is called a pit nucleus. At this location a pit can initiate and the metastable growth can start. In this phase, the pit (embryo) can evolve into a stable growing pit or repassivate and stop growing. Through experiments it has been found that a critical pitting potential E_p exists, i.e. the potential below which a pit will come to arrest, just as a critical pitting temperature. The potential depends on many factors, e.g.: chloride ions, pH, current density, and alloy composition of steel [13].

A large number of factors influencing pitting corrosion has been listed by Bhandari [10]. Bhandari divided all

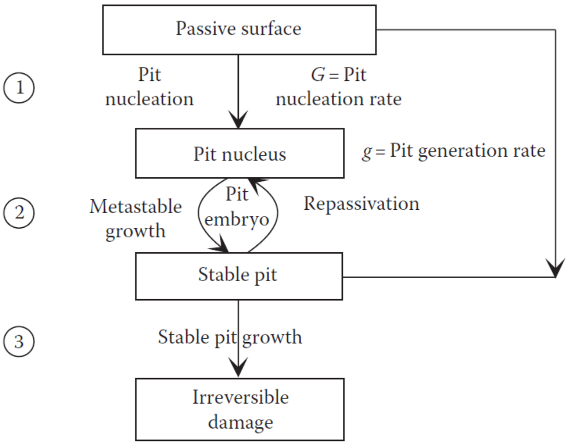

Figure 2.4: Phases of pitting corrosion [13]

factors into four subjects: (i) physical (environmental) factors, (ii) chemical factors, (iii) biological factors and (iv) metallurgical factors. Some physical, chemical and metallurgical factors have already been emphasized, but biological factors have not. According to Melchers [12], biological activity is one of the most important influences on pitting corrosion. The next section deals with this factor. A mechanism not mentioned by Bhandari, is the effect of stress on corrosion pit growth. This is a mechanism especially of importance in corrosion fatigue, and will be dealt with in section 2.2.2.

2.2.1. Biologically enhanced corrosion

Fouling on offshore structures can have two forms of negative impact on the fatigue life: (i) the corrosion process can be enhanced, which is called microbiological induced corrosion (MIC), and (ii) the roughness and wetted area of the structure is increased, resulting in increased stresses in the structure. One of the bacteria causing MIC, are sulfate-reducing bacteria (SRB). SRB form iron ions into ironsulfate (FeS) using hydrogen sulphide (H_2S). When a favourable environment (depending on physical factors as temperature, pH, nutrients, and dissolved oxygen) has been created, and there is access to the steel surface, SRB can create an anaerobe environment at the pit surface, and accelerate the pit growth significantly [14]. MIC has little influence on general corrosion.

2.2.2. Effect of cyclic stress

A corrosion pit can act as a stress concentration and plasticity can be localized around corrosion pits. Scientists are not unanimous whether it is the degree of plasticity or the applied stress that is the accelerator of pit growth. Fatoba [15] simulated corrosion pit growth using a micro-capillary cell in X-65 pipeline steel. A cyclic stress range of 180 MPa has been applied in combination with a stress ratio of 0.1 and a frequency of 2.0 Hz. Ma [16] did pitting corrosion experiments in a NaCl solution for A-537 steel with MnS inclusions at the surface. A cyclic stress range of 280 MPa has been applied in combination with a stress ratio of 0 and a frequency of 1 Hz. The results of both experiments can be found in figure 2.5. The applied maximum stress in both experiments in combination with a corrosion pit is most probably exceeding the yield stress limit of both steels. Plastic strains can therefore be observed in the experiments. For both experiments it has been found that the corrosion pit growth rate is higher for an applied cyclic stress.

Gutman [17] studied the mechanochemistry of materials, which includes the effect of stress on the dissolution rate in the corrosion process. Gutman established a relation between the stress in the material, plastic strain and the anodic current of deformation, see equation (2.8).

$$\frac{I}{I_{\mathrm{n}}} = \left(\frac{\Delta\epsilon}{\epsilon_0} + 1\right) \exp\left(\frac{\sigma_{\mathrm{m}} V_{\mathrm{m}}}{RT}\right) \tag{2.8}$$

where I is the anodic current of deformation, I_{n} is the anodic current for no deformation, V_m is the molar volume, $\Delta\epsilon$ is the plastic strain, ϵ_0 is the onset of strain hardening, σ_{m} is the spherical part of the macroscopic stress tensor depending on the applied stress, R is the gas constant and T is the temperature. These equations

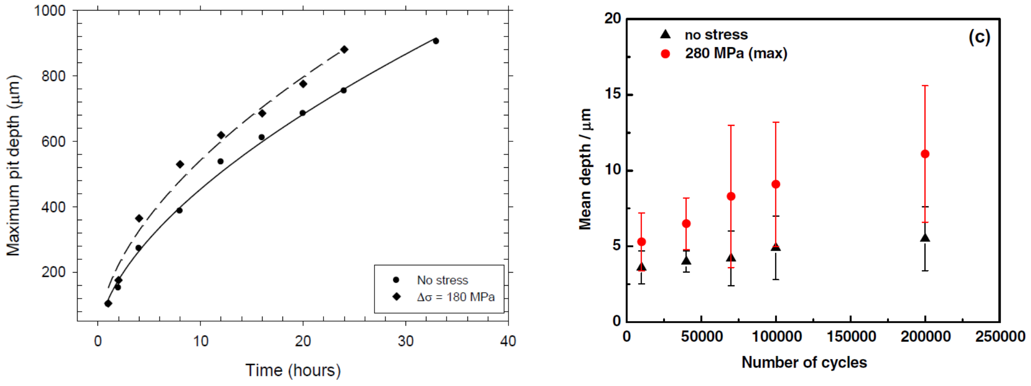

(a) Using a micro-capillary cell for X-65 steel [15]

(b) Using a NaCl solution for A 537 steel [16]

Figure 2.5: Effect of cyclic stress on corrosion pit growth

result in plastic strain having a larger effect on pit growth than elastic strains. Experimentally, Guan [18] showed for stainless steel, that peak stresses above the yield strength increase the metastable pitting growth and initiation rate, implying that plastic deformation has more influence than elastic deformation. Ebara [19] also showed a higher pit initiation rate for high stress amplitudes for stainless steels, although not necessarily at the yield strength. Ishihara et al. [20] added the effect of stress to the exponential pit growth law (which will be discussed in section 2.2.4), and also studied the effect of cyclic stress frequency on the pit growth in aluminium. Ishihara concluded that the latter effect could be neglected, but a note should be added that only a short amount of time was considered and a low stress amplitude.

2.2.3. Hydrogen embrittlement

Hydrogen embrittlement (HE) is a possible consequence of the corrosion process. Hydrogen atoms are reactants in combination with electrons according to equation (2.2), but a hydrogen atom can also, in combination with one electron, be adsorbed by the metal. When this occurs in stressed regions, the growth of cracks is promoted [9]. HE is typically not occurring in steels having yield strengths of less than 700 MPa, although loading conditions and hydrogen concentration may affect this limit [21]. When cathodic protection is applied (see section 2.2.5), the chance of HE occurring is higher, due to more dissolved hydrogen atoms in the electrolyte [22], so material choice is then more important for HE.

2.2.4. Pitting corrosion models

The availability of fundamental pitting corrosion models is necessary to fully understand the pitting corrosion process and to create simplified models that can be used in engineering solutions. Currently available models can be divided in (i) analytic models, which also include models based on experimental data, and (ii) numerical models.

Analytic models

In early corrosion (fatigue) models, simplistic models for corrosion pit growth were assumed. A power (i.e. exponential) law was first proposed by Romanoff [23] to relate the pit depth a to time t, see equation equation (2.9).

$$a(t) = c_1 t^{c_2} \tag{2.9}$$

Where c_1 and c_2 are parameters that should be determined empirically. This law was applied by Kondo for his corrosion fatigue model [24], in which he used $c_1 = 1/3$ for low-alloy steel. A value of c_2 was determined using Faraday's law (equation (2.7)), which was validated using experiments. Velázquez [25] mentioned that these parameters depend on many variables, of the environment and material, which makes it hard to use this as a deterministic approach. Some studies used the power law, and also implemented pit nucleation, so t in equation (2.9) was replaced by $(t - t_i)$, where t_i is the pit nucleation time [26].

Melchers [12, 27, 28] developed a bi-modal pit growth model in which four phases based on uniform pit growth are included to determine the long-term pit growth for mild and low-alloy steels: (1) kinetic phase, which is assumed to be a linear function, (2) oxygen diffusion-controlled phase, (3) hydrogen reduction phase, and (4) steady state diffusion-controlled phase. The phases are shown in figure 2.6. Melchers applied this model to determine the parameters for the curve on multiple sources of field data from literature, including data from Blekkenhorst et al. [29] of the North Sea for an experimental steel (I4 mild steel), which is comparable in alloy composition to S355 steel. Using Melchers' model, the maximum pit depth can be determined, depending on the field data used for calibration. The field data of Blekkenhorst is based on the maximum pit depth of a 1 m^2 panel, immersed in the North sea up to 7.2 years.

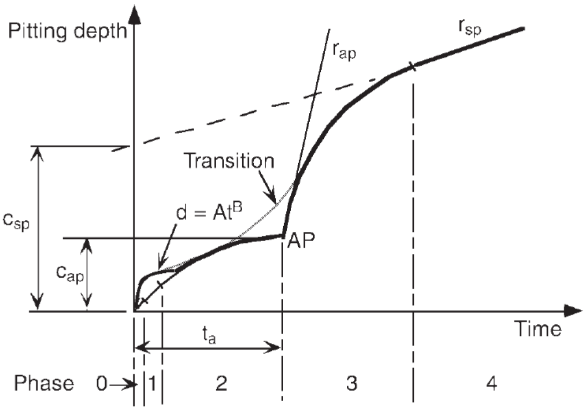

Figure 2.6: Bi-modal pit growth model of Melchers [12]

To determine the probability of a certain pit depth after a certain amount of time, a statistic model as Extreme Value analysis could be used, for which Melchers proposed Gumbel distributions [12]. Wang [26] used a Weibull function to fit field data of corrosion pit growth, based on pitting corrosion mechanics and Melchers' model. The parameters in the Weibull functions can be determined based on the environment (seawater temperature, dissolved oxygen, salinity, pH-value) and the composition of the steel (alloying elements). Just as Melchers' model, the model of Wang can be applied only to mild and low-alloy steels. Wang used field data of A3 steel, which is comparable in alloy composition to S355 steel, in Chinese seas of a period of 16 years, but further specification of this data has not been found. Both models, adapted for North Sea conditions, can be found in figure 2.7. Wang's model includes a maximum pit depth, where Melchers' model includes a constant pit growth rate in the final phase. This results in a large difference between the models for a corrosion exposure of 10 to 20 years. A more extensive review of pit growth models is given by Bhandari [10].

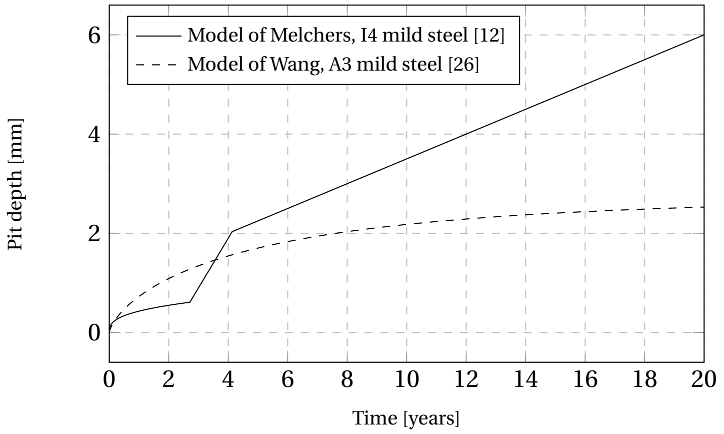

Figure 2.7: Comparison of uniform and pitting corrosion rates for North Sea conditions

It should be noted that most analytic models found in literature do not include the effect of stress or strain on the pit growth, however, experiments show that stress does have effect. Also, the analytic models do not give insight in the micro-topography or length and width of a corrosion pit, only in depth.

Numerical models
Although numerical models of pitting corrosion are available, they are not always well validated with experiments. A review on numerical pitting corrosion models is written by Jafarzadeh et al. [30]. Jafarzadeh divided the models into non-autonomous models, which solve for the corrosion front as a separate step in the solution process, and autonomous models, in which the evolution of the corrosion front is autonomous. Only autonomous models will be discussed here, because these are more recent and less complex and costly because there is no need for remeshing.

Four types of autonomous numerical models are available: (i) finite volume, (ii) cellular automata (CA), (iii) peridynamic and, (iv) phase-field models. Scheiner et al. [31] used a finite volume model to solve the governing equations of his model based on either diffusion- or activation-controlled pitting corrosion. Scheiner validated his model to stainless steel experiments by means of graphs of the current density to the electrochemical potential. Wang et al. [32] simulated metastable corrosion pit growth for stainless steel including the influence of mechanical stress using a CA model coupled with FEM. Wang used the Gutman equation (equation (2.8)) to include the effect of stress and strain on the pit growth kinetics for stainless steel, but only qualitatively validated the results. Fatoba et al. [15] also used a CA model coupled with FEM and validated it for a corrosion pit induced by a micro-capillary cell developed by Evans [33] in API 5L X65 steel. Chen [34] created a peridynamic model that includes microstructural effects and can capture subsurface damage as well, but does not include the effect of stress and/or strain on pit growth. Chen created his model for stainless steel and validated it by the dependence of depth with time of $\sqrt{t}$ and the same current density - electrochemical potential as Scheiner. Duddu [35] took a different approach and used XFEM coupled with level sets to track the moving interface of a corrosion pit surface in a stainless steel in which he did not take stress or strain into account. The model of Duddu is non-autonomous, but mentioned because it is used by Mai et al [36]. Duddu validated his model by 1D pencil electrode experiments of stainless steel and also by comparing to numerical work of Scheiner. A phase field model was developed by Mai to simulate activation- and diffusion-controlled pitting corrosion which gave equal results to the XFE-LS model of Duddu. Jafarzadeh claims that there is no model that clearly works best for each condition. It depends on the demands on the model which one works best It should be noted that most of the mentioned models are validated for 2D situations. Multiple studies note that the researchers are currently working on the 3D extension of their models [15, 34].

2.2.5. Corrosion mitigation techniques

In the offshore wind industry there are several techniques that are applied to the design of wind turbines to prevent degradation of the material due to corrosion. This research work will not include any of the given mitigation techniques, but for completeness a list of the available techniques and their benefits and drawbacks is given below.

- **Coating** - A coating can be applied to the surface of a metal structure to prevent the corrosive environment from interaction with the metal. Many different types of coatings are available which increase the corrosion fatigue life of a structure [37, 38]. The danger of coatings is that, subjected to (fatigue) loading, a coating can crack, which will lead to localized corrosion through the cracked coating surface.
- **Cathodic protection** - By applying an electrode potential to the steel structure, the environment for the chemical reactions of the corrosion process is less favourable. The influence of cathodic protection is affected by the applied potential. A summary of several studies into cathodic protection is made by Komai [39].
- **Corrosion resistant materials** - Steel and other metals are never fabricated from one type of metal, but consist of alloys. Some alloys are known to improve fatigue life, while other alloys are known to improve the resistance to (localized) corrosion, as listed by Hill and Perez [40]. The choice for a better behaviour for a certain process of a metal alloy is typically accompanied by a worse behaviour for a different process.
- **Inspections** - In the offshore industry, regular inspections are carried out at structures for safety reasons. There are visual inspections carried out to notice irregularities of several millimetres at the surface of a material, as well as non-destructive testing methods such as Eddy current testing or magnetic particle inspection to detect irregularities at the surface or subsurface of a minimum size of roughly 1 mm [38, 41].

2.3. Fatigue

Fatigue is a degradation mechanism that results in failure of a structure due to cracks initiated by a cyclic stress. Polák [42] divided the evolution of fatigue damage in crystalline metals into two major phases, as can be seen in figure 2.8: (i) macrocrack initiation, and (ii) macrocrack growth and fracture. These two phases are elaborated upon separately in the following two subsections.

2.3.1. Fatigue crack initiation

Fatigue crack initiation is the formation of cracks on or below the surface of a material. To understand crack initiation of metals under fatigue loading, initially the micro-scale should be studied.

First, a note should be added on the definition of crack initiation. Crack initiation sets the limit on the minimum size of a fatigue crack, assuming no existing cracks are in the material. Typically, initiation is a complex process that can result in an extremely small crack of <1 µm or a crack that initiates and rapidly grows up to 100 µm [43]. To the scientist, initiation is defined as a crack that is visible using any tools, which often is microscopy. To the engineer, the same definition yields, but the tools of engineers are non-destructive testing methods, which detect only larger crack sizes. To the scientist, this means that the engineer takes small crack growth in its definition of initiation. The crack that is found by the scientist is called a micro-crack, while the crack found by the engineer a macro-crack, but also these names do not have quantitative definitions.

Initiation can, from micro-scale point of view, occur at three locations in metals [44]:

- **Persistant Slip Bands (PSBs)** - irreversible dislocation occurs due to PSBs, extrusions, and intrusions in surface grains that are optimally oriented for slip.
- **Grain Boundaries (GBs)** - cyclic slip can result in microcracks at GBs and twin boundaries.
- **Inclusions** - local concentration of (plastic) strain at inclusions or hard particles results in crack initiation preferably at relative large grain sizes.

A comprehensive review on the physics of fatigue crack initiation with particular interest in the microstructure is given by Sangid [45]. With a more macro-scale point of view, Polák [42] defined the general scheme of fatigue damage evolution in figure 2.8. Clearly the separation between micro-, and macro-cracks is seen here; after the first four processes of macro-crack initiation, a crack will nucleate. After this micro-crack nucleation, interaction between micro-cracks may occur next to short crack growth before a macro-crack is initiated. From this overview, it is clear that the plastic stress-strain response, and therefore the history of cyclic applied stress plays an important role in the crack nucleation.

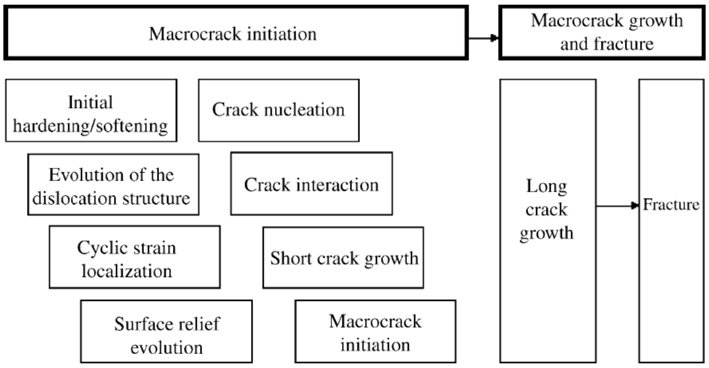

Figure 2.8: Evolution of fatigue damage in crystalline metals [42]

Softening/hardening

The first phase mentioned by Polák is initial softening/hardening, the mechanism of moving the stress-strain curve either up (hardening) or down (softening) in the plastic region of the curve. In combination with fatigue loading, hysteresis loops will appear when the stress-strain history is known, as shown in figure 2.9. This mechanism is important to keep track of, because by a constant amplitude (CA) fatigue loading, the strain amplitude will not necessarily be constant, especially not when the geometry is changing, as is the case with corrosion pit growth.

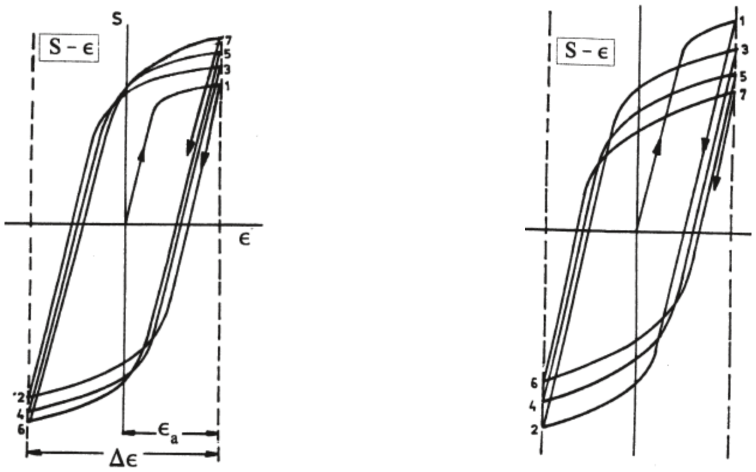

(a) Strain hardening

(b) Strain softening

Figure 2.9: Hysteresis loops under constant strain amplitude ϵ_a [46]

Short crack growth
When looking at macro-crack initiation, short crack growth is taken into account. In short crack growth, opposite to long crack growth, the microstructure still plays an important role [42]. Grain boundaries for example decelerate or even arrest a propagating small crack. Schijve [46] therefore defined the initiation period as supposed to be completed when microcrack growth (i.e. short crack growth) is no longer depending on the material surface conditions.
Polák [42] also concluded that the majority of the fatigue life of materials subjected to normal fatigue loading conditions is spent on short crack growth. Therefore, the decision whether to take short crack growth into account for the determination of crack initiation life is important to accentuate.

2.3.1.1. Initiation life models

Fatigue initiation is a microscopic process. Therefore, models are developed which capture the microscopic effects. The current use of fatigue initiation models in engineering solutions comprises relatively simplistic models. These models are based on experiments and are therefore a more macroscopic approach to determine fatigue initiation life. The approaches are elaborated upon in the next sections.

Microscopic
Microscopic models that can predict fatigue initiation life take into account the microstructure of the material, i.e. slip planes and grain boundaries. Pineau et al. [47] and McDowell and Dunne [48] reviewed models that make use of fatigue indicator parameters (FIPs). FIPs are used as indicators for the driving forces of crack initiation. FIPs are often either strain or energy based. Nicolas et al. [49] used FIPs to estimate the location of crack initiation in corroded aluminium and compared this to experiments. He found that the locations that crack initiation occurred, the FIP values were significantly greater than the average value, although the location of crack initiation did not necessarily have the highest FIP value. Nicolas did not estimate the crack initiation life. The microstructural approach of using FIPs is specifically useful to compare microstructures of different materials. The use of these kind of models in engineering solutions is still a subject of discussion [50].

A different microscopic method, also based on energy, is proposed by Mura and Nakasone [51]. They stated that crack initiation occurred at a certain value of change in Gibbs free energy. This method is not often applied in fatigue life determination models.

Mesoscopic
Continuum Damage Mechanics (CDM) is a method that can be implemented in numerical methods that try to describe microscopic processes at a macroscopic framework, and therefore can be argued to be a mesoscopic method. Most complete CDM methods are multi-scale methods, which can provide information of the damage evolution in a material throughout different scales. This section will focus on this kind of models.

CDM is a relatively new method, which can be used to predict initiation in many types of materials. Models of CDM divides a material into small elements, called a representative volume element (RVE). In an RVE, a damage variable D is determined based on damage at the micro-scale level such as nucleation and growth of voids, cracks, cavities, meso cracks and others [52]. A critical damage criterion D_c is applied and defined as the condition at which an RVE is fractured. For initiation, a value of $0.2 < D_c < 0.5$ is applied, depending on the material type [53]. The most popular CDM model is the model of Lemaitre [52], which is described in his book [53], and determines the initiation life of a meso/macro crack. According to Lemaitre, the size of the crack determined at initiation is 0.2 to 0.5 mm for steels, dependent on the size of the RVE.

Macroscopic

The most applied approach in determining the fatigue crack initiation life of a metal is the strain-life method. This method considers plastic and elastic strain separately, but in one formulation to determine the fatigue initiation life. Stress and strain are coupled using the Ramberg-Osgood formulation

$$\epsilon_\mathrm{a} = \epsilon_\mathrm{a}^\mathrm{e} + \epsilon_\mathrm{a}^\mathrm{p} = \frac{\sigma_\mathrm{a}}{E} + \left(\frac{\sigma_\mathrm{a}}{K'}\right)^{1/n'} \tag{2.10}$$

that describes a hysteresis loop, where E is the Young's modulus, K' is the cyclic strength coefficient and n' is the cyclic strain hardening exponent. Masing [54] later added that the stress amplitude versus strain amplitude can be expressed using the same equation. Basquin [55] gave a formulation for the strain-life equation by only implementing elastic behaviour. A plastic part was developed separately, but at the same moment, by Coffin [56] and Manson [57]. Combined, the following expression is found:

$$\epsilon_\mathrm{a} = \epsilon_\mathrm{a}^\mathrm{e} + \epsilon_\mathrm{a}^\mathrm{p} = \frac{\sigma_\mathrm{f}'}{E}(2N_\mathrm{f})^b + \epsilon_\mathrm{f}'(2N_\mathrm{f})^c \tag{2.11}$$

where σ_f' is the fatigue strength coefficient, ϵ_f' the fatigue ductility coefficient, b the fatigue strength exponent, c the fatigue ductility exponent, and $2N_\mathrm{f}$ is the number of reversals. All fatigue coefficients and exponents are determined using experiments in which round specimens are fatigued with a minimum notched diameter of about 5-8 mm until failure.

Typically, experiments of thin, polished specimens under a cyclic, fully reversed, strain-controlled, uniaxial loading are used to obtain strain-life curves. The experiments are typically ceased at failure, but sometimes the experiment is stopped earlier, to obtain fatigue crack initiation life. Because crack propagation life will be relatively short in such thin and polished specimen, it can be argued that, using the strain-life method, initiation of a macrocrack of about 1-2 mm is determined [58]. A study of Dowling et al. [59] has concluded that the initiation life of a fatigue crack of 0.07 mm is a fraction of about 10% of the total fatigue life for a fatigue life of ≤25,000 cycles in strain-life experiments of a steel type comparable to S355 steel. In a different study, Dowling et al. [59] found that the fraction of initiation life of the total fatigue life ($N_\mathrm{i}/N_\mathrm{f}$) increases for higher fatigue lives. Although the latter study was for a higher strength steel than S355 steel, it is generally accepted that the fraction $N_\mathrm{i}/N_\mathrm{f}$ is higher in the high cycle fatigue regime than in the low cycle fatigue regime.

Mean stress effects are not implemented into equation (2.11), but are proposed by Morrow [60], and Smith, Watson and Topper (SWT) [61]. Morrow's equation is found to work better than the SWT approach for materials where the fatigue strength coefficient is substantially larger than the true fracture strength $\tilde{\sigma}_\mathrm{f}$ [58]. Xin et al. [62] implemented the strain-life method including SWT mean stress correction in a FEM program to determine initiation life of a S355 steel specimen.

2.3.2. Fatigue crack propagation

Fatigue crack propagation describes the lifetime of a fatigue crack from initiation to failure of the structure. Because this research work focusses (more) on initiation, propagation will be elaborated upon briefly.

For fatigue crack propagation calculations, the stress intensity factor (SIF) K is used to indicate the severity of the stress distribution around the crack tip. The SIF is calculated using:

$$K = Y\sigma\sqrt{\pi a} \tag{2.12}$$

where Y is a factor depending on the shape and geometry of the crack, σ the applied stress and a the crack length. After fatigue crack nucleation, first a short crack will propagate. This is still dependent on microstructure. This region is called the threshold region, due to the SIF of the crack should be higher than the SIF threshold to propagate. The next region is the Paris region, for which the fatigue crack growth rate can be determined using the Paris equation [63]

$$\frac{da}{dN} = C\Delta K^m \tag{2.13}$$

where $\frac{da}{dN}$ equals the pit growth rate, C and m are material constants, and ΔK is the SIF range. The third crack growth region is the last region until fracture. This region is the stable-tearing crack growth region in which the crack growth rate is high, in the order of 0.01 mm/cycle and above [46].

2.3.3. Influence factors

After understanding both the fatigue crack initiation phase as the fatigue crack propagation phase, it is possible to list the factors influencing these processes. The factors can be divided into three categories: (i) mechanical, (ii) metallurgical and (iii) environmental. A selected amount of factors are listed per category below.

- **Mechanical** - Difference in cyclic loading can be expressed as mechanical factors influencing fatigue behaviour: (i) stress ratio, (ii) frequency, (iii) waveform of the applied cyclic stress, (iv) amplitude, (v) residual stresses (due to welds or the crack closure mechanism) and (vi) for a variable amplitude load, the order of applied cyclic stress amplitudes. These parameters influence both fatigue crack initiation and propagation behaviour.
- **Metallurgical** - Different material types have different fatigue behaviour. For this research work, structural steel is of interest, for which the following factors are of importance: (i) alloy composition, (ii) microstructure, (iii) heat treatment, (iv) material properties (yield stress, Young's modulus, toughness, brittle/ductile, etcetera), (v) manufacturing defects, (vi) inclusions, voids and pores, and (vii) grain size and orientation. In monopiles, the grain orientation is favourable for crack initiation, but unfavourable for crack propagation due to the rolling direction being in the transversal direction of the monopiles, which is perpendicular to longitudinal stresses as a result of bending due to wind loading [7, 64, 65].
- **Environment** - The environment can have influence on the fatigue process by corrosion, which may lead to a rougher surface, a smaller wall thickness, stress concentrations and more brittle behaviour due to the absorption of hydrogen. Cathodic protection, one of the mitigation techniques for corrosion, can have a negative impact on fatigue life depending on the applied potential. Komai [39] claims that cathodic protection retards the crack initiation, but may increase the fatigue crack growth rate, which may be caused by hydrogen embrittlement.

2.3.4. Fatigue calculations in practice

Fatigue calculations are necessary for design and maintenance studies. Calculations are performed according to standards, as the Eurocode for structural design. For offshore structures the most common classification society in The Netherlands is DNV GL. In the standard for fatigue design of offshore steel structures, S-N curves are given for different structural details and environments [66]. S-N curves, relating a nominal stress range versus number of cycles to failure at that stress range, are the most common tool to determine fatigue lifetime. No distinction is made for different regimes (fatigue crack initiation, propagation), which makes S-N curves a simple tool to use in engineering calculations. The S-N curves given in the standard are defined for base material as well as for welds, which are usually more fatigue sensitive locations than plain steel due to residual stresses and imperfections. Welds are not included in this research work, so this is not treated in this literature review. For plain steel, the S-N curve as given in figure 2.10 should be used. As shown in the figure, the standard also makes distinction between fatigue in air, in seawater with cathodic protection and under free corrosion (without mitigation measures). For the S-N curve in seawater with cathodic protection, the transition point is moved from 10^7 to 10^6 cycles. For the S-N curve in free corrosion, the transition point is not present. It is unknown whether pitting corrosion has occurred in the tests, where the SN-curve in free corrosion is based upon.

In the standard for corrosion protection of wind turbines, minimum values for a uniform corrosion rate in the splash zone can be found [67]. This is 0.30 mm per year for North Sea conditions on the external surface of a wind turbine. After selecting the correct S-N curve, a fatigue safety factor, the design fatigue factor (DFF) will be applied. The DFF is different in different zones of the wind turbine structure. A value of 3 should be applied in the splash zone, 2 below the splash zone and 1 above the splash zone [68]. This is mainly due to splash zone being inaccessible for inspections [69], but also due to harsh environment in the splash zone as

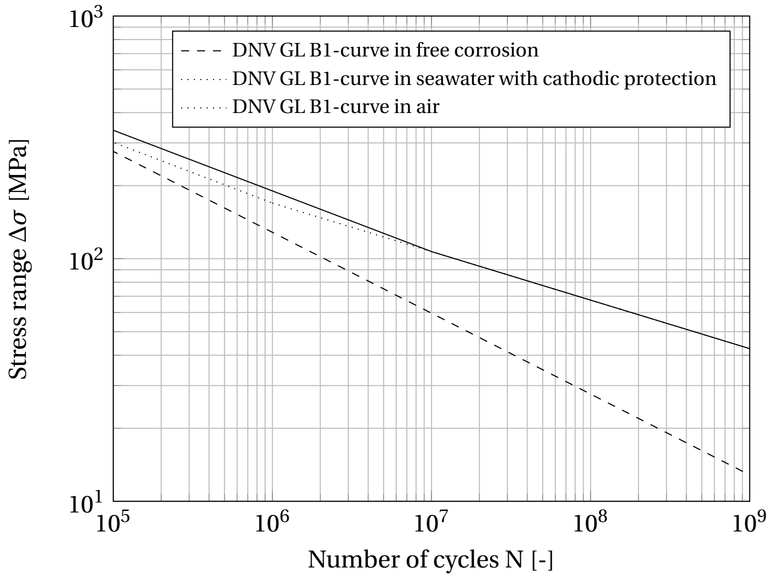

Figure 2.10: S-N curves for air and free corrosion, from DNV GL-RP-C203 [66]

shown by Melchers [70]. A note should be added that pitting corrosion specifically is not mentioned in these design codes.

2.4. Corrosion fatigue

When the combined, synergetic effect of corrosion and fatigue is evaluated, a S-N curve as Duquette [71] proposed in figure 2.11 can be found. In this figure, it can be seen that the fatigue limit is not defined within 10^8 cycles for corrosion fatigue. A fatigue limit does exist for pre-pitted specimens in air or untreated specimens in fatigue loading. This schematic is supported by multiple experiments as Li et al. [72], Palin-Luc et al. [73], Zhang et al. [74] and also corresponds to the S-N curves of DNV GL standard (figure 2.10). Some studies do show a fatigue limit, mostly due to run-outs, so not validated through failed specimens [19, 37, 75]. All do show a steeper curve in the medium cycle fatigue range for corrosion fatigue than fatigue in air. Bignonnet [76] performed strain-controlled uniaxial fatigue experiments in air, and a corrosive environment with and without an applied electrode potential. Bignonnet created strain-life curves of the experiments, which can be found in figure 2.12. The slope of the elastic and plastic part of the fitted curve is about equal for air and free corrosion, where the free corrosion curve is positioned more to the left with respect to the strain-life curve in air. The slopes of the strain-life curves in a corrosive environment with an applied electrode potential is lower.

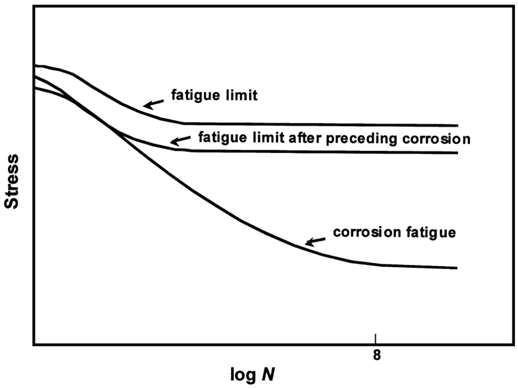

Figure 2.11: Schematic representation of a S-N curve [71]

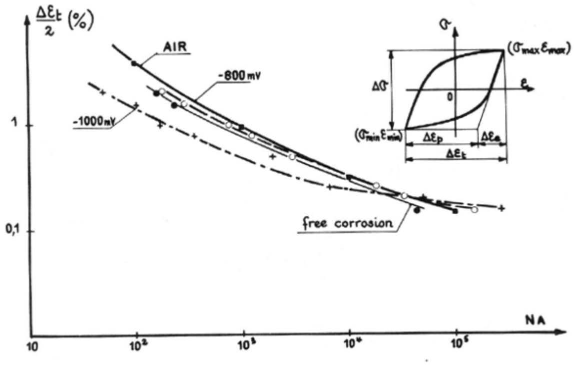

Figure 2.12: Strain-life curve for steel E355 in different environments [76]

2.4.1. Phases

When the phases of pitting corrosion (section 2.2) and fatigue crack initiation (section 2.3) are combined, a graph as figure 2.13 can be created. In this figure the phases are somewhat simplified, but it shows the transition from a pit to a crack clearly. Also, the dependence of corrosion on time, and fatigue on cycles is shown. The factor that links these two dependents, is the frequency of the load cycles. The transition between these two dependants is the main reason that corrosion fatigue experiments can not produce reliable predictions on the pit-to-crack transition, which will be discussed in section 2.4.2. Li and Akid [72] show the same phases in figure 2.14 as seen in figure 2.13, but with experiments. Also, figure 2.14 shows the speed of the defect size (either the pit depth or the crack length) plotted against the crack length. This figure shows clearly that the pit growth rate decreases exponentially in time, and that the long crack growth rate is constantly increasing in time. The pit-to-crack transition is an unclear phase in this figure.

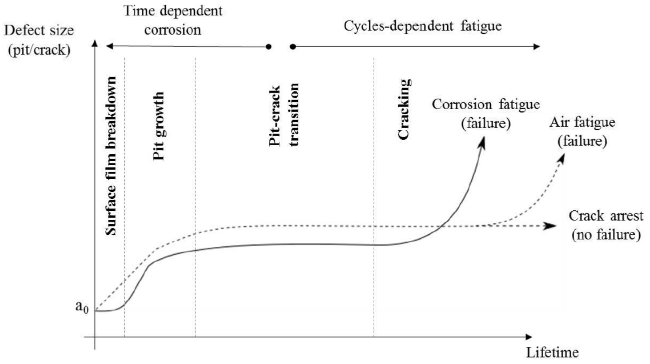

Figure 2.13: Phases of corrosion fatigue [50]

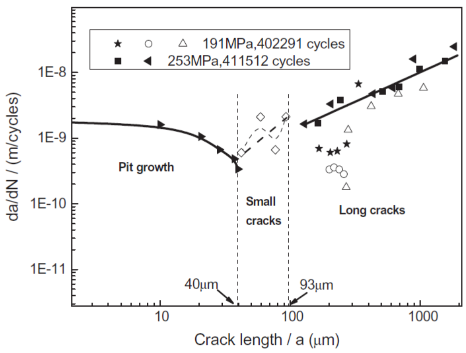

Figure 2.14: Corrosion pit and crack growth rate versus crack length [72]

2.4.2. Experiments

Due to the large number of factors influencing the corrosion fatigue behaviour, a large number of choices need to be made for performing corrosion fatigue experiments. It is hard to perform corrosion fatigue experiments realistically, because as well the corrosion process as the fatigue process needs to be accelerated, which are respectively time dependent and cycles-dependent as can be seen from figure 2.13. The fatigue process can be accelerated by increasing the frequency, but the corrosion process can be accelerated by inducing a electrode potential E in Volt, which leads to a higher current I in Ampères, or by increasing the temperature T or pH. But, these factors are not under control in such a way that it is possible to accelerate the pit growth in a realistic way. Therefore, most experiments are aimed at finding the influence of one factor, but still influence of other factors may remain uncertain.

In corrosion fatigue experiments, often a pit is created on the specimens before the experiment actually starts, which is called pre-pitting. This can be done under various circumstances: (i) artificially drill a hemispherical hole which creates a smooth surface [77], (ii) use a corrosive environment to develop a corrosion pit, which creates a rough surface and includes hydrogen absorption [15, 33, 49, 73, 78], and (iii) apply loading to the specimen during the pitting corrosion process in an corrosive environment [15, 79]. This method adds the factor of pit depth and shape to the list of influence factors, but takes away a number of factors as well. After pre-pitting, the specimen is subjected to a fatigue loading in air or a corrosive environment. This leads to a difference in S-N curves as schematic presented by Duquette [71] in figure 2.11. Duquette implies that no fatigue limit exists for corrosion fatigue cases.

2.4.3. Damage models

In analytic methods of life prediction of metals subjected to corrosion fatigue, usually a threshold stress intensity factor (SIF) range ΔK_{th} is determined to predict the pit-to-crack transition. This value is determined by several researchers based on linear elastic fracture mechanics (LEFM). Using this theory, the assumption is made that a three dimensional corrosion pit can be regarded as a two dimensional crack. After the pit-to-crack transition, Paris' law for long crack growth [63] is used. A review on corrosion fatigue life estimation models is given by Larossa et al. [50] for models that were published before 2018. Only models that implemented the pit-to-crack transition in the determination of the corrosion fatigue life are elaborated here. The crack growth model of the models discussed below are neglected. In all models, the pit is considered to be either hemispherical or elliptical, and the aspect ratio is considered to be constant.

Pit considered as a long crack

Classic models based on LEFM assume two phases: (i) fatigue crack initiation, and (ii) fatigue crack propagation. In time, more phases of the corrosion fatigue process are described by models. The first substantive model was proposed by Kondo [24], which is called the "competition model". Kondo proposed the pit growth law as $2c \propto At^{1/3}$ and determined a critical pit condition $(\Delta K)_\mathrm{p}$ at which the crack growth rate is higher than the pit growth rate. Chen [77] combined two criteria for the pit-to-crack transition: (i) the stress intensity factor range should be equal or higher than the threshold stress intensity factor range (equation (2.14)) and (ii) the crack growth rate should be equal or higher than the pit growth rate (equation (2.15)).

$$\Delta K \geq \Delta K_\mathrm{th} \tag{2.14}$$

$$\left(\frac{da}{dN}\right)_\mathrm{crack} \geq \left(\frac{da}{dN}\right)_\mathrm{pit} \tag{2.15}$$

Wang et al. [80] used the pit growth law determined by Kondo and used the fatigue crack initiation model proposed by Mura and Nakasone [51]. This model determines the initiation lifetime based on the change in Gibbs free energy, which is a microscopic approach to determine the fatigue crack initiation life as described in section 2.3.1.1. Ishihara et al. [20] proposed a pit growth model that is a function of the applied stress and time for aluminium. Instead of basing the pit-to-crack transition stress intensity threshold range on the aspect ratio, Ishihara used the $\sqrt{\text{Area}}$ parameter proposed by Murakami et al. [81]. Sriraman and Pidaparti [82] combined the pit growth model of Ishihara with the pit growth model used by Wang. Also the fatigue crack initiation model of Wang is used and the result, including a crack growth model, were S-N curves for corrosion-fatigue behaviour. Concluded was that crack initiation can occur, according to the model, at small pits as well as large pits. The model is not validated for a simultaneous event of fatigue loading and a corrosive environment. Mao et al. [83] used the model of Ishihara and extended it using stress concentration factors (SCF) of corrosion pits by Cerit et al. [84], and made distinction between three ranges of aspect ratios to determine the corrosion fatigue crack initiation life. The model was validated in the same say as Ishihara. Results of the model can be found in figure 2.15. From the figure it can be concluded that the model is less conservative than the model of Sriraman and Pidaparti, but the trend is quite different from the experiments. Li and Akid [72] determined the critical pit depth from where a crack would nucleate by experiments via de da/dN-curve and combined this with two pit growth models:(i) exponential law, and (ii) Faraday's law. Next, a difference between small and long crack growth was made and this was combined to determine the total fatigue life. Results of the model can be found in figure 2.16. It can be found that the model is conservative compared to the test data, but it predicts the lower bound reasonably well. Like Li and Akid, several other studies have shown that the threshold SIF can be determined by making da/dN-ΔK plots through experiments [85–87]. Although another study by Schönbauer [75] shows that fatigue crack growth rate curves do not show a clear threshold value in aqueous solution compared to air.

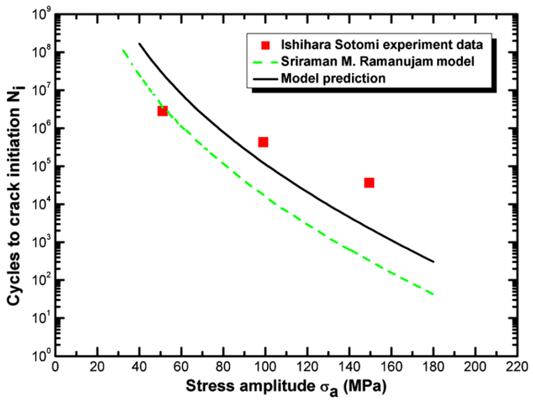

Figure 2.15: Fatigue initiation life prediction of aluminium from the model of Mao [83]

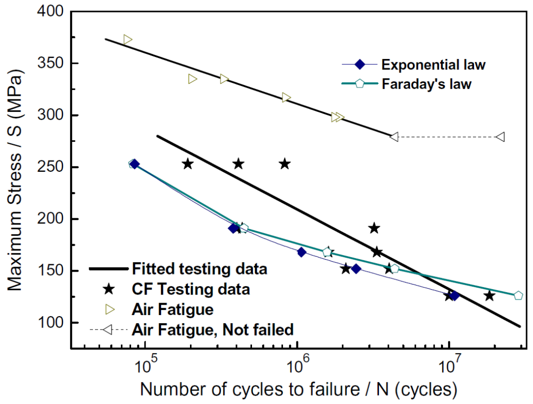

Figure 2.16: Fatigue life prediction of steel from the model of Li and Akid [72]

Pit considered as a short crack
El Haddad [88] proposed a fatigue threshold value $\Delta\sigma_{th}$ for short cracks to propagate in a notch, to determine the SIF threshold range for crack initiation, defined as

$$\Delta K_{\mathrm{th}} = Y \Delta\sigma_{\mathrm{th}} \sqrt{\pi(l + l_0)} \tag{2.16}$$

where l is the crack length, which is equal to zero for initiation, and l_0 is the notch or pit depth a. The geometry factor depends on the location in the pit, where Y is larger at the pit mouth than at the pit base according to Newman and Raju [89]. This approach is applied on steam turbine blades by Salzman et al. [90, 91] and Schönbauer et al. [85, 86]. They found good agreement of the model to the experiments, when shown in Kitagawa-Takahashi diagrams, for fatigue analysis of a pre-pitted specimen in air and concluded that pits can be treated as (short) cracks.

Pit considered as a notch
Zhou et al. [92] compared, just as Fatoba [15], analytically determined notch factors K_{f} based on the aspect ratio to experimentally determined notch factors for corrosion pits. It was found that the analytic methods overestimated the maximum stress in the corrosion pit.

2.4.4. Driving forces of the pit-to-crack transition

Burns et al. [93] studied the pit-to-crack transition thoroughly using microscopy in combination with FEM to validate their thoughts. Aluminium specimens were first corroded by using either isolated-controlled pitting corrosion on the surface of the metal. Next a fatigue loading was applied, until a 10-20 µm crack nucleated. By using Confocal Laser Scanning Microscopy (CSLM) and Scanning Electron Microscopy (SEM) on the corrosion pit surface where a crack initiated, the experiments were evaluated. From figure 2.17 it can be seen that a large scatter of crack initiation locations is observed. Burns concludes here that not only macro-topography of the pit is of importance, but micro-topography (also including jut-in/micro-pit topography) is as well. Cerit et al. [94] had the same opinion and included micro-pits in finite element analyses. Cerit found that the stress concentration factor (SCF) increased significantly after a micro-pit in a corrosion pit was induced.

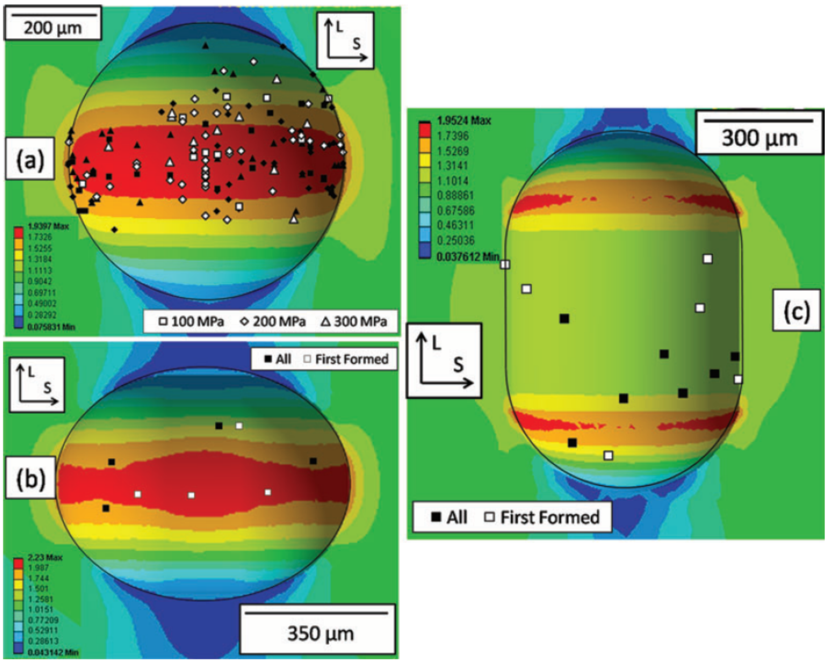

Figure 2.17: Values of k_{t-e} from elastic FEA of the macro-pit size, with crack initiation locations found from experiments marked with white (first crack formed in pit) and black (subsequent crack formations) symbols. Different pit shapes and stress amplitudes are shown. Also note that the loading is applied in longitudinal grain direction. [93]

Turnbull et al. [95] used elastic-plastic FEA to model the stress and strain distribution around a corrosion pit for static loading. They found for static applied high stress, that plastic strain is localised at the pit mouth, while stress is maximised towards the pit base. For low applied stress, plastic strain is localised at the pit base, while stress is maximised at the pit mouth. Accompanied by experimental data including observations using X-ray tomography of stress corrosion cracks nucleating from pits [96, 97], Turnbull concludes that pit growth induced plasticity must be considered a possible factor in determining the pit-to-crack transition. In line with this conclusion is the research of Sabelkin et al. [79], who created corrosion pits on multiple specimens under different static loadings. After a certain pit depth was reached, which was equal for each specimen, a fatigue loading was applied on the specimen, which was again equal for each specimen. It was found that the specimen with the largest applied stress during pit growth, had a longer fatigue crack initiation lifetime. Sabelkin concluded that this was due to plasticity, but a note must be added that the geometry of the pits after reaching a certain depth could be different, which is not stated in the paper. Evans et al. [33] measured a threshold strain value using Digital Image Correlation (DIC) at which a crack would initiate from a corrosion pit. The testing was done using experiments of pre-pitted specimens in air and the threshold strain value was found to be more or less constant for multiple pit geometries.

Fatoba [15] found a difference in crack location and life for equally pre-pitted X-65 steel specimens under fatigue loading in air compared to a corrosive environment. For the corrosion fatigued specimens, the crack initiation location was found at the pit mouth and base, while for the specimens fatigued in air, only at the pit mouth. This suggests that electrochemical factors do play a role in the crack initiation from corrosion pits, due to a more aggressive environment in the pit base than in the pit mouth. It is yet unclear, whether this is due to the degradation of material by corrosion, and this way accelerating crack initiation, or due to the aggressive environment accelerating the initiation directly by for example hydrogen absorption in the steel causing embrittlement [15]. Magnin [98] summarized the current knowledge on this subject, but concluded that more research is necessary in the modelling of local electrochemistry around defects as a pit to obtain quantitative values of fluxes and absorbed hydrogen.

In realistic circumstances, it is reasonable to assume that multiple pits can grow in proximity. The interaction of these pits on the fatigue crack initiation life as well as crack propagation life has been researched including experiments in air by Fatoba [15]. Fatoba found that the distance between pits for a aspect ratio ($a/2c$) of 0.34 and 0.41 respectively for a stress range of 405 MPa should be below 4 times the pit diameter to have effect on the fatigue crack initiation or propagation life. Up to a factor of 40 in fatigue crack initiation life was found for two pits close to each other.

To conclude, four driving forces can be identified for the crack initiation process in a corrosion pit [93]:

- **Geometry** - As well the micro- as macro-topography of the pit location are driving forces in the pit-to-crack transition. The micro-topography includes the surface roughness in the pit, for example due to micro-pits nucleating inside the pit. Macro-topography includes the pit shape, depth and the thickness of the specimen. Interaction between multiple corrosion pits in a proximity can also accelerate fatigue crack initiation.
- **Strain and local plasticity** - Local plasticity causes slip bands to form, which induces crack nucleation. The plasticity is caused by a severe micro-topography which concentrates strain.
- **Hydrogen embrittlement** - As stated in section 2.2.3, HE can enhance brittle fracture, so crack initiation.
- **Chemical processes** - As stated previously, the effects of local chemical processes on the crack initiation is unclear. In experiments it is hard to study this part, because a lot of factors are involved.

2.5. Recapitulation

Pitting corrosion is one of the most dangerous forms of corrosion, due to the unpredictability, difficulty to detect, and the combined, synergetic effect with a fatigue loading, as can be seen in figure 2.11. The pitting process is widely studied, yet the pitting corrosion behaviour is hard to predict. Less widely studied is the effect of stress on the pitting corrosion process. Analytic models of pitting corrosion are available, but do not describe the pit shape, only depth, and do not implement all variables involved in the pitting corrosion process. Melchers' and Wangs model appear to give a good representation of the pit depth evolution in time, each validated for different field data. Melchers' model consists of four phases; phase one, the kinematic phase, is limited by the rate of oxygen diffusion through the water next to the corroding surface, phase two is controlled by the available oxygen going through the increasing thickness of the corrosion product and phase 3 and 4 are rapid and approximately steady-state conditions. Melchers gives parameters for pit growth based on data of 7 years of corrosion of S355 equivalent steel in the North Sea. Wang's model consists of three parameters dependent on the composition of the steel and salanity, temperature, dissolved oxygen and pH of the seawater. A large difference is found between the models of Wang and Melchers for periods of over 10 years. Numerical models that describe the pit growth are available, and some implement the effect of stress as well. These models describe the pit shape and micro-topography as well, but, if validated, most are only validated by experiments using stainless steels, without an applied stress.

The fatigue crack initiation process has been studied thoroughly, on a microscopic level as well as on larger scales. Initiation life determination methods are available, of which the strain-life method is the most used method, due to the ease of use compared to other methods. The strain-life method actually is a method to determine fatigue life, but due to the size of specimens used to determine the strain-life parameters, one can argue that the method predicts a (macro) crack of 1-2 mm in length, which is roughly the size of a crack that first can be discovered by using non-destructive testing methods. Predictions of smaller cracks (meso cracks) can be made using either strain-life characteristics of thinner test specimen, better detection methods for initiation, or using a different method as CDM. Dowling [59] tracked the crack length during strain-life experiments, and found that a crack length of 76 μm initiated at up to 10% of the fatigue life until failure. Plasticity was found to be a driving force for fatigue crack initiation, but the scale of the effect of plasticity on the fatigue crack initiation life in a corrosion pit is yet unknown. Because the strain-life method takes both into account, this method will be used in this research work. Another driving force for the pit-to-crack transition is hydrogen embrittlement.

In practice, several corrosion mitigation techniques are applied to offshore structures, which all are validated to decrease the corrosion process if applied correctly. The necessity of the application and the magnitude of application of these techniques is yet not fully known. This could mean that the application is over-conservative, and that the fabrication and maintenance costs can be lowered. This is due to a lack of understanding of the complete corrosion fatigue process.

Several models are available that determine the corrosion fatigue life, which also implement the pit-to-crack transition. This is done mainly by assessing the pit as either a small, or a large crack, i.e. by simplifying a pit shape to a 2D hemispherical/elliptical crack. These models are validated for pre-pitted specimens under a fatigue loading in a corrosive environment (NaCl solution), in which the fatigue loading is accelerated by the cyclic frequency, but the corrosion process is not accelerated in-situ, except for the pre-pitting beforehand. Validation of numerical or analytical models that include a fatigue loading in a corrosive environment is hard, due to the number of variables involved in the corrosion fatigue process. By considering the pit as a fatigue crack, a large number of these variables are not taken into account. The driving forces of the pit-to-crack transition where found to be: (i) Macro- and microtopography (i.e. geometry), (ii) dynamic strain, (iii) hydrogen embrittlement, and (iv) chemical processes. The effect of the latter was found to be unknown; either these processes could influence the crack initiation directly, or influence the corrosion process only, and thereby enhancing crack initiation. The effect of hydrogen embrittlement is neglected in this thesis on the effect of dynamic strain due to a lack of material data including hydrogen absorption, but it will be used in the fatigue life determination using strain-life curves. The effect of strain history is taken into account in this research work, just as the effect of the macro- and micro-topography, which is a combination that has not been done before according to this literature study.

3

Corrosion fatigue modelling methods

This chapter gives a description of the developed corrosion fatigue model. The model is built up according to the flowchart in figure 3.1. In the left column of the flowchart, the input parameters are shown, which will be discussed in section 3.1. In the right column, the model to determine the pit-to-crack transition is visualized. The model is split up in two parts in this section: (i) FEM model, which will be discussed in section 3.2, and (ii) damage accumulation model, which will be discussed in section 3.3. A general discussion on the developed corrosion fatigue model will be given in section 3.4.

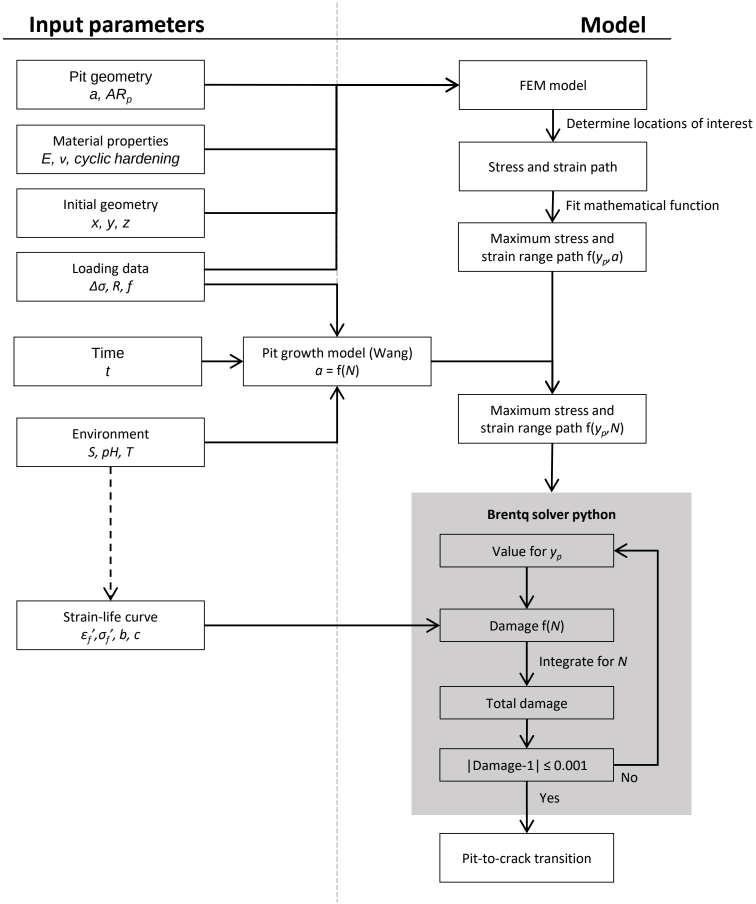

Figure 3.1: Flowchart of the corrosion fatigue model

3.1. Input parameters

It is of great importance to have a clear overview of which parameters are used as input in the developed corrosion fatigue model, because these parameters impact the confidence bounds of the outcome of the complete model. This section covers the choices of values for all input parameters, as listed in the flowchart in figure 3.1. First, the material properties are discussed; split up in elastic properties, plastic properties, and fatigue properties. Next, the pit growth parameters are discussed, which include pit geometry, pit growth model, and the environment. This section concludes with the loading data, and the initial geometry of the specimen. Chapter 6 discusses the sensitivity of the corrosion fatigue model on several input parameters.

3.1.1. Material properties

Hot-rolled S355 steel is typically used in offshore wind turbine foundations. To implement the material behaviour, elastic properties are required for static, linear calculations. For cyclic loads in the plastic region, cyclic hardening data is required as well. To determine damage at a certain strain range, Coffin-Manson-Morrow parameters for the strain-life curve are required. To select substantiated values for all parameters, different sources are gathered and compared for S355 steel. Preferably, material behaviour of steel in free corrosion (corrosive environment without an applied electrode potential) is used. This is because, due to hydrogen absorption, steel can behave more brittle in a corrosive environment than in air [9]. No specific enough stress-strain data related to hydrogen embrittlement of steel types in a corrosive environment has been found in the literature. Therefore, the effect of hydrogen absorption is not taken into account in the elastic and plastic material behaviour. Fatigue data of S355 steel in free corrosion has been obtained and will be implemented in the corrosion fatigue model. This section will not go into detail on the determination of all parameters. Appendices A and B show a more extensive description of the determination of the plastic hardening, and strain-life parameters.

Elastic properties

For all analyses the elastic material parameters from table 3.1 are used.

Parameter	Value	Unit
Young's modulus E	210,000	MPa
Poisson's ratio ν	0.3	-

Table 3.1: Elastic material parameters of S355 steel

Plastic properties

For plastic analyses, the hardening model proposed by Chaboche [99] is used. The model of Chaboche consists of an isotropic, and a kinematic part. The isotropic part of the hardening model defines the change in size of the yield surface σ^0 given the equivalent plastic strain $\bar{\epsilon}^p$. The kinematic part of the hardening model defines the change in back stress α, and results in translation of the yield surface. The parameters calibrated by Krolo et al. [100] for hot-rolled S355 steel are selected for this study. The parameters are listed in table 3.2. More information on the Chaboche hardening model, a comparison between multiple sources of stress-strain data of S355 steel, and an description of the implementation of the hardening parameters is given in appendix A.

No data has been found that includes the effect of hydrogen absorption on the stress-strain behaviour of steel. More research needs to be done in this field. Because of this, and because a large scatter between the (monotonic/cyclic) stress strain curves is found in appendix A, the influence of a scatter in this data on the results of the corrosion fatigue model needs to be studied. The sensitivity of the corrosion fatigue model on the stress-strain curve as input will be studied in chapter 6.

Fatigue properties

In this study, the strain-life method is used to describe the fatigue behaviour of the material. This low cycle fatigue method considers plastic strain next to elastic strain, which is expected to have an effect on the pit-to-crack transition. Another advantage of the strain-life method is that it is relatively easy to implement compared to other methods that predict fatigue crack initiation life.

Parameter	Value	Unit
Change in size of the yield surface $\sigma\|_0$	386	MPa
Maximum change in yield surface size Q_∞	20.8	MPa
Rate in yield surface change b	3.2	-
Kinematic hardening factor C_1	5327	MPa
Rate of change in kinematic hardening factor γ_1	75	-
Kinematic hardening factor C_2	1725	MPa
Rate of change in kinematic hardening factor γ_2	16	-
Kinematic hardening factor C_3	1120	MPa
Rate of change in kinematic hardening factor γ_3	10	-

Table 3.2: Chaboche hardening model parameters for S355 steel in air [100]

The strain-life curve used in this study includes the effect of a corrosive environment, and can be used to predict fatigue crack initiation life of cracks of about 0.076 mm. Strain-life data of Mrozinski et al. [101] is multiplied by a factor to compensate for a corrosive environment, and a factor to compensate for fatigue crack initiation life of a crack length of 76 μm. The result of this factorization is the strain-life curve that will be used in this study.

Results of low cycle fatigue experiments of Dowling [59, 102] are used to determine a factor of the fatigue crack initiation life over the total fatigue life found by strain-life experiments. Based on a study by Bignonnet et al. [76], a factor between strain-life curves in air and free corrosion is determined. The strain-life parameters fitted on the data found after factorization are given in table 3.3, and the curve is shown in figure 3.2. A more detailed description on determination of the strain-life curve can be found in appendix B. Because more research is needed on the fatigue behaviour of specimens in free corrosion, and on the determination of initiation in these experiments, the sensitivity of the corrosion fatigue model on the strain-life curve as input will be studied in chapter 6.

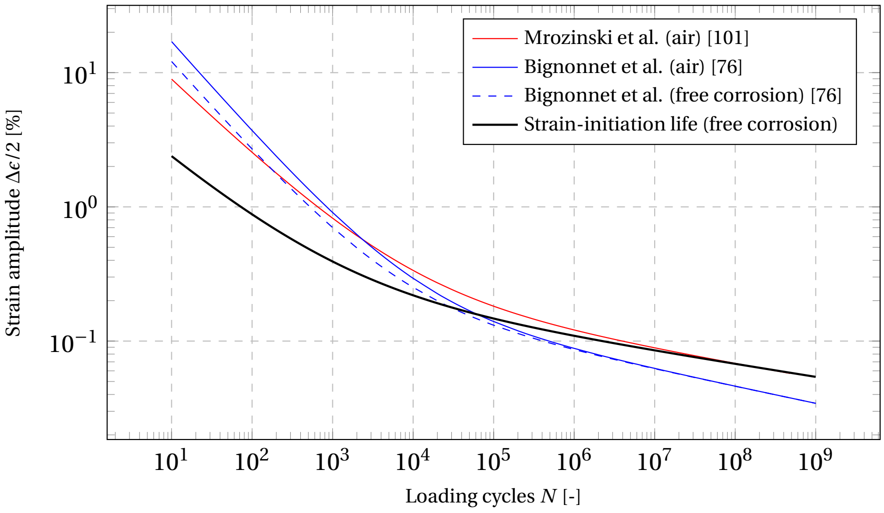

Figure 3.2: Final strain-initiation life curve in combination with original strain-life curves

Parameter	Value	Unit
Fatigue strength coefficient σ'_{f}	838	MPa
Fatigue ductility coefficient ϵ'_{f}	0.0982	-
Fatigue strength exponent b	-0.0952	-
Fatigue ductility exponent c	-0.519	-

Table 3.3: Coffin-Manson-Morrow parameters for free corrosion conditions and a failure criterion of a crack length of about 76 μm

3.1.2. Environment and pit growth parameters

Two analytical models to estimate the pit depth development in time are obtained from literature, as discussed in chapter 2. The model of Wang et al. [26] is implemented in this thesis because of two reasons: (i) from multiple experiments it is found that the pit growth rate is decreasing over time, which corresponds to the model of Wang and not to the model of Melchers [12] in which the pit growth stays constant after a certain amount of time, and (ii), the model of Wang is more simple in use, and also adaptable to different environments by the parameters: salinity, dissolved oxygen, pH and temperature. Because of the large difference in the pit depth over a large amount of time between the pit growth models, the pit growth model will be taken into account in the sensitivity study in chapter 6.

The parameter determination using environmental data for the pit growth model of Wang is based on experiments of A3 steel, of which the alloy composition is shown in table 3.4 together with the alloy composition of different hot-rolled S355 steel types. It can be concluded that the steel type A3 is comparable in alloy composition to S355 steel. Therefore, the pitting corrosion behaviour of A3 steel is assumed to be comparable to S355 steel.

Steel type	Source	C	Mn	S	P	Si	Cu	Ni
S355J0	NEN-EN-10025-2 [8]	≤0.2	≤1.60	≤0.030	≤0.030	≤0.55	≤0.55	-
A3	Wang et al. [26]	0.2	0.55	0.009	0.015	0.26	-	-
S355N	De Jesus et al. [65]	0.10	0.64	0.041	0.022	0.15	0.38	0.095
CSA 350W	Ghahremani [103]	0.23	0.50-1.50	0.05	0.04	0.35	-	-
S355	Mrozinski et al. [101]	-	-	-	-	-	-	-
S355	Krolo et al. [100]	0.16	1.36	0.007	0.015	0.021	0.04	0.02
E355	Bignonnet et al. [76]	0.11	1.45	0.001	0.02	0.3	-	0.42

Table 3.4: Steel composition in weight-percentage

Table 3.5 shows environmental data of the North Sea and at the bay of Qingdao, China. At Qingdao, experiments with A3 steel coupons in sea water have been performed. From the data it can be seen that the two locations do not differ much, except for the temperature. The difference in temperature results in a different value for d_m, which equals the maximum pit depth after an infinite amount of time. The equation to determine pit growth in time using this model is shown in equation (3.1), where a is the current pit depth, t is time, and d_m, m, and α are model parameters determined in table 3.5.

Location	T [°C]	Dissolved O_2 [mL/L]	Salinity [wt.%]	pH [-]	d_m	m	α
Qingdao [26]	13.6	5.57	3.2	8.16	3.00	0.722	0.199
North Sea [104–106]	11.0	5.60	3.301	8.0	2.72	0.722	0.195

Table 3.5: Data of Qingdao and North Sea compared including Wang pit growth model parameters

$$a(t) = d_\mathrm{m}\{1 - \exp\left(-(\alpha t)^m\right)\} \tag{3.1}$$

3.1.3. Loading data

Many factors are involved in the determination of a load spectrum of wind turbine foundations. Multiaxial fatigue effects are neglected in this study for simplicity. This study does not address variable fatigue load spectra. The load is simplified to a constant amplitude, uniaxial load with a sinusoidal shape. To define a constant amplitude load, a maximum stress or stress amplitude is necessary in combination with a stress ratio. The stress ratio is defined accordingly equation (3.2).

$$R = \frac{\sigma_\mathrm{nom,min}}{\sigma_\mathrm{nom,max}} \tag{3.2}$$

For wind turbine foundations, relatively high stress ratios are found. Especially in welds, where a residual stress will increase the mean stress compared to the base material. Therefore, for this study a stress ratio of 0.5 is chosen.

To couple the corrosion process to the fatigue process, time is an important parameter. The fatigue life is typically given in a number of cycles. To couple the number of cycles to time, the frequency of a load cycle needs to be determined. In this study, a frequency of 0.2 Hz is chosen, which corresponds to the average frequency of waves in the North Sea. It is not specified whether waves are the main contributor to the load spectrum of wind turbine foundations, and in what extent wind, the motion of the wind turbine blades, or other factors influence the load spectrum. Because of this uncertainty, the stress ratio R, and frequency f, will be taken into consideration in the sensitivity study in chapter 6.

3.1.4. Geometry

Monopiles built in the North Sea typically have a diameter of 6-8 metres and a length of over 40 metres [107]. The wall thickness of monopiles of state-of-the-art windturbines is mostly kept secret by manufacturers. For this study, a wall thickness of 60 millimetres is chosen, which corresponds to a diameter over wall thickness ratio of approximately 100 to 130. The full size of the wind turbine foundation will not be modelled. This would result in a very large computation time due to the large number of elements that should be used to model a wind turbine foundation in combination with a corrosion pit of several millimetres in size. The dimensions of the model in x-, and z-direction are based on the study of Cerit et al. [84]. Cerit et al. chose the dimensions of their FEM model such that the width and breadth of the model did not influence the results. The chosen dimensions of the FEM model are shown in table 3.6.

Coordinate	Value	Unit
x-direction	250	mm
y-direction	60	mm
z-direction	150	mm

Table 3.6: FEM model dimensions

In figure 3.3, the coordinate system of the FEM model relative to the monopile structure is shown. The curvature of the monopile is neglected in the FEM model, because the curvature is in the tangential direction, while the uniaxial loading is applied in axial direction of the monopile, which equals the x-direction of the FEM model. Therefore, no effect of the curvature on the stress and strain level is expected for this type of loading.

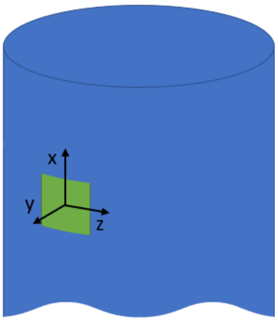

Figure 3.3: Coordinate system of FEM models. In green the modelled piece, the wall thickness is not shown for clarity.

The shape of the corrosion pits included in this study are defined using an aspect ratio AR_p, according to

$$AR_\mathrm{p} = \frac{a}{2c} \tag{3.3}$$

where a is the pit depth (in the negative y-direction), and $2c$ is the pit diameter (in the x-, and z-direction). The shape of perfectly elliptical corrosion pits is chosen as circular in the xz-plane, and elliptically shaped in the xy, and yz-plane. In this study, three different pit shapes are considered: a circular pit shape of $AR_\mathrm{p} = 0.5$, a more blunt pit shape of $AR_\mathrm{p} = 0.25$, and a more sharp pit shape of $AR_\mathrm{p} = 1.0$.

Surface roughness
This study will also investigate the effect of surface roughness on the pit-to-crack transition. To determine this effect, a different geometry will need to be modelled to obtain the effect of the roughness on the stress and strain distribution. To reduce calculation time, the roughness is only applied locally by means of a micro-pit. The micro-pit is located in the bottom of the corrosion pit. The corrosion pit is still a circular or elliptical shaped pit. The micro-pit will always have a circular shape of $AR_\mathrm{p} = 0.5$. The depth of the micro-pit will be a fraction of the depth of the corrosion pit, and therefore also scale with the pit growth of the corrosion pit. In this study, three different micro-pit depth over corrosion pit depth fractions (a_micro/a) will be tested: 0.01, 0.05 and 0.1.

3.2. FEM model

This section elaborates on the implementation of the FEM model in the developed corrosion fatigue model. The goal of the FEM model is to find the distribution of stress and strain around the surface of a corrosion pit and below. The FEM model will be created using Abaqus FEA. The computation time can be very large using FEA, and therefore, in each of the following sections, considerations will be made to reduce the computation time if possible. The FEM models are built up using scripting, which is supported by Abaqus FEA. Scripting is a useful tool to efficiently perform parametric studies.

Two types of models are created, a planar (2D) model, and a solid (3D) model. The 3D model will be created for two different types of geometries, i.e. perfectly elliptic/circular corrosion pits, and corrosion pits including surface roughness (micro-pit). In the corrosion fatigue model, the 3D model will be used only. To substantiate choices, the 2D model is used in some cases, because the computation time is significantly shorter. The dimensions of the FEM model are given in section 3.1.4. The planar FEM model only includes the x-, and y-directions. In 3D, only a quarter of the complete FEM model is implemented, to minimize computation time. The centre of the corrosion pit is always positioned at (0.0, 0.0, 0.0) mm.

3.2.1. Geometry convergence study

The width (z-direction) and length (x-direction) of the FEM model are chosen accordingly the research of Cerit et al. [84]. The length of the FEM model is larger than the width of the material, and because the width (z-direction) is perpendicular to the loading direction (x-direction), which results in higher strain and stress levels the locations in the corrosion pit with the highest x-coordinates, the width is a more critical parameter. To verify that these dimensions do not influence the stress and strain levels due to the presence of a corrosion pit, a FEM model including a larger width of 300 mm is evaluated. The 3D FEM calculation is performed for an aspect ratio of 0.25, because for this aspect ratio the pit width is largest compared to the pit depth. A transient analysis is performed for an applied static load of 1 MPa.

The distribution of stress over the pit surface is shown in figure 3.4. Figure 3.5 shows the distribution of stress below the surface of the corrosion pits. From both figures it can be seen that the influence of a larger width on the stress and strain levels is negligible. It can be concluded that this will also be the case for different aspect ratios, where the width with respect to the depth is lower.

3.2.2. Boundary conditions and load application

The correct application of boundary conditions on a FEM model is of great importance to obtain realistic results. The planar FEM model including boundary conditions and loads is shown in figure 3.6a. The corrosion pit is the centre of the coordinate system. The edge at $x = -125$ mm is fixed in the x-direction. The point $(-125, 0, 0)$ mm is fixed in the y-direction as well to prevent the model from being unstable. The load is applied at $x = 125$ mm.

The solid FEM model including boundary conditions and loads is shown in figure 3.6b. The corrosion pit is the centre of the coordinate system. The faces at $x = 0$ mm are fixed in the x-direction, and around the y-, and z-axis. The faces at $z = 0$ mm are fixed in the z-direction and around the x-, and y-axis. This way symmetry is created at these faces. The point $(-125, 0, 0)$ mm is fixed in the y-direction as well to prevent the model from being unstable. The load is applied at the face at $x = -125$ mm.

The applied load is either static or cyclic. Cyclic loads are applied according to a sinusoidal shape and require a maximum stress $\sigma_{\mathrm{nom,max}}$ and a stress ratio R.

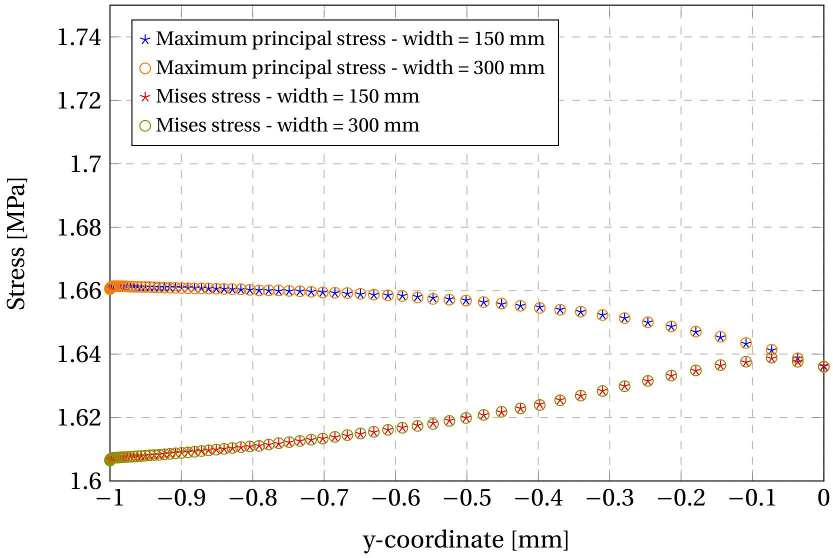

Figure 3.4: Stress distribution along the pit surface for different widths of the 3D FEM model for an aspect ratio of 0.25

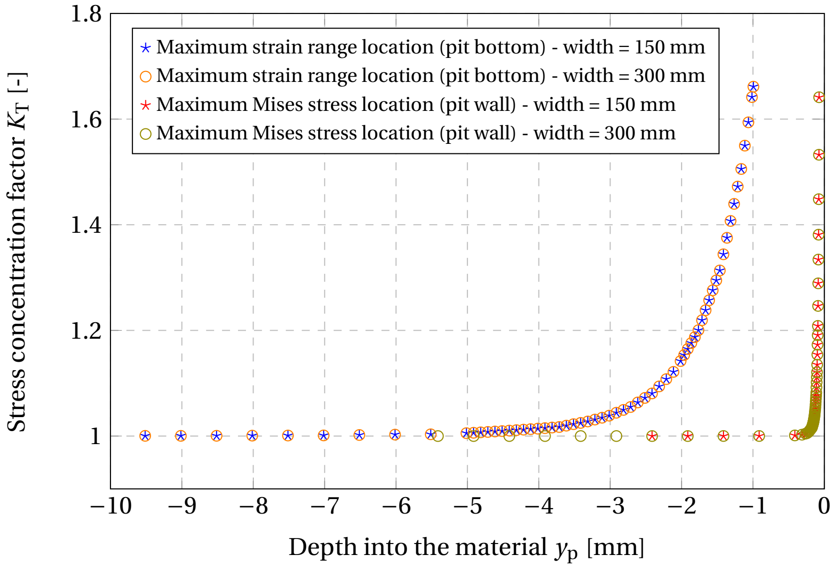

Figure 3.5: Stress concentration factors for a stress path from the pit surface into the material for different widths of the 3D FEM model for an aspect ratio of 0.25

3.2.3. Mesh

The mesh of a solid FEM model exists of either hexahedron elements (cubes) or tetrahedron elements (pyramids). Because hexahedron elements typically are very robust compared to tetrahedron elements in non-linear calculations, hexahedron elements are chosen in this study. Mesh refinements have been applied along the pit surface, as can be seen in figure 3.7 for the 2D model, in figure 3.8 for the 3D model without surface roughness, and in figure 3.9 for the 3D model including surface roughness. The mesh around the pit surface is refined compared to the outer edge of the models. To structure the mesh of the 3D model, a box of partitions is created around the pit, such that the elements outside the box can be rectangular or square, and the number of elements is decreased. The partitions can be seen more clearly in figure 3.6. For both the 2D and 3D model, a number of partitions have been created below and parallel to the pit surface. This way the rate by which the stress is decreasing below the surface of the pit, which is called the stress gradient, can be determined correctly. More of these partitions can be created if pit growth steps are implemented. Pit growth steps will be discussed in section 3.2.5.

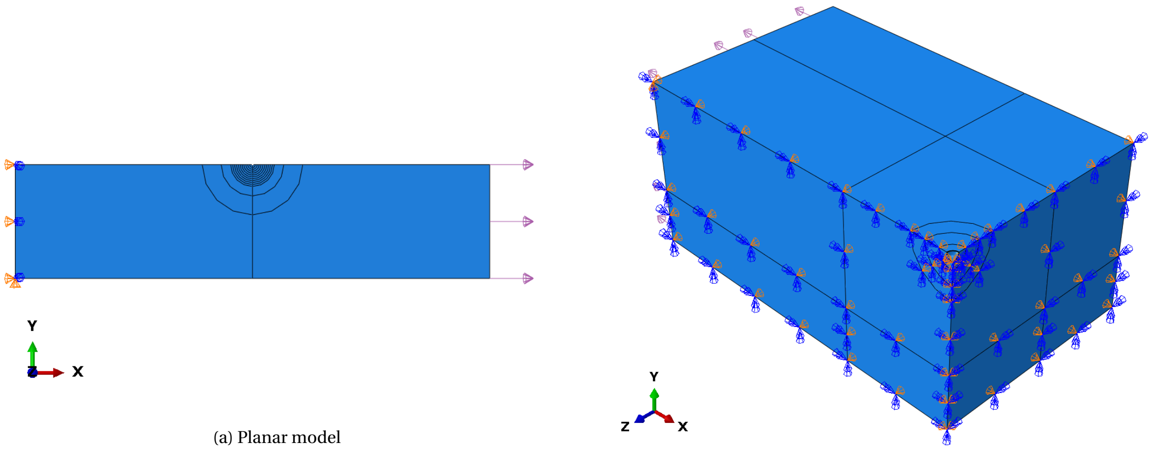

(a) Planar model

(b) Solid model

Figure 3.6: Boundary conditions and load application

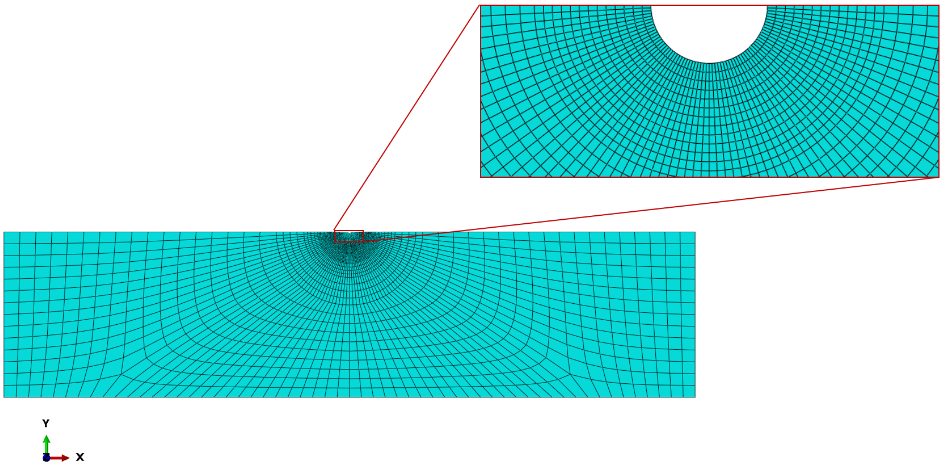

Figure 3.7: Planar model mesh

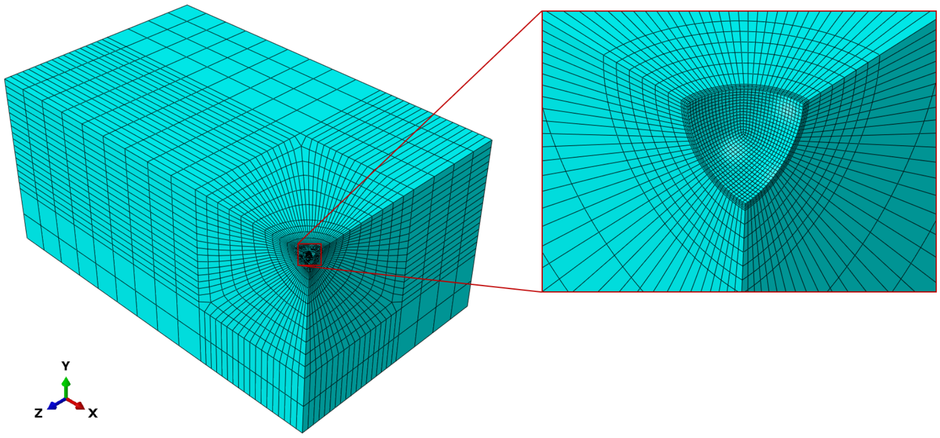

Figure 3.8: Solid model mesh

Mesh convergence study

To optimize the mesh to converged results and a minimal calculation time, a mesh convergence study is performed. The convergence study is performed for the 2D and 3D models without roughness. The micro-pit in the 3D model including surface roughness will be regarded as a corrosion pit, i.e. it will contain the

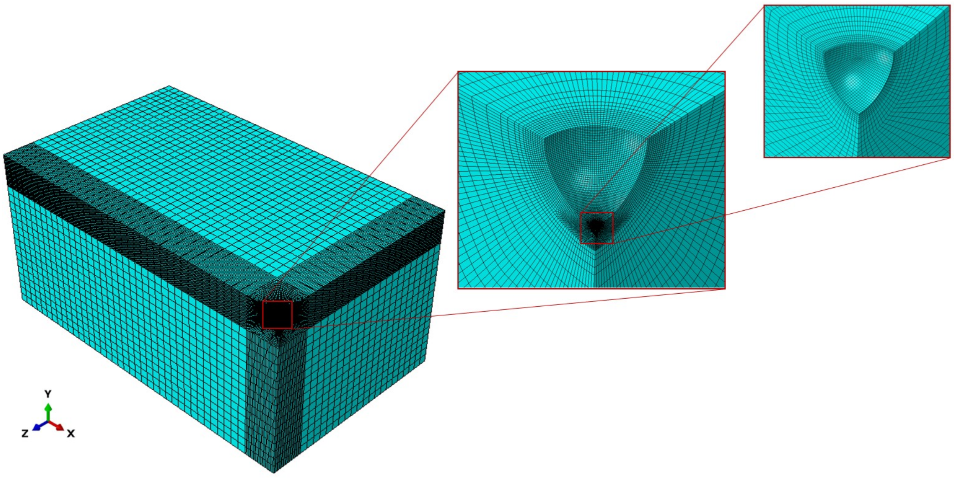

Figure 3.9: Solid model mesh including surface roughness

same number of elements as will be found for corrosion pit in the 3D model without surface roughness.

Models are created with different mesh sizes, different factors between the mesh size at the outer edge of the model and the pit surface, and either linear or quadratic elements. All models are of equal geometry, for which the pit depth a and width c are 0.25 mm. Results are shown for the stress concentration factor K_T, determined from the maximum principal stress, against the number of degrees of freedom (DoFs) in figure 3.10a and 3.10b for the 2D, and 3D model without surface roughness respectively. In these figures, CPS4R corresponds to linear plane stress elements, CPS8R to quadratic plane stress elements, C3D20R to quadratic solid elements, and C3D8R to linear solid elements. All elements have a reduced number of integration points to reduce the computation time. The chosen mesh size and element type are marked in red and are 5 mm at the outer edge for the planar model with a mesh factor of 400 and 10 mm at the outer edge for the solid model with a mesh factor of 200 between the element size at the outer edge of the model and at the pit surface. For both models quadratic element types are selected with a reduced number of integration points.

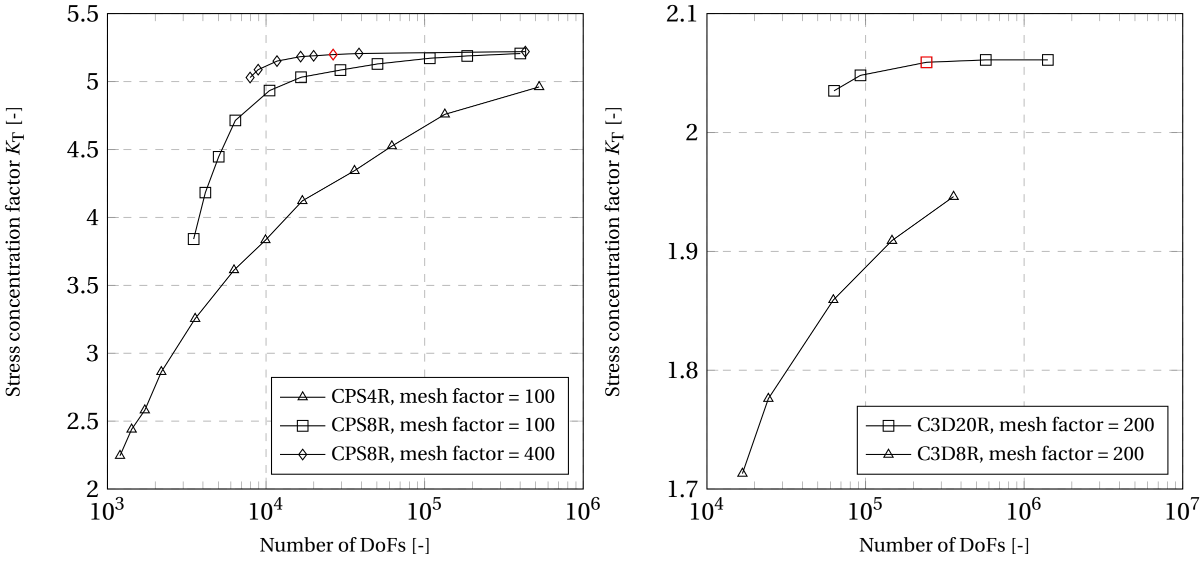

(a) 2D model

(b) 3D model

Figure 3.10: Mesh convergence study - a = 0.25 mm, 2c = 0.5 mm

Because the stress below the surface is of importance to the corrosion fatigue life in this model, the mesh should not only be converging at the pit surface, but also below the surface of the corrosion pit. Therefore, a convergence study is performed for the stress along a path from a fixed location at the pit surface into the material. Two locations at the pit surface will be chosen, the pit bottom and the maximum strain range location. The maximum strain range location is equal to the maximum stress location for linear FEM calculations. Only of the 3D model the stress and strain below the surface of the corrosion pit will be used. Therefore this convergence study is only done for the 3D FEM model. A pit with an aspect ratio of 1.0 is considered.

The results for the mesh as determined using figure 3.10 and a refined mesh of half the element size is shown in figure 3.11. It is found that both lines follow the same slope, but the refined mesh results in a more smooth curve. In the post-processing of the results, a function will be fitted on the stress and strain data points. This way, the irregularities in the stress path of the non-refined mesh will be smoothed out. Therefore, the non-refined mesh is assumed to be fine enough.

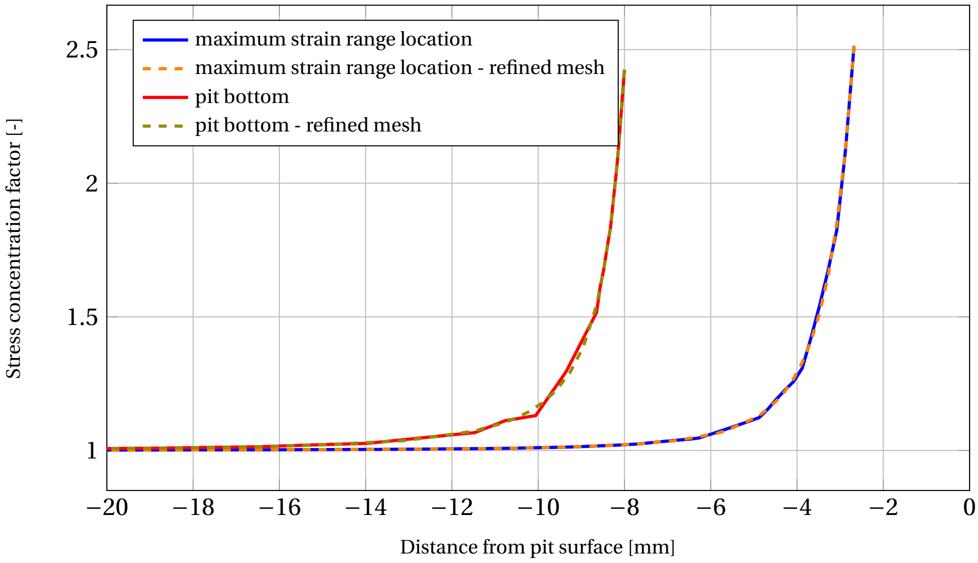

Figure 3.11: Mesh convergence study of the stress gradient for the solid model and $AR_\mathrm{p} = 1$

3.2.4. Time steps

The applied load will either be static or cyclic. For static loads, a transient analysis with a variable step size, determined by the solver, will be used to solve the problem. The initial step size depends on the applied load. For loads beyond the yield stress, smaller step sizes are required, where for loads in the elastic region, one step will be sufficient.

For cyclic loads, two options are available in Abaqus FEA: (i) a transient analysis with a small step size, and (ii) a direct cyclic method. The direct cyclic method is a quasi-static analysis, which uses a combination of Fourier series and time integration of the non-linear material behaviour to obtain a stabilized response of the structure iteratively [108]. This method returns a converged result significantly faster than the transient method for a cyclic analysis. Due to the solving method, the stabilized hysteresis loop can shift horizontally or vertically, which could be unrealistic. This means that the mean stress and strain is not predicted correctly, however the stress and strain ranges are predicted correctly.

A comparison between the direct cyclic method and the transient method has been made for a stress ratio of 0.5 using different aspect ratios in the solid model. Resulting hysteresis loops can be found in figure 3.12. The applied load is such that the mean stress is just below the yield stress in the perfectly elliptical pit. For this analysis, the mean stress is applied using the transient method prior to the cyclic load, which resulted in more accurate results using the direct cyclic method. The resulting maximum principal stress and principal strain ranges can be found in table 3.7. From these values the fatigue initiation life using the strain-initiation life curve in free corrosion has been calculated including Smith-Watson-Topper mean stress correction. The differences in fatigue initiation life have been listed in table 3.7. The difference is mainly due to the difference in maximum stress, but is assumed to be low enough to be able to use the direct cyclic method for a stress ratio of 0.5 to reduce computation time.

3.2.5. Pit growth steps

The FEM model is built as such, that it is possible to delete rows of elements during the analysis to simulate pit growth in time of perfectly elliptical pits. This way, plasticity can already be introduced in certain elements,

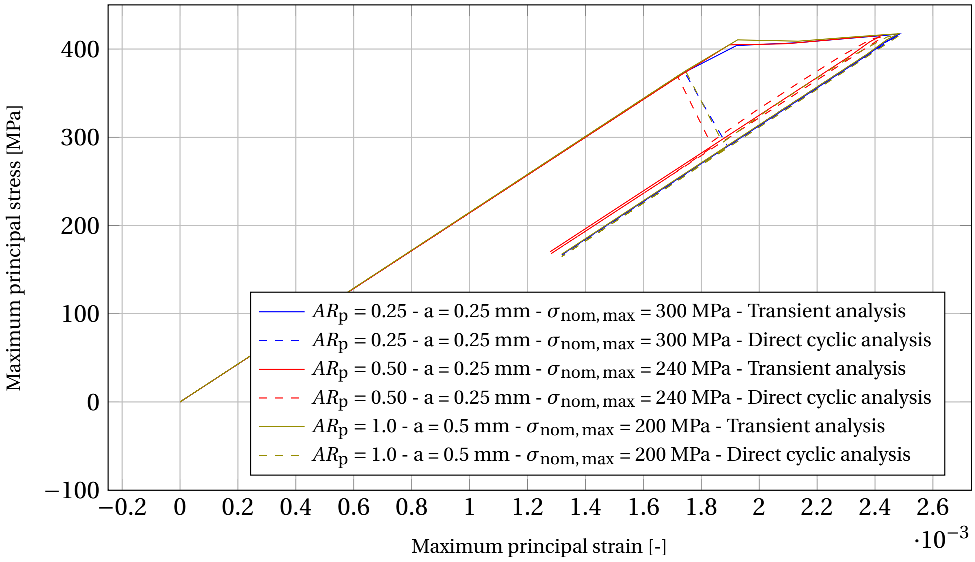

Figure 3.12: Hysteresis loops at the pit bottom of perfectly elliptical pits using direct cyclic and transient analysis for three aspect ratios

AR_p [-]	a [µm]	Analysis type	$\sigma_{\mathrm{nom,\,max}}$ [MPa]	$\Delta\epsilon_{\mathrm{last\,cycle}}$ [%]	$\sigma_{\mathrm{max,\,last\,cycle}}$ [MPa]	N_i [-]	Difference in N_i [%]
0.25	250	Transient	300	0.11621	416.93	667386	+1.48%
		Direct cyclic		0.11616	415.79	677284	
0.50	250	Transient	240	0.11462	415.73	721177	+2.46%
		Direct cyclic		0.11462	413.57	738913	
1.00	500	Transient	200	0.11625	417.24	664024	+2.10%
		Direct cyclic		0.11638	414.91	677997	

Table 3.7: Comparison of 3D transient and direct cyclic analyses for different aspect ratios for $R = 0.5$

before the elements appear at the surface of a pit. As a result, it could be that due to plastic hardening, the hysteresis curve is translated (kinematic hardening) or expanded (isotropic hardening) differently than without pit growth steps (without the history of plastic strains). To investigate this, transient analyses have been performed of the planar FEM model for a perfectly circle shaped pit ($AR_\mathrm{p} = 0.5$). The analysis is done at two stress ratios, -1.0 and 0.1, including pit growth steps with an initial pit depth of 250 µm, and a maximum pit size of 312.5 µm, or without pit growth steps and a pit depth of 312.5 µm. The number of pit growth steps is varied, so that it can be concluded if convergence in the pit growth step size has been obtained. The analyses are performed for 20 consecutive cycles per pit growth step, to obtain the stabilized hysteresis loops. For plasticity to occur in multiple rows of elements surrounding the pit wall, a high applied maximum stress of 250 MPa has been chosen. The resulting hysteresis loops for five, and no pit growth steps are shown in figure 3.13. The corresponding strain ranges and maximum stress values of the last cycle of the hysteresis loops are shown in table 3.8. The strain ranges and maximum stress values of the last load cycle are used in combination with the strain-initiation life curve in free corrosion and the mean stress correction of Smith-Watson-Topper, to calculate fatigue crack initiation life. The resulting fatigue initiation life and the difference in fatigue initiation life between the analyses including pit growth steps and excluding pit growth steps is shown in table 3.8.

From the results for a stress ratio of -1.0, it appears that the fatigue crack initiation life is converging for smaller pit growth step sizes. The converged result does not equal the number of cycles to fatigue crack initiation without any pit growth steps, but is between 2-3% higher. For a stress ratio of 0.1, the difference in fatigue crack initiation life is smaller for smaller step sizes, but the result has not clearly converged yet. Due to the very small differences in strain and stress levels in these calculations, the difference in fatigue crack initiation life with pit growth steps, and without pit growth steps, is below 1% for all step sizes. Based on these results, it can be concluded that the effect of (plastic) strain history on hysteresis loops is negligible.

Therefore, no pit growth steps will be implemented in the FEM model to consider the effect of stress, and strain history on the stress, and strain levels.

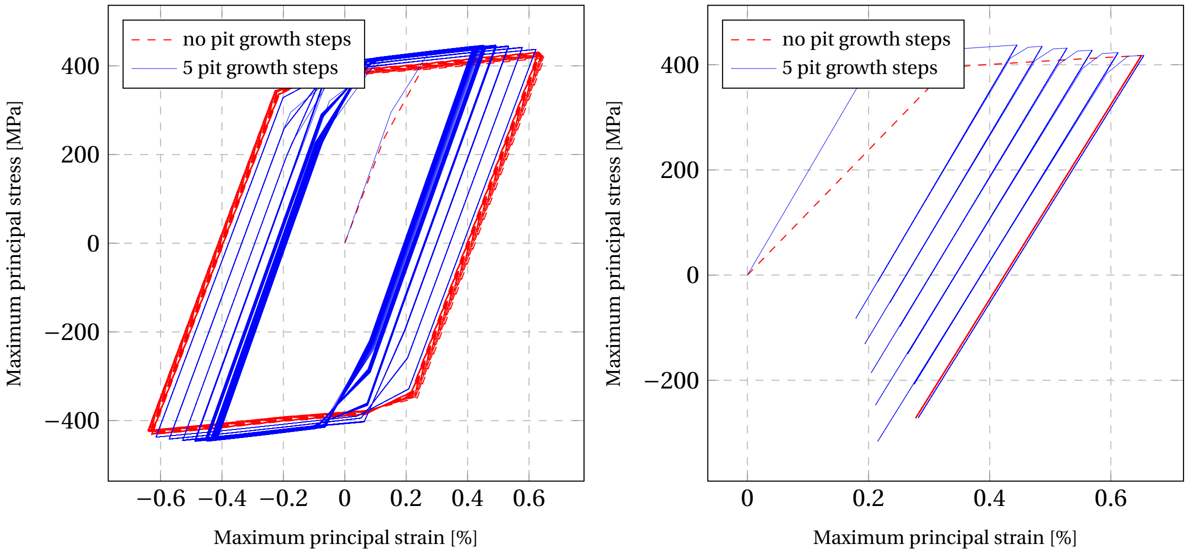

(a) $R = -1$

(b) $R = 0.1$

Figure 3.13: 2D transient analysis for $AR_\mathrm{p} = 0.5$ and $\sigma_\mathrm{nom,\,max} = 250$ MPa - for each pit growth step 20 consecutive cycles are shown, of which the last is assumed to be stabilized

Stress ratio [-]	$\sigma_\mathrm{nom,\,max}$ [MPa]	Pit growth steps [-]	a_initial [µm]	$\Delta\epsilon_\mathrm{last\,cycle}$ [%]	$\sigma_\mathrm{max,\,last\,cycle}$ [MPa]	N_i [-]	Difference in N_i [%]
-1.0	250	0	312.5	1.25786	437.42	267	
		5 times 12.5 µm	250	1.23760	431.10	285	+6.74%
		10 times 6.25 µm	250	1.23801	437.77	276	+3.37%
		15 times 4.17 µm	250	1.24059	437.84	275	+3.00%
0.1	250	0	312.5	0.37245	417.53	6980	
		5 times 12.5 µm	250	0.37311	417.99	6918	-0.89%
		10 times 6.25 µm	250	0.37315	417.75	6928	-0.74%
		15 times 4.17 µm	250	0.37318	417.50	6939	-0.59%

Table 3.8: Comparison of transient 2D analyses for AR_p=0.5 with and without pit growth steps

3.2.6. Verification

This subsection focusses on verification of the FEM models through comparison to analytic SCF formulae. For these calculations, the thickness of the 2D and 3D model (in y-direction) is chosen to be 150 mm, which is equal to the dimensions used by Cerit et al. [84], for comparison reasons. A static load of 1 MPa is applied in the FEM models, and the resulting maximum principal stress at the pit surface is extracted to determine the SCF. For the planar model, both plane strain as plane stress element types have been considered.

Figure 3.14 shows SCFs for constant pit width and different pit depths for a through-thickness pit (2D model) and a pit (3D model) without surface roughness. In figure 3.14a, it can be seen that the use of plane strain elements results in lower stresses than the use of plane stress elements for $a \geq 0.1$. This difference can be expected, because plane stress elements allow strain in the in-plane direction, which corresponds to a thin plate, and plane strain elements do not, which corresponds to a thick plate. A good agreement between analytic SCF formula by Inglis et al. [109] and the numerical SCF results of the through-thickness pit is found. For the 3D model, the numerical results and the analytic SCF formulae of Cerit et al. [84] and Ahn et al. [110] show less agreement, but the relation follows the same curve. A reason for the underestimation of the SCF has not been found.

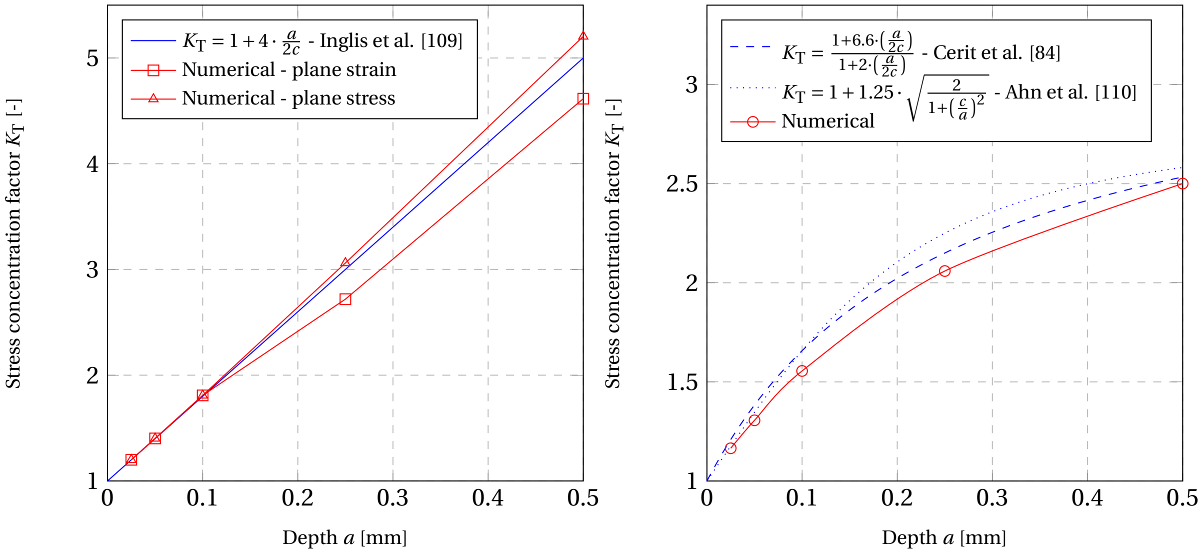

(a) Through-thickness notch (planar model)

(b) Notch results (solid model)

Figure 3.14: Stress concentration factors for constant pit width $2c = 0.5$ [mm]

Table 3.9 shows the SCFs for a corrosion pit including a micro-pit in the pit bottom for different micro-pit depth over pit depth fractions. The calculations are performed for a pit depth of $a = 0.5$ mm and a width of $2c = 1.0$ mm. The values are compared to results of Cerit et al. [84], who performed the calculations for different pit depths, but Cerit et al. found that the pit depth was no factor in the determination of SCF formulae of corrosion pits. The difference between the SCFs of this study, and the SCFs of Cerit et al. was found to be around 0.5%.

AR_p [-]	a_{micro}/a [-]	K_T [-] - FEM	K_T [-] - Cerit et al. [84]	Difference in K_T
0.50	0.1	3.820	3.80	+0.53%
	0.05	3.972	3.99	-0.45%
	0.01	4.301	-	-

Table 3.9: SCFs of perfectly circular pits including a micro-pit at the pit bottom

3.3. Damage accumulation

This section discusses all steps following the FEM model until the final pit depth and fatigue crack initiation life, which is displayed in figure 3.1. This includes the extraction and usage of stress and strain from the FEM model, implementation of the pit growth model and strain-life relation in these results, and finally the solving of the equation to find the final pit depth and time at which a crack will initiate at the surface of the corrosion pit. In terms of the competition between the fatigue process and corrosion process, this is the point where the fatigue process will start to dominate the corrosion fatigue process. First a general overview of the method to determine the pit-to-crack transition will be given. Next, the implementation and considerations in the implementation of this method into the corrosion fatigue model will be discussed.

Method

Stresses and strains can be extracted from the FEM model. The maximum principal variant of both stress and strain will be used for all calculations. By subtracting the minimum strain from the maximum strain at a node or other location, the strain range is determined. Using the maximum stress and strain range, the strain-life relation can be used to estimate the fatigue life. In this study, the Smith-Watson-Topper mean stress correction will be implemented to compensate for stress ratios other than -1. The strain-life relation including Smith-Watson-Topper mean stress correction is shown in equation (3.4).

$$\sigma_{\max}\frac{\Delta\epsilon}{2}=\frac{\sigma'_{\mathrm{f}}}{E}(2N_{\mathrm{f}})^{b}+\sigma'_{\mathrm{f}}\epsilon'_{\mathrm{f}}(2N_{\mathrm{f}})^{b+c} \tag{3.4}$$

where σ_{max} is the maximum stress in a load cycle. Fatigue damage is accumulated using Miner's Rule [111]:

$$D=\sum_{j=1}^{k}\frac{n_j}{N_{i,j}} \tag{3.5}$$

where D is the damage fraction, n_j is the number of cycles accumulated at stress range $\Delta\sigma_j$ or strain range $\Delta\epsilon_j$, and $N_{i,j}$ is the number of cycles until fatigue crack initiation at stress or strain range j. Miner's Rule is a linear summation rule of cyclic ratios. In essence, the rule assumes that the amount of damage is independent of the loading range at any given fraction of the fatigue life. Because in this model, the strain-life curve represents the fatigue crack initiation life instead of the total fatigue life, the rule in this model results in the finding of an equal crack size for all applied loading ranges.

The validity of this rule in this application may be questionable due to sequence effects. In this study, a constant amplitude load is implemented, but the geometry of the specimen is changing due to the pit growth. This results in an increasing loading range at a given point in the material at which a crack will initiate once it surfaces at the corrosion pit due to pit growth. Miner's Rule tends to be conservative for this sequence of loading ranges, but this depends on the stress ratio according to Pereira [112]. In this research work, non-linear damage accumulation models have not been investigated further and Miner's Rule is assumed to be valid for this application.

Implementation

Ideally, for each element or node in the mesh of the FEM model, damage is memorized and accumulated. This way initiation can occur at any location in the specimens and no assumptions or estimations have to be made for this. This would mean that every function of the damage accumulation model should be implemented in Abaqus FEA, because it would take a lot of time to implement a FEA method in a programming language. It has been found a possibility to implement the damage accumulation model in the framework of Abaqus scripting. By implementing all functionalities into Abaqus FEA, a step size needs to be determined. At each pit growth step the pit expands according to this step size. The mesh size at the pit surface needs to be equal to this mesh size to be able to perform the pit growth steps. To determine the minimum size of the step size without too much computation time, this concept is implemented in Python using a constant pit growth rate and different step sizes. The result is shown in figure 3.15 for two different pit aspect ratios. From this theoretical case it can be found that the minimum step size to obtain a reasonably converged result should be 0.005 mm. Compared to a maximum pit size of 2.76 mm, this could require over 500 pit growth steps, which results in a significant amount of computation time. Therefore the implementation of pit growth steps in the FEM model is not feasible.

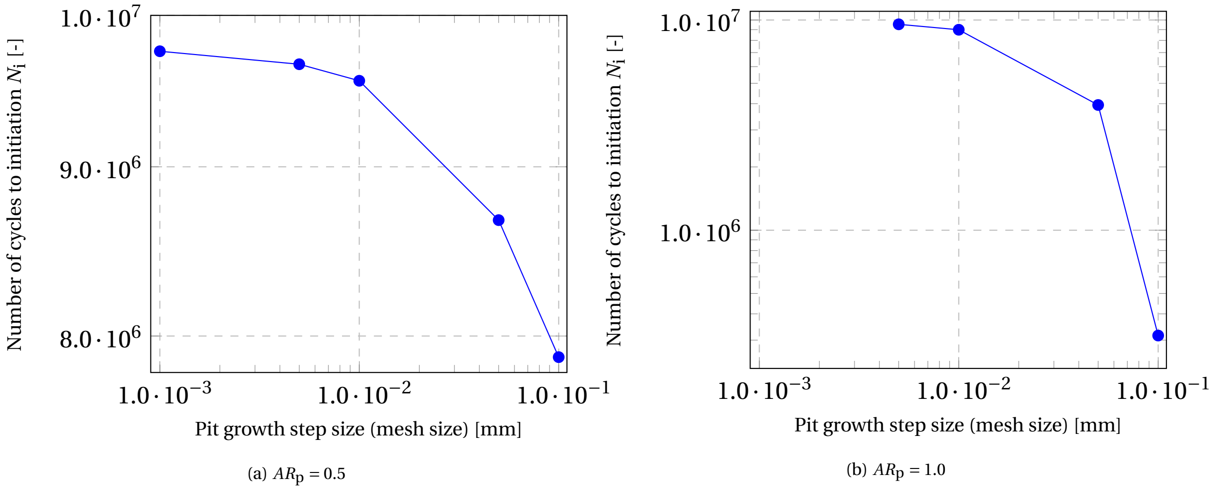

(a) $AR_{\mathrm{p}}=0.5$ (b) $AR_{\mathrm{p}}=1.0$

Figure 3.15: Convergence study on the pit growth step size. Number of cycles to fatigue crack initiation are determined for an equal applied loading and two different pit shapes using pit growth steps in a Python script.

To reduce the amount of computation time, interpolation between pit growth steps could be implemented. Because it is not trivial to implement this in Abaqus FEA, the stress and strain results are exported from Abaqus FEA into Python.

First, the maximum strain range location is determined by subtracting the minimum value of the maximum principal strain from the maximum value of the maximum principal strain of all nodes along the pit surface. For perfectly elliptical pits, this is initially assumed to be the location of fatigue crack initiation. Of this location a path will be created that goes into the material, of which a visualization has been given in figure 3.16. The stress/strain path from the pit bottom will be directed perpendicular to the y-axis. The stress/strain path from the maximum strain range location is directed into the material in such a way that the fraction of x/y_p is always equal. This way the line crosses the maximum stress range location for each pit depth, because it has been found that for a pit depth up to at least 8 mm, and a specimen thickness of 60 mm, the strain distribution along the pit surface is not affected by the thickness. Also note that y_p is always perpendicular to the y-axis, and therefore the gradients of the resulting graphs of stress/strain-paths from the pit bottom can not be compared to graphs of stress/strain-paths from the maximum strain range location. This can only be done if the distance to the pit surface is used as parameter instead of y_p.

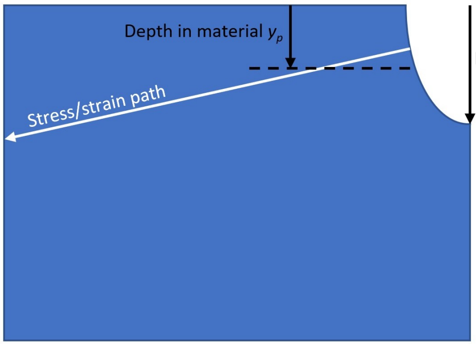

Figure 3.16: Visualisation of an example of a stress/strain path from a maximum strain range location

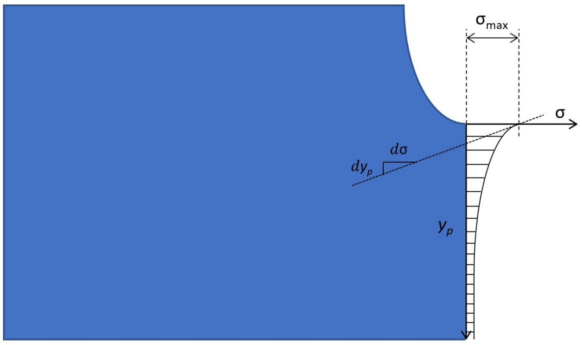

Figure 3.17: Visualisation of the stress gradient $\frac{d\sigma}{dy_p}$ and path from the pit bottom down into the material

Using the depth into the material y_p in mm, the mathematical function of equation (3.6) will be fitted on the strain range and maximum stress data points along the path. This is also done for a path that goes from the pit bottom into the specimen. In this equation a, b, c, e, and f are the parameters which will be determined by the fitting process. An example of a fit of the function is given in figure 3.18.

$$\{\Delta\epsilon/2, \sigma_{\text{max}}\} = \frac{a y_{\text{p}}^2 + b y_{\text{p}} + c}{y_{\text{p}}^2 + e y_{\text{p}} + f} \tag{3.6}$$

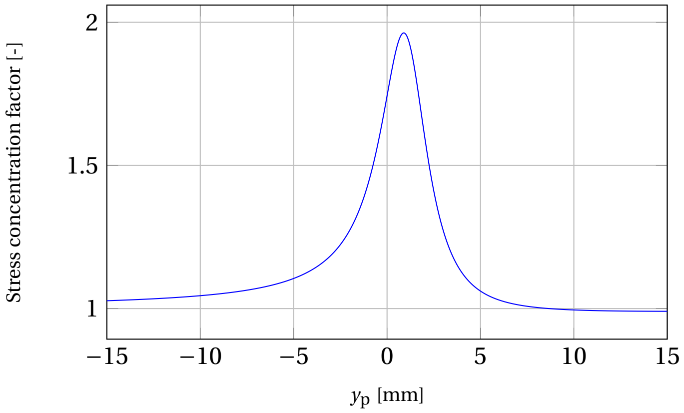

Figure 3.18: Plot of an exemplary fit of equation (3.6) for a pit depth of 2 mm

Using the finding that the specimen thickness does not influence the stress/strain over the pit surface, it has been found that the stress and strain along a path from the surface of a perfectly elliptical pit into the specimen is linearly scalable with the pit depth for a constant aspect ratio. This way only a maximum of three pit depths per aspect ratio have to be calculated using finite element modelling, which saves up computation time. Now, the stress and strain range are dependent on the pit depth and the location in the material. Using a pit growth model in combination with the load frequency, the dependence on pit depth can be substituted by a dependence on the number of load cycles. A function has been written that requires stress and strain as a function of y_p and N, and a value for y_p as input, and outputs the total damage at the given pit surface location; either pit bottom or maximum strain range location. This function creates two arrays in which respectively the maximum stress and strain range for a pit depth of 0 to y_p are stored. These arrays are used to create a new array in which the damage is saved for these values of strain range and maximum stress using the strain-life relation. By numerical integration of this array over the number of cycles N, the total damage is determined. This function is solved for a damage of 1, with a maximum error of 0.1%, using the Brentq-solver, which is implemented in Python. This way the number of cycles N and final pit depth at the moment of fatigue crack initiation can be determined.

3.4. Discussion

This section discusses the developed corrosion fatigue model and its input parameters. The developed model covers many corrosion and fatigue parameters, which results in a comprehensive basis to model the corrosion fatigue process. The current combination of input parameters as implemented in the developed model has not been found in any research work aimed at the prediction of the pit-to-crack transition yet. Still, a number of assumptions have been made in the development of the model in this study.

In this study, corrosion pit growth has been implemented using the maximum pit depth model of Wang [26]. This model regards the maximum pit depth based on relatively global environmental parameters (temperature, salinity, dissolved oxygen), but does not regard the local solution chemistry in the environment of the corrosion pit. The local chemistry affects the shape of the pit. Also, the effect of stress on the pit growth is not taken into account by the pit growth model. In this study, the shape of the pit has been simplified and taken as an ellipse in the XY-, and YZ-plane, and as a circle in the XZ-plane. Other variations in corrosion pit shapes as shown in figure 2.2 have not been investigated in this study, because no analytical pit growth models have been obtained from literature that predict the corrosion pit shape evolution. The effect of surface roughness has been implemented in the model locally by means of a micro-pit. The pit is assumed to grow while remaining its shape, also with a micro-pit implemented as surface roughness. It can be argued that the shape of a corrosion pit changes constantly due to the local chemistry, and is typically not elliptical. Nevertheless, it could be that the stress and strain levels around a corrosion pit can be estimated using a elliptical geometry including a certain surface roughness.

An accessory effect of the corrosion process is hydrogen absorption. The absorption of hydrogen in the material results in a more brittle material behaviour. The degree and extent of the effect of hydrogen absorption on material embrittlement, local stress-strain relations, and strain-life relations is relatively unknown, and limitedly implemented in this study. The effect of hydrogen absorption on the strain-life relation has been taken into account using the results of the research of Bignonnet et al. [76]. However, that research has not been well documented, and the number of experiments which the strain-life relations have been based upon is limited. Also, in the experiments of Bignonnet et al., the rate of hydrogen absorption is unknown, and there has been a certain surface roughness present due to the corrosive environment. Surface roughness has a significant effect on the fatigue crack initiation, but only acts at the surface of a material, where in the developed corrosion fatigue model, the strain-life relation has been used to accumulate damage below the surface as well. It is unknown up to which depth hydrogen absorption has an effect, though, the material in an offshore structure may be fully saturated with hydrogen relatively early during its life.

The coupling of the corrosion process to the fatigue process in this model has been done using the load frequency. The load frequency couples time to the number of cycles. The frequency has been assumed to be constant for all applied stress ranges, where in reality this will not be true. High stress ranges are likely to occur less frequent than low stress ranges in the load spectrum of wind turbine foundations at sea. The influence of the frequency on the corrosion fatigue model will be investigated further in chapter 6. In chapter 6, also the sensitivity of the developed model on the plastic hardening parameters, stress ratio, pit growth parameters, and strain-life parameters will be discussed.

A generally accepted definition of the moment of fatigue crack initiation does not exist in the fatigue research community. In this study, the criterion of a crack size of 0.074 mm has been implemented based on the research work of Dowling [59, 102]. The implementation of this research has been based on the fraction of fatigue initiation life over the fatigue life until failure of strain-life experiments. Especially in the high cycle fatigue region, the fraction includes a large uncertainty, because Dowling performed low cycle fatigue tests only. In the high cycle fatigue region ($N \geq 10^7$), a constant fraction of initiation life over total fatigue life until failure of 70% has been assumed. From the available test data in the low cycle fatigue region, a significant spread in the data has been found. Therefore, further research on strain-life relation for fatigue crack initiation is necessary, preferably by including free corrosion conditions.

Stress and strain levels are the input for the strain-life equation, and will be obtained from FEM calculations in chapters 4 and 5. In these chapters, linear (elastic) FEM calculations will be performed using the transient method in Abaqus, where non-linear (elasto-plastic) FEM calculations will be performed using the direct cyclic method in Abaqus. The direct cyclic method is aimed to find the stress or strain range from a cyclic loaded specimen more efficiently than using the transient method. It has been found that using the direct cyclic method, the stress/strain range is obtained correctly, where the maximum stress in a cycle is not obtained correctly for all cases. For a stress ratio of 0.5, the difference in fatigue life between both methods has been found to be below 2.5%, which has been assumed to be negligible. For lower stress ratios, a larger difference is expected, due to plasticity at the unloading part of the hysteresis loop.

It has been found that resulting hysteresis loops of FEM models with, and without implemented pit growth steps, show a good correspondence for stress ratios of at least 0.1. Therefore, pit growth steps have not been implemented in the FEM model. It has been found that the history of (plastic) strains has a negligible effect on the stress and strain levels at the pit surface. For lower stress ratios, a larger difference has been found, which could be due to plasticity at the unloading part of the hysteresis loop.

4

Pit-to-crack transition results

Chapter 4 describes results of the corrosion fatigue model as described in chapter 3. Two different cases, as listed in table 4.1, will be investigated in this section. A third case, of elliptical or circular shaped pits including a certain surface roughness will be discussed in chapter 5.

In chapter 4, the pit-to-crack transition of perfectly elliptical and circular shaped pits will be determined. These calculations are divided into two parts based on the loading which requires a different method of fitting the stress/strain paths: section 4.1, which shows pit-to-crack transition results of applied cyclic stresses that result in elastic strains only around the pit surface (linear calculations), and section 4.2, which shows pit-to-crack transition results of applied cyclic stresses that result in elastic and plastic strains around the pit surface (non-linear calculations). All calculations are performed using the 3D FEM model. Section 4.3 discusses all results, and conclusions will be drawn based on the results in this section.

	Section 4.1	Section 4.2	Section 5.1
Material behaviour	Linear	Non-linear	Linear & non-linear
Pit aspect ratio AR_p	0.25, 0.5 & 1.0	0.25, 0.5 & 1.0	0.50
Pit shape	Perfectly elliptical	Perfectly elliptical	Elliptical including micro-pit at pit bottom

Table 4.1: Cases investigated in this study

4.1. Fictive linear case

Section 4.1 describes the results of the corrosion fatigue model for ideally elliptical shaped pits for loads which result in elastic strains only. Linear FEM calculations in 3D are performed for three different aspect ratios; AR_p = 0.25, 0.5, and 1.0. All linear FEM calculations are performed for an applied static load of 1 MPa. Using the elastic behaviour of the material, the stress and strain ranges resulting from applied cyclic loads which result in elastic strains only at the pit surface can be determined from the static FEM calculations by means of superposition. Using the SCFs as determined in section 3.2.6, the maximum load that results in stress below the yield stress is determined for each aspect ratio.

Stress and strain results

First, the distribution of stress over the surface of the corrosion pits is determined, so the maximum stress can be located, which is equal to the maximum strain range location for linear calculations. Figure 4.1 shows the distribution of the maximum principal stress, and the Von Mises stress over the surface of a pit in the yz-plane of different depths for a constant width. The lines show a cross-section of the pit perpendicular to the direction of the applied stress, the colour of the lines show the distribution of the stress over the pit surface. The stress is normalized per aspect ratio to be able to show different aspect ratios in one figure. The black dots show the location of the maximum stress per aspect ratio.

The maximum principal stress (figure 4.1a) is located in the pit wall for aspect ratios of 0.5 and higher. For lower aspect ratios, the maximum stress is located in the pit bottom. The difference in maximum and

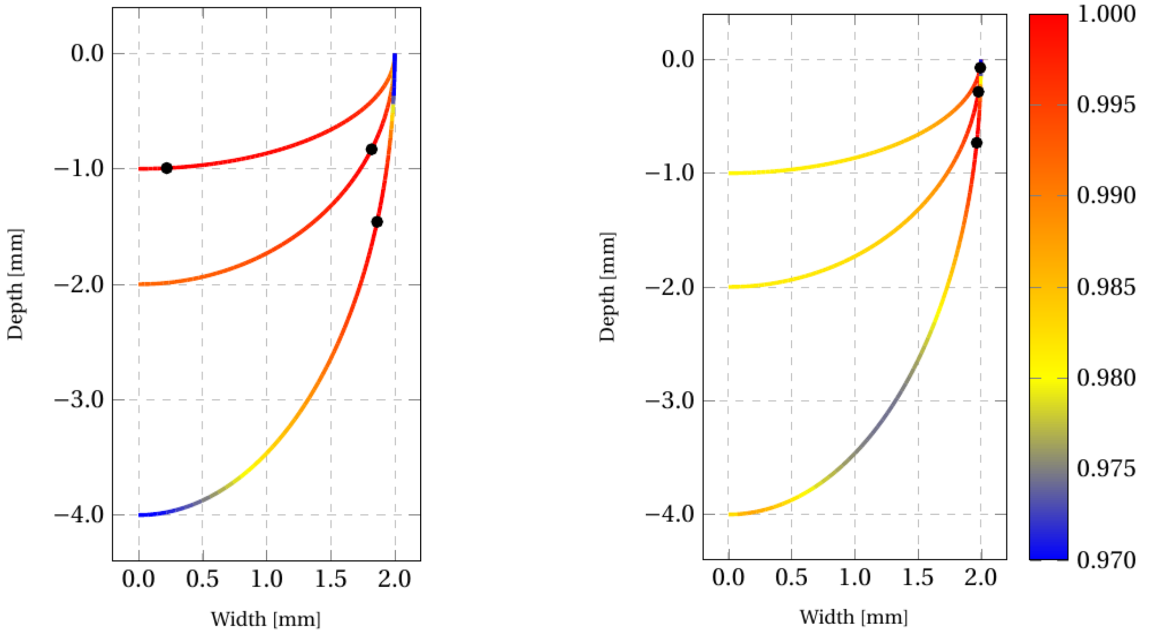

(a) Maximal principal stress

(b) Von Mises stress

Figure 4.1: Stress distribution over the surface of different pit shapes in the YZ-plane. The colour bar shows the stress, normalized per aspect ratio. The black dots show the location of maximum stress per pit depth.

minimum principal stress along the pit surface is lower for lower aspect ratios, although for an aspect ratio of 1.0, the difference is within 3%, which is not significant.

The maximum Von Mises stress (figure 4.1b) is located in the pit wall for all aspect ratios. Also, the maximum Von Mises stress locations are positioned higher in the pit wall than the maximum principal stress locations. This is due to a stress in the z-direction (equal to the width-axis in figure 4.1) in the pit bottom of about a tenth of the SCF, which has a negative impact on the Von Mises stress. At the maximum Von Mises stress locations, the stress in z-direction is negligible. The difference between the maximum and minimum Von Mises stress is higher than the difference in maximum principal stress for lower aspect ratios, but not significantly. Because the Von Mises stress is a yield criterion, this implies that plasticity will occur rather at the pit wall, than at the pit bottom.

In this study, not only the stress and strain distribution at the pit surface is taken into consideration, but also the stress and strain distribution below the pit surface. This way, damage can already be built up at a location in the material before this location becomes the pit surface due to pit growth. Figure 4.2 shows the stress concentration around and below corrosion pits for three aspect ratios. All pits are of equal depth and are displayed at the same scale to make comparison easier. It can be seen that for lower aspect ratios, the stress gradient is lower, i.e. the stress decreases less per unit of distance from the pit surface. Also, a difference in stress gradient over the pit surface can be observed. For an aspect ratio of 0.5, the stress gradient is equal over the whole pit surface. For higher aspect ratios, the stress gradient is higher at the pit bottom compared to the pit wall. For lower aspect ratios, this observation is the opposite. Note that the pit growth is modelled in such a way that the aspect ratio remains equal. This means that the pit growth rate at the pit wall in the direction of the stress/strain path can be different than at the path from the pit bottom down into the material. For sharp pits, where $AR_\text{p} > 0.5$, and the stress gradient is lower at the pit wall, just as the pit growth rate, this will increase the amount of damage along the stress/strain path. For more flat pits, where $AR_\text{p} < 0.5$, the stress gradient is also lowest where the pit growth rate is lowest, which will result in more damage accumulation at this location compared to the pit wall.

For each aspect ratio, four different pit sizes have been modelled. Table 4.2 shows the pit dimensions of all linear FEM calculations. From each model, two stress paths are extracted. One from the pit bottom down into the material along the y-axis, and one from the maximum strain location into the material. Figure 3.16 shows the coordinate system and the direction of an exemplary stress path from the pit wall into the material.

Figure 4.3 shows the data points and fit of the maximum principal stress along a path from the pit bottom down into the material. Figure 4.4 shows the data points and fit of the maximum principal stress along a path

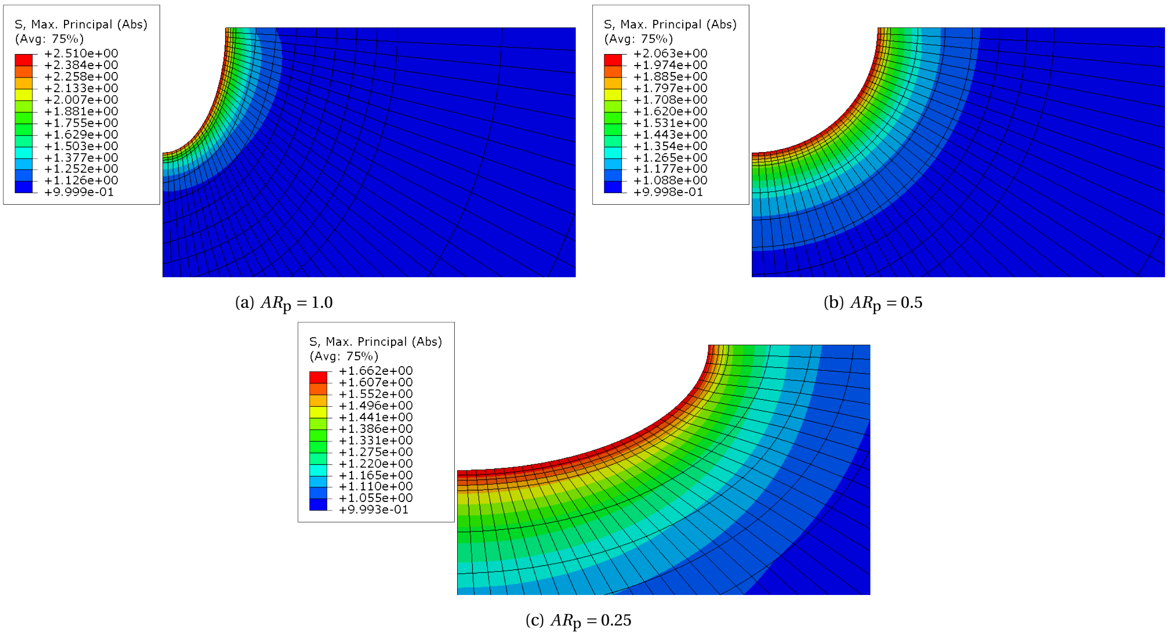

(a) $AR_\mathrm{p} = 1.0$

(b) $AR_\mathrm{p} = 0.5$

(c) $AR_\mathrm{p} = 0.25$

Figure 4.2: Stress distribution around and below the pit surface in the YZ-plane for different aspect ratios, a depth of 2.0 mm, and a stress of 1 MPa. The cross-section is taken perpendicular to the loading direction.

AR_p [-]	0.25				0.5				1.0			
a [mm]	0.25	1.0	2.0	4.0	0.5	2.0	4.0	8.0	1.0	2.0	4.0	8.0
$2c$ [mm]	1.0	4.0	8.0	16.0	1.0	4.0	8.0	16.0	1.0	2.0	4.0	8.0

Table 4.2: Pit dimensions of linear FEM models

from the maximum strain range location along the pit surface into the material. The maximum strain range location is different for each aspect ratio, accordingly figure 4.1a.

It has been found that the maximum stress along the pit surface was equal for each pit depth per aspect ratio. This means that the thickness of the material has no influence on the stress distribution along the surface of a pit. This finding made it possible to linearly extrapolate the stress along a path over different pit depths. Therefore, the mathematical function of equation (3.6) has been fitted only to the data points of the results of one FEM model per aspect ratio, which is indicated in figure 4.3 by a dashed line. From the figures it can be seen that the stress gradient is lower for higher aspect ratios, just as the SCF, which is equal to the results of figure 4.2.

Corrosion fatigue initiation life results

Maximum stress and strain range functions for a stress ratio of 0.5 are calculated based on the fitted functions for stress along the paths into the material using superposition. The final pit depth and number of cycles to the pit-to-crack transition are determined using the method described in section 3.3. The results for the chosen stress ranges are shown in appendix C, table C.1. Figure 4.5 shows the results in a stress life plot together with the elastic part of the strain-initiation life curve in free corrosion conditions, compensated for a stress ratio of 0.5 using the Smith-Watson-Topper mean stress correction, and the mean and design SN-curves for base material in free corrosion and air conditions from DNV GL standard RP-C203 [66]. A note must be added that the SN-curves include crack propagation life, where the strain-life curve, and therefore the resulting data points as well, do not include this.

When the results for the maximum strain range locations are compared to the results at the pit bottom, a large difference is found for an aspect ratio of 1.0. The maximum stress is higher, and the stress gradient is lower at the maximum strain range location for this aspect ratio, which both is positive for fatigue crack initiation in terms of corrosion fatigue. For circular shaped pits, i.e. pits with an aspect ratio of 0.5, the difference between the moment of the pit-to-crack transition at both locations is relatively low. For higher aspect ratios,

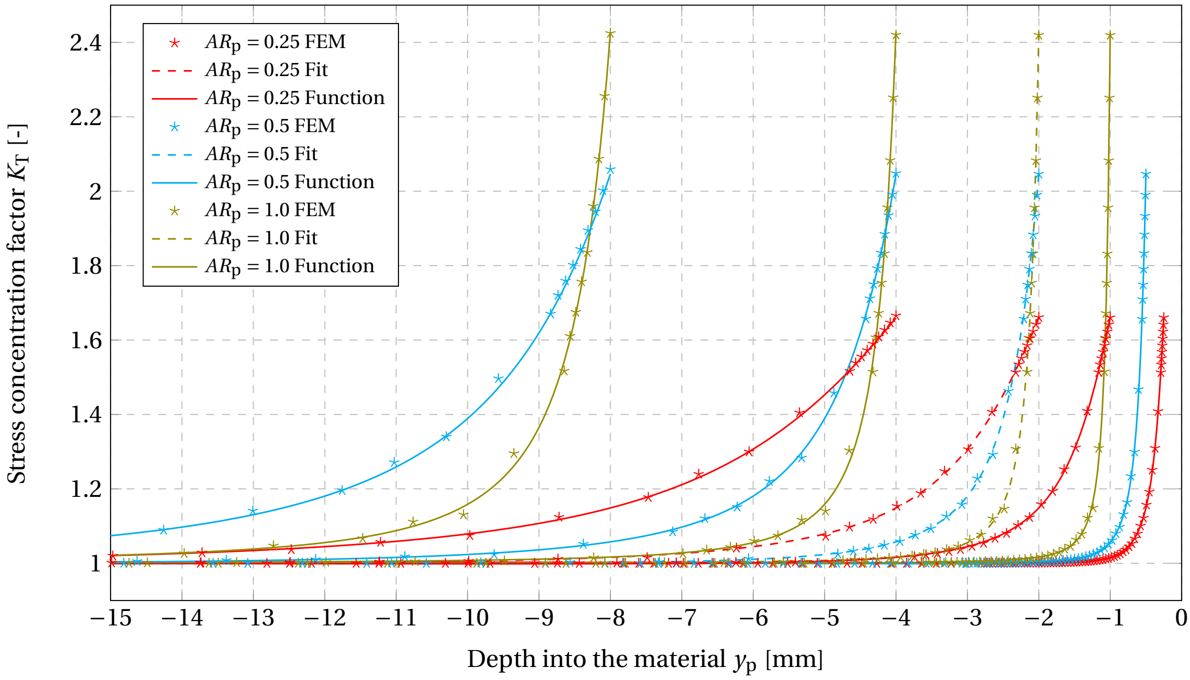

Figure 4.3: Stress concentration factor along a path from the pit bottom into the material

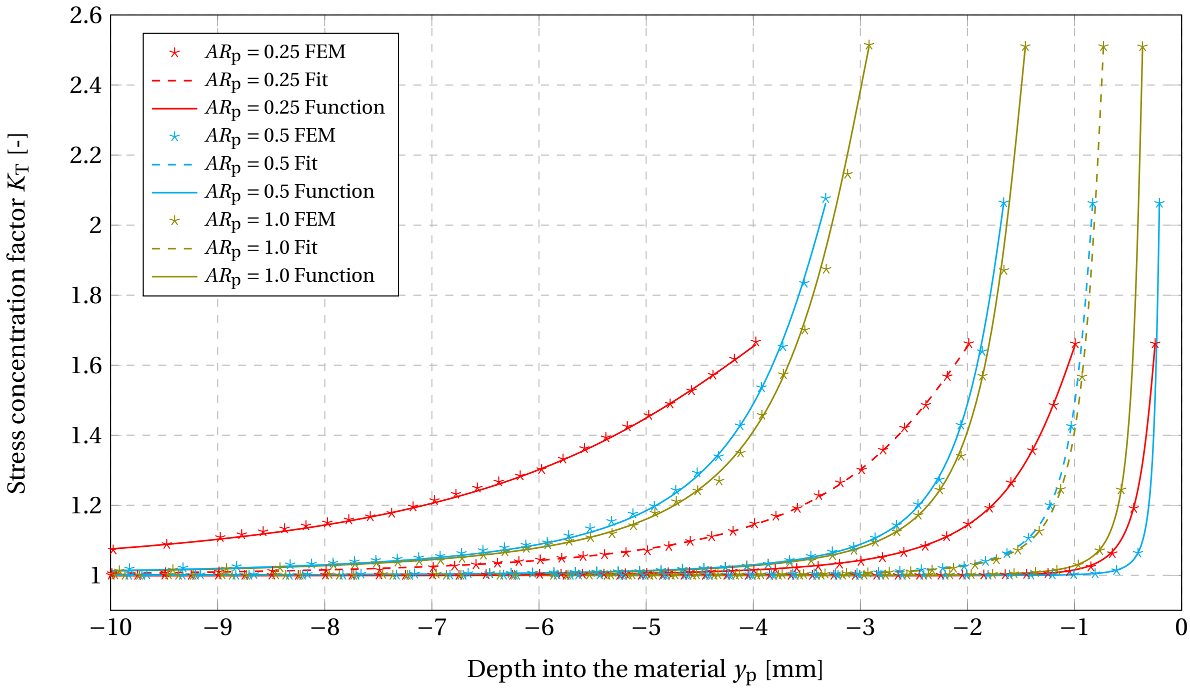

Figure 4.4: Stress concentration factor for location of maximum stress in thickness

the difference is negligible, because the maximum strain range is located almost at the pit bottom.

From figure 4.5 it can be found that the data points of the fatigue crack initiation life of perfectly elliptical and circular corrosion pits are all positioned above the DVNGL standard for fatigue in sea water.

A comparison between the accumulated damage for different locations in the pit, and aspect ratios, can be found in figure 4.6. This figure shows a gradual increase in accumulated damage for low aspect ratios compared to higher aspect ratios, which corresponds to a lower stress gradient, and lower SCF for low aspect ratios. For higher aspect ratios, the SCF and stress gradient are higher, which corresponds to a steeper

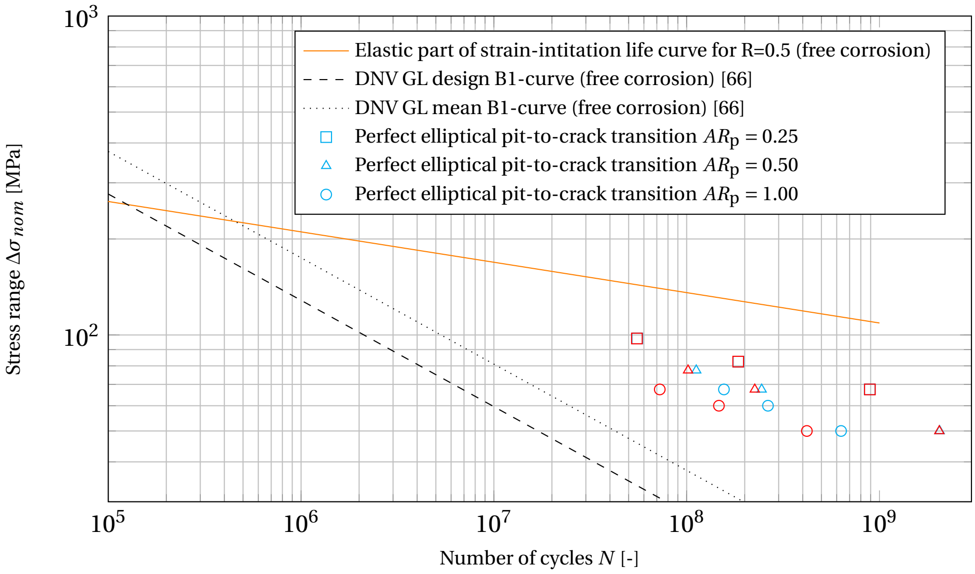

Figure 4.5: Corrosion fatigue initiation life results including the S-N curve for free corrosion of DNV GL standard. Blue marks indicate results at the pit bottom location and red marks indicate the results at the maximum strain range location on the pit surface.

accumulated damage curve. For $AR_p = 0.25$, the accumulated damage increases linearly from a certain moment in time. This is due to the choice of the pit growth model of Wang, which states that the pit growth rate decreases over time. For this aspect ratio, the difference between the accumulated damage curve at the maximum strain range location and the pit bottom is negligible. This is due to the maximum stress location being positioned close to the pit bottom for this aspect ratio. For $AR_p = 0.5$ and $AR_p = 1.0$, the location of the pit-to-crack transition is more clearly at the maximum strain range location. At these locations, the accumulated damage curve starts to get steeper at a lower number of cycles. This is because the stress gradient is lower at these locations than at the pit bottom. The difference is significant at an aspect ratio of $AR_p = 1.0$. For this aspect ratio, the damage per cycle is given in figure 4.7.

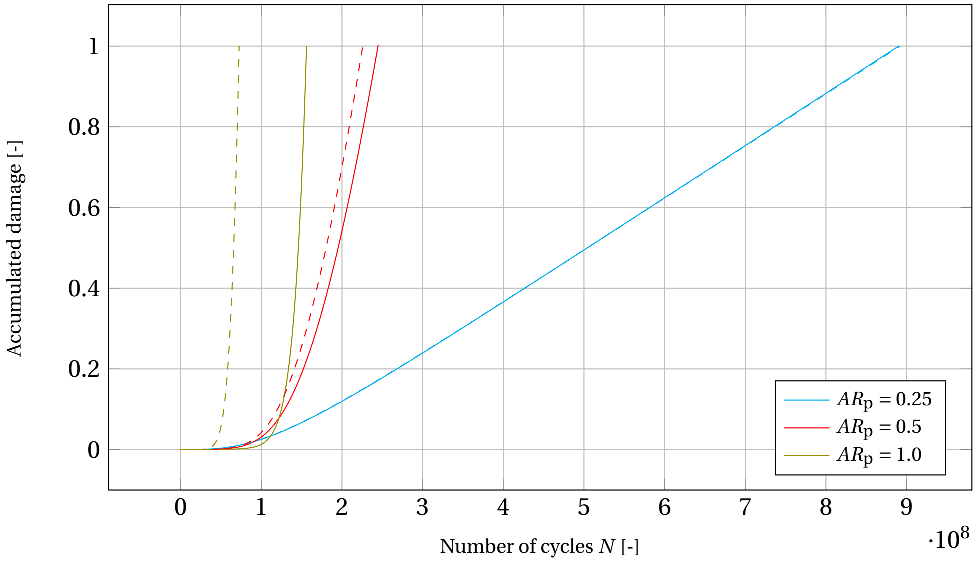

Figure 4.6: Accumulated damage for $\Delta\sigma = 135$ MPa. The dashed lines indicate the accumulated damage at the maximum strain range location in the pit surface, the solid lines the accumulated damage at the pit bottom.

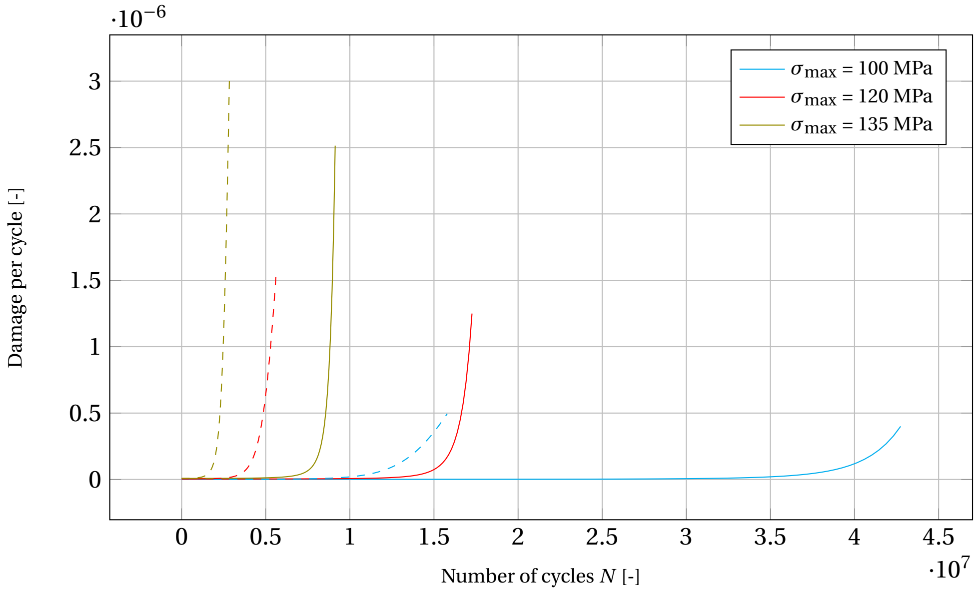

Figure 4.7: Damage per cycle for an aspect ratio AR_p of 1.0 and a stress ratio R of 0.5. The dashed lines indicate the accumulated damage at the maximum strain range location in the pit surface, the solid lines the accumulated damage at the pit bottom.

4.2. Fictive non-linear case

Section 4.2 describes the results of the corrosion fatigue model for ideally elliptical shaped pits for loads which result in elastic and plastic strains at the pit surface. The calculations are performed for the same three aspect ratios as in section 4.1. A cyclic load is applied in the FEM model, using the direct cyclic method in Abaqus, and by applying the mean stress prior to the cyclic load. All stresses are chosen as such, that the mean stress does not result in plasticity around the pit surface. This way, the direct cyclic method can be used to determine the strain ranges and maximum stress around and below the pit surface, as shown in section 3.2.4. The chosen pit dimensions and stress ranges of the non-linear FEM models are listed in table 4.3. A total of 27 non-linear FEM models are created.

AR_p [-]	a [mm]	$2c$ [mm]	$\Delta\sigma_{nom}$ [MPa]	$\sigma_{nom,max}$ [MPa]
0.25	0.25 1.0 4.0	1.0 4.0 16.0	125, 137.5, 150	250, 275, 300
0.5	0.25 1.0 4.0	0.5 2.0 8.0	100, 110, 120	200, 220, 240
1.0	0.5 2.0 4.0	0.5 2.0 4.0	80, 90, 100	160, 180, 200

Table 4.3: Pit dimensions and load specification of non-linear FEM models

Stress and strain results

Figure 4.8 shows the distribution of the maximum principal strain range and maximum principal stress at the pit surface for the different aspect ratios.

When this distribution is compared to the distribution of stress at the pit surface from the linear FEM models (see figure 4.1), it stands out that the maximum strain range in the plastic regime is located higher than the maximum strain range in the elastic regime. This can be explained by the maximum plastic strain being located at the pit wall, which was expected, because the Von Mises stress is maximum at this location too in the elastic regime. The difference in maximum principal strain range over the whole pit surface is higher for lower aspect ratios, but not significant. The maximum difference for $AR_p = 1.0$ is about 2.5%.

The maximum principal stress is located closer to the pit bottom than the maximum principal strain range. It can be seen that the maximum principal stress does not change much along the pit surface, except at the mouth of the corrosion pit, where the maximum plastic strain is located. This corresponds to the findings of Turnbull [95], who found that the principal stress region localised towards the pit bottom in case plasticity occurs. The maximum strain range location and the maximum principal stress location are not equal, where these locations were equal for the linear calculations. Because the fatigue crack initiation life is dependent on both variables due to the mean stress correction on the strain-life equation, the minimum fatigue crack initiation life without taking pit growth into account is located in between these locations, as can be seen in figure 4.9. Next to the stress and strain at the pit surface, also the gradient of principal stress and the principal strain range, and the pit growth rate, which is different at different locations along the pit surface, have influence on the fatigue crack initiation life of a growing corrosion pit. Therefore, it can not be predicted which of the locations will have the lowest fatigue crack initiation life. The maximum principal strain range, maximum principal stress, and minimum fatigue crack initiation life locations will all be taken into account in the fatigue crack initiation life calculations in this section. It has been found that the maximum stress, and minimum life locations are different for different stress ranges per aspect ratio. The maximum strain range location is equal for all stress ranges per aspect ratio. All locations are listed in table C.2 in appendix C.2.

Figure 4.10 shows the distribution in thickness of the total principal strain at the peak of the applied cyclic load for the three aspect ratios. The applied mean stress is for each aspect ratio just below the yield strength in the pit surface. Just as for the linear FEM analyses, the gradient is relatively constant along the pit surface for a circular shaped pit, where for sharper pits, the gradient is lower at the pit wall than at the pit bottom, and for lower aspect ratios, the gradient is lower at the pit bottom than at the pit wall.

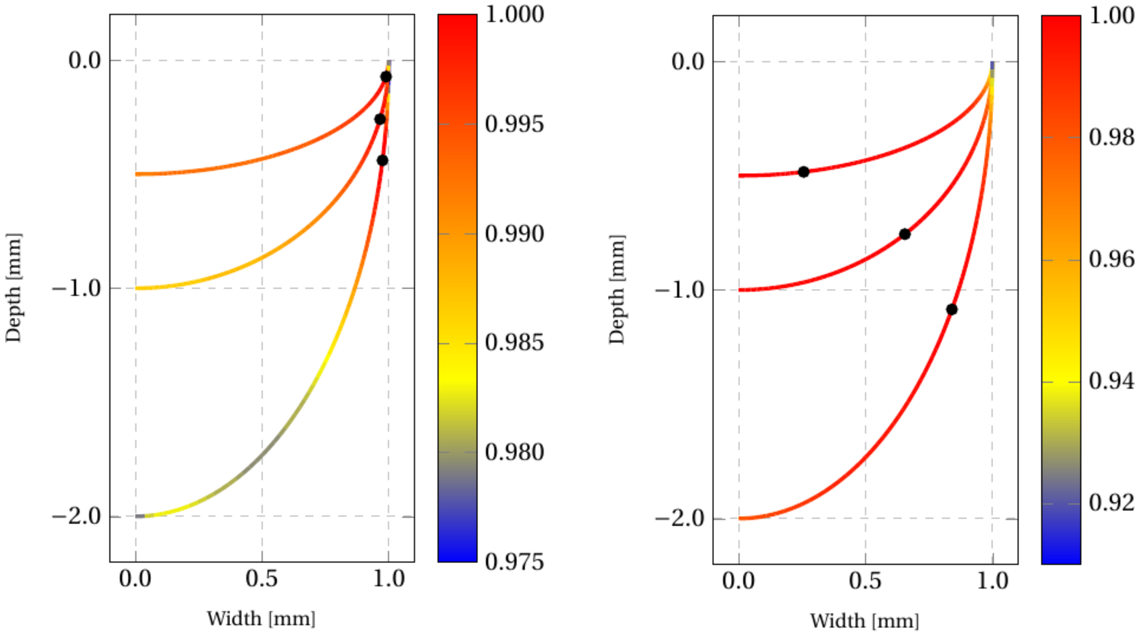

(a) Maximum principal strain range (normalized)

(b) Maximum principal stress (normalized)

Figure 4.8: Strain range and stress distribution over the surface of different pit shapes in te YZ-plane. The colour bar shows the {strain range, stress}, normalized per aspect ratio. The black dots show the location of maximum {strain range, stress} per pit size.

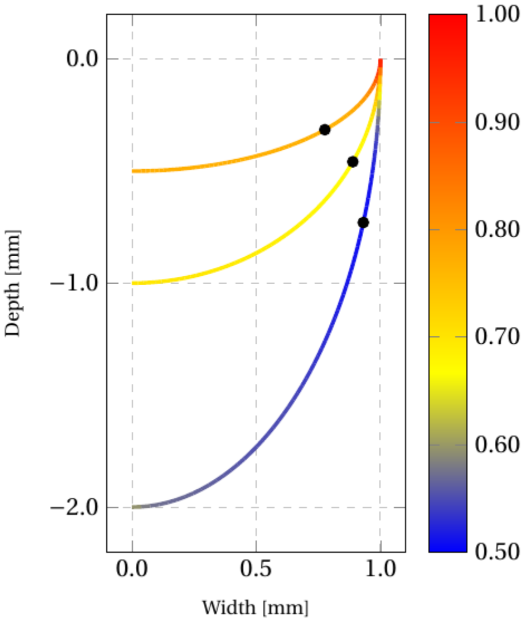

Figure 4.9: Fatigue crack initiation life distribution over the surface of different pit shapes in te YZ-plane corresponding to the maximum stress and strain range from figure 4.8. The values correspond to a stable corrosion pit, so no pit growth is taken into account. The colour bar shows the initiation life, normalized per aspect ratio. The black dots show the location of minimum fatigue life respectively per pit size.

The maximum principal stress and maximum principal strain ranges along paths from the pit bottom down into the material, or from the maximum strain range location into the material, are shown in appendix C.2, figures C.1 to C.12. The stress and strain paths are only shown for the pit bottom and maximum strain range location, because of the amount of graphs required when all locations were taken into account.

The mathematical function of equation (3.6) is fitted for the middle pit size for each aspect ratio, applied stress range, and location. The other lines in the figures are extrapolated using a linear dependence and show good similarity to the data points. It has been found that maximum stress has its highest value at a location

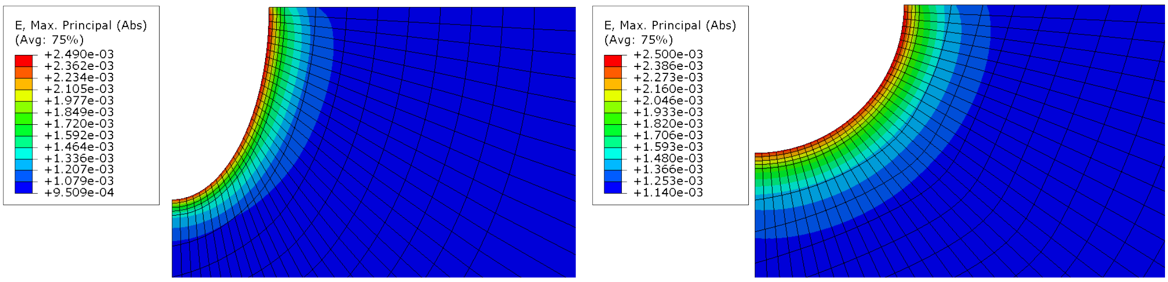

(a) $AR_{\text{p}} = 1.0$ - $\sigma_{nom,max} = 200$ MPa (b) $AR_{\text{p}} = 0.50$ - $\sigma_{nom,max} = 240$ MPa

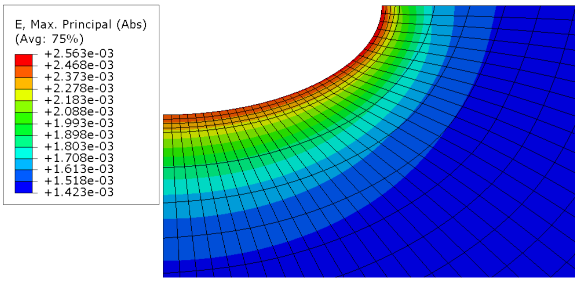

(c) $AR_{\text{p}} = 0.25$ - $\sigma_{nom,max} = 300$ MPa

Figure 4.10: Strain distribution around and below the pit surface in the YZ-plane at the peak of the sinusoidal cyclic load. The cross-section is taken perpendicular to the loading direction.

just below the pit surface for some stress ranges. This is only the case when plasticity is located at the pit surface at that location.

Corrosion fatigue initiation life results

The fatigue crack initiation life results are listed in table C.3 in appendix C.2 for all investigated locations. From the results is has been found that the pit bottom is the most favourable location for fatigue crack initiation for an aspect ratio of $AR_{\text{p}} = 0.25$, the minimum life location is the most favourable location for an aspect ratio of $AR_{\text{p}} = 0.50$, and the maximum strain range location is the most favourable location for an aspect ratio of $AR_{\text{p}} = 1.00$. This means that the sharper the pit shape, the higher in the pit wall a crack will initiate. For circular shaped pits, the difference in fatigue crack initiation life along the pit surface is relatively low compared with more sharp or blunt corrosion pits.

Figure 4.11 shows the fatigue crack initiation life results of corrosion pits in free corrosion conditions for both the linear as the non-linear calculations. In this graph, only the fatigue crack initiation results at the pit bottom and maximum strain range location are shown for clarity and consistency. The slope of all fatigue crack initiation life results is estimated to be $m \approx 6$, where the slope for the DNV GL B1 SN-curves for free corrosion have a slope of $m = 3$.

4.3. Discussion and conclusions

This section discusses the results of chapter 4 and draws conclusions based on the results. Because the main objective of this study is to develop a model that predicts the moment of the pit-to-crack transition, and the location of the pit-to-crack transition in a corrosion pit, this section is split up in two parts. The first part discusses the fatigue crack initiation life, which is assumed to be equal to the moment of the pit-to-crack transition in this study. The second part discusses the location of the pit-to-crack transition in the corrosion pit.

Fatigue crack initiation life

Sections 4.1 and 4.2 have shown that the fatigue crack initiation life of perfectly elliptic corrosion pits found from the corrosion fatigue model is higher than the total fatigue life given by the SN-curves for the same stress ranges. The model has also shown that the slope of the fatigue crack initiation results is more flat ($m \approx 6$) compared to the SN-curve of DNV GL ($m = 3$). Because the fatigue crack initiation life is a larger fraction of the total fatigue life in the high cycle fatigue region compared to lower number of cycles, a relatively lower

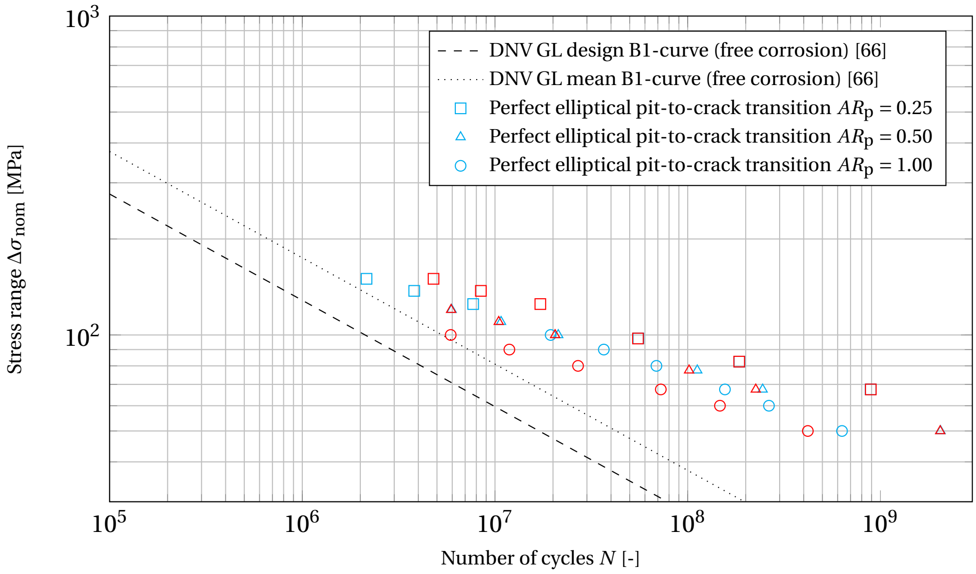

Figure 4.11: Corrosion fatigue initiation life results including the S-N curve for free corrosion of DNV GL standard. Blue marks indicate results at the pit bottom location and red marks indicate the results at the maximum strain range location on the pit surface.

amount of fatigue crack propagation life will be added to the data points in the high cycle fatigue region when propagation would be taken into account. Therefore, the difference in slope will be lower between the data points of the developed model and the DNV GL B1 SN-curve for free corrosion conditions. Because the input parameters are expected to have a significant effect on the fatigue crack initiation life results of the developed model, no conclusions can be drawn on the DVNGL SN-curve for free corrosion conditions. In chapter 6, a sensitivity study of the developed on the input parameters is presented. In this chapter, a more elaborate discussion on the comparison between the DNV GL SN-curves and the results of the developed model is presented.

From the three different aspect ratios investigated in this study, it has been found that the sharpest pit ($AR_p = 1.0$) has the lowest fatigue crack initiation life, and the most blunt pit ($AR_p = 0.25$) has the highest fatigue crack initiation life. This can be expected because a sharper pit (higher aspect ratio) results in a higher stress concentration factor. But, it has been found that a more blunt pit (lower aspect ratio) has a lower stress gradient, which in some cases results in a higher strain range from a certain depth compared to sharper corrosion pits (figure 4.3). This way the accumulated damage based on the strain history will be higher up to a certain depth into the material. The effect of the stress gradient is larger at high pit growth rates, which is at high stress ranges. From the results it has been seen that at low stress ranges, the spread between the results of different aspect ratios is larger, which is due to the difference in SCF and the low pit growth rate at the moment of fatigue crack initiation at these stress ranges.

Yet, it can be concluded that the influence of the SCF on the fatigue crack initiation life of perfectly elliptical corrosion pits is larger than the effect of the stress gradient, mainly at low stress ranges. From a mechanistic point of view, in the developed model, the competition between the corrosion process and the fatigue process can be seen as a competition between the pit growth rate, stress gradient and the SCF.

Fatigue crack initiation location

Per aspect ratio, the fatigue crack initiation life has been determined of two locations for linear calculations. The first was the pit bottom, the latter the maximum strain range location, which depends on the aspect ratio. For non-linear calculations, the maximum stress location has been found to be different from the maximum strain range location. Therefore, the maximum stress location and the minimum life location for a stable (non-growing) corrosion pit were also investigated for non-linear FEM calculations, next to the pit bottom and maximum strain range location.

Typically all maximum strain range locations have been found to be in the pit wall. Only for an aspect ratio of 0.25 and elastic strains at the pit surface, the maximum strain range location was found at the pit bottom. The maximum stress location has been found to be closer to the pit bottom due to the localisation of plastic strain at the pit wall. This finding corresponds to the findings of Turnbull et al. [95].

The difference between the strain range at the pit bottom and the pit wall has been found to be larger for higher aspect ratios. The stress gradient has been found to be larger at the pit wall than at the pit bottom for an aspect ratio of 0.25, where the inverse has been found at an aspect ratio of 1.0. For circular shaped corrosion pits ($AR_\mathrm{p} = 0.5$) the stress gradient has been found to be constant around the pit surface. The competition between the stress gradient and the SCF is the reason of difference in fatigue crack initiation location between different aspect ratios.

The fatigue crack initiation location is the pit wall for all cases of an aspect ratio of 1.0, where the maximum strain range and the lowest stress gradient is located in the pit wall. For a circular pit shape, the difference between the fatigue crack initiation life at the pit bottom and the pit wall has been found to be negligible. For an aspect ratio of 0.25, the pit bottom has been found to be the location of fatigue crack initiation, even though the maximum strain range is not located here in all cases. The pit bottom is a more favourable location for fatigue crack initiation of corrosion pits with an aspect ratio of 0.25, because of a lower stress gradient compared to the pit wall.

5

Effect of surface roughness on the pit-to-crack transition

Section 5.1 shows the results of the pit-to-crack transition of elliptical or circular shaped pits including a certain surface roughness. In this section both linear and non-linear calculations are performed. The results will be discussed in section 5.2.

5.1. Fictive case including surface roughness

In this section results are shown of elliptical corrosion pits including surface roughness. By including a more realistic corrosion pit shape, more realistic fatigue crack initiation life results can be obtained. To reduce calculation time, the roughness is only applied locally by means of a micro-pit. The micro-pit is located in the bottom of the corrosion pit. Even though it has been found in section 4.2 that fatigue crack initiation occurs earlier in the pit wall than in the pit bottom for certain aspect ratios, for simplicity reasons, only the effect of roughness on the initiation life at the pit bottom has been looked at in this section. It is expected that the results return a good estimation of the influence of surface roughness on the fatigue crack initiation life at locations other than the pit bottom as well. To reduce the computation time, it has been chosen to perform calculations including a micro-pit for a corrosion pit aspect ratio of 0.5 only. For the same reason, it has been chosen to investigate micro-pits of an aspect ratio of 0.5 only.

The micro-pit is chosen to be a percentage of the depth of the corrosion pit. This way the stress and strain path from the pit bottom down into the material can be extrapolated using the same linear relation as in sections 4.1 and 4.2. In these sections proof has been given that the linear extrapolation can be used for the range of pit depths necessary for the implemented pit growth model. Therefore, only one FEM calculation per micro-pit depth over pit depth ratio is performed. The calculations are performed for micro-pit depth over pit depth fractions (a_{micro}/a) of 0.01, 0.05, and 0.1.

Stress and strain results

Figure 5.1 shows the distribution of stress around, and below the micro-pit surface. All images are of the same scale, and same location. The colour scale, which indicates the maximum principal stress, is also equal for each image. From the figures, it can be seen that the stress concentration is higher for a smaller micro-pit depth. It can also be seen that a larger micro-pit depth has a larger effect on the stress distribution below the surface of the micro-pit, which means that the stress gradient is lower.

Figure 5.2 shows the stress path from the pit bottom down into the material from the static linear calculations. The stress path from the pit bottom down into the material for a perfectly elliptical pit without micro-pit has been shown in this figure as well by means of a solid black line. It can be seen from this figure that the SCF is larger for smaller micro-pits, just as the stress gradient. This means that a larger micro-pit will result in more damage accumulation at a location in the material before the pit surface reaches this depth. From the graph it can be seen as well that the implementation of a micro-pit can be seen as a superposition of stress. The fitted curves shown in the graph, are created based on a superposition of two fits. The first is the fit of a perfectly circular pit (black line in the graph), and the second is the fit of the extra stress induced by the micro-pit.

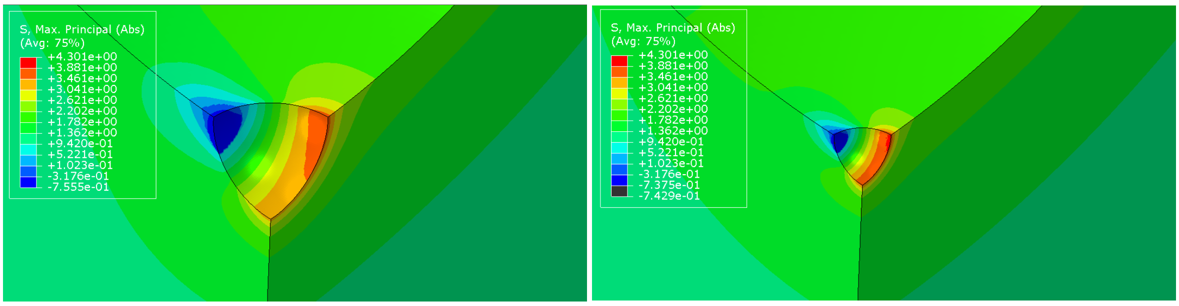

(a) $a_{\text{micro}}/a = 0.10$, $K_T = 3.820$ (b) $a_{\text{micro}}/a = 0.05$, $K_T = 3.972$

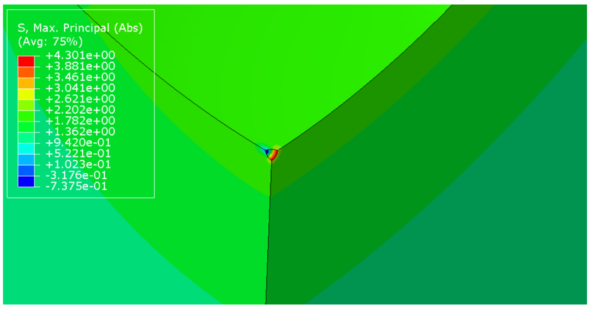

(c) $a_{\text{micro}}/a = 0.01$, $K_T = 4.301$

Figure 5.1: Stress distribution around and below the micro-pit surface located in the pit bottom of a corrosion pit with an aspect ratio of $AR_p = 0.5$ and a pit depth of $a = 0.5$ mm. The micro-pit has an aspect ratio of $AR_p = 0.5$ and its depth is a fraction of the pit depth of the corrosion pit.

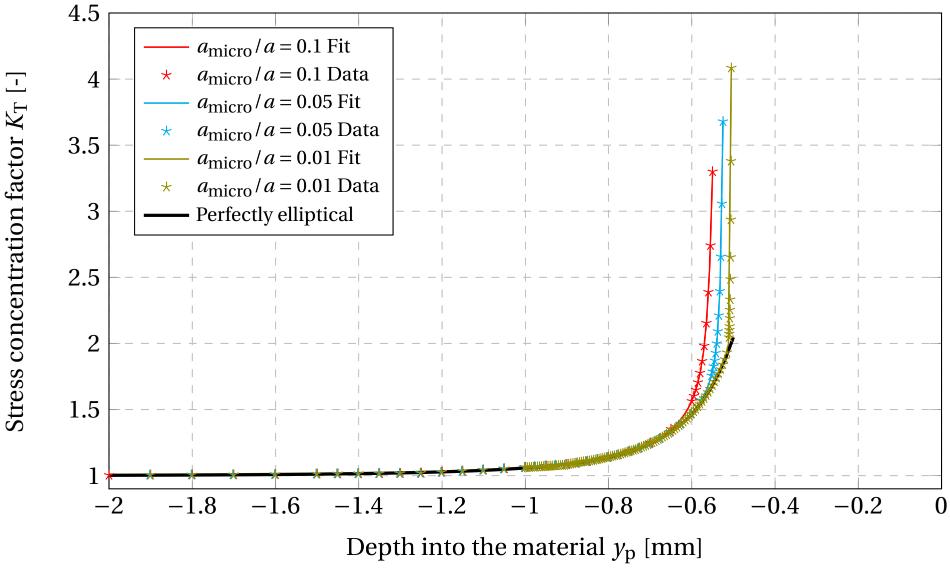

Figure 5.2: Stress concentration factor along a path from the pit bottom into the material for a pit of aspect ratio $AR_p = 0.5$ and a pit depth $a = 0.5$ mm including and excluding a micro-pit at the pit bottom

The same correlation is found in cyclic, non-linear calculations of equal geometries. Figures C.13 and C.14 in appendix C.3 show respectively the strain range and maximum stress path from the pit bottom down into the material of the cyclic, non-linear FEM calculations for a nominal stress range of 120 MPa. For other nominal stress ranges, no graphs are shown in the appendix, because of the large amount of required space.

Corrosion fatigue initiation life results

Figure 5.3 shows the fatigue crack initiation life results of the corrosion fatigue model including a micro-pit at the pit bottom. Also, results of calculations from sections 4.1 and 4.2 for the same geometry without a micro-pit are shown in the figure. It can be found that the correlation between the nominal stress range and the number of cycles to fatigue crack initiation for corrosion pits including a micro-pit tends to follow about the same slope of the results without a micro-pit for stress ranges above 60 MPa. For stress ranges below 60 MPa, the slope quickly becomes very steep. It has been found that this effect is caused by the pit growth rate, that is decreased significantly at about $1 \cdot 10^8$ cycles. This can be seen in figure 5.3, which also shows the maximum pit depth in time, which is plotted against the number of cycles using the frequency. Because the corrosion process is degrading the material more slowly, i.e. expanding the corrosion pit more slowly, more damage can be accumulated in the material below the corrosion pit surface. This way, the high stress concentration due to the micro-pit, that only appears close to the micro-pit surface due to the high stress gradient, impacts the fatigue crack initiation life more significantly at low stress ranges.

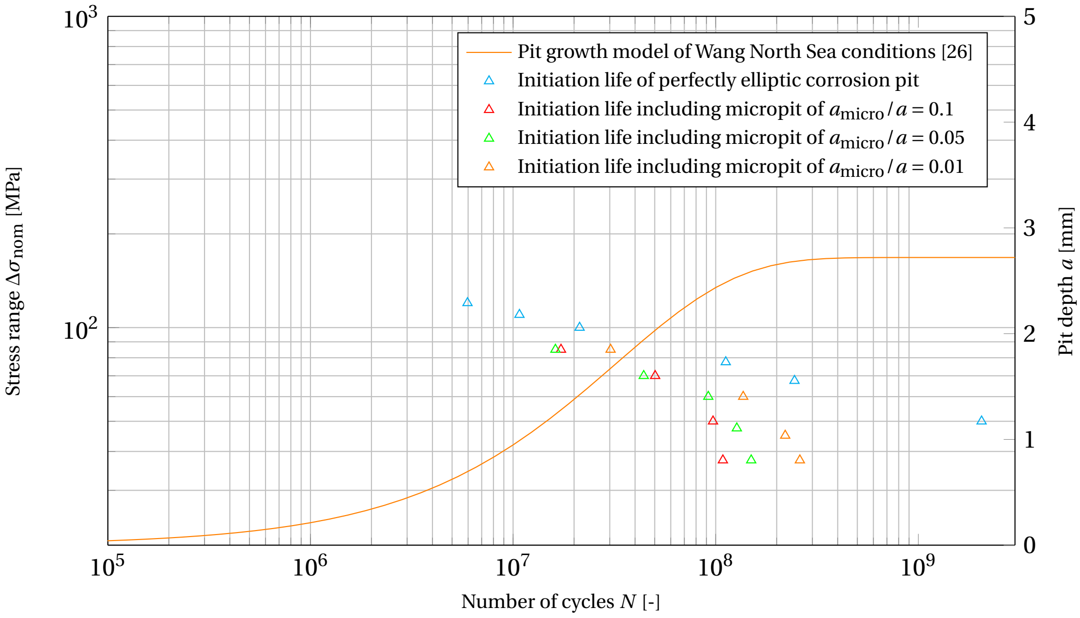

Figure 5.3: Fatigue crack initiation life results from the corrosion fatigue model including and excluding a micro-pit at the pit bottom. All results are for initiation at the pit bottom and for a pit aspect ratio of $AR_p = 0.5$. The secondary y-axis shows the pit depth.

5.2. Discussion and conclusions

This section discusses the results from section 5.1, and draws conclusions based on the results. Because the main objective of this study is to develop a model that predicts the moment of the pit-to-crack transition, and the location of the pit-to-crack transition in a corrosion pit, this section is split up in two parts. The first part discusses the fatigue crack initiation life time, which is assumed to be equal to the moment of the pit-to-crack transition in this study. The second part discusses the location of the pit-to-crack transition in the corrosion pit.

Fatigue crack initiation life

Compared to the pit geometries without a micro-pit, the SCF has been found to be doubled for the smallest micro-pit depth over corrosion pit depth ratio investigated ($a_{micro}/a = 0.01$), and one and a half times the original SCF for the largest ratio ($a_{micro}/a = 0.1$). The stress gradient has been found to be larger at shallower micro-pits with regard to the corrosion pit than deeper micro-pits, yet all micro-pits had a relatively large stress gradient. Due to the large stress gradients, the impact of the micro-pits is relatively low at higher stress ranges, where the pit growth rate is relatively high at the moment of fatigue crack initiation. At lower stress ranges, where the pit growth rate at the moment of fatigue crack initiation is relatively low, the impact on the fatigue crack initiation life is high. At the number of cycles where the pit growth rate decreases nearly to zero, an almost vertical asymptote has been found. This vertical asymptote is a result of the combined effect of the low pit growth rate, the high SCF, and the high stress gradient. Due to the low pit growth rate, damage is able to accumulate at the surface of the corrosion pit, where the SCF is significant higher than below the surface, due to the high stress gradient. Therefore more damage is able to accumulate per cycle, than when the pit growth rate was higher, which results in failure at the number of cycles, where the pit growth rate is decreased significantly, regardless of the stress range. This behaviour will not be found in reality, due to the load spectrum of wind turbine foundations, in which low stress ranges are more likely to occur more frequently than high stress ranges. This will result in a variable load frequency, where in the developed model a constant frequency is implemented. In section 6.5, the effect of the frequency on the fatigue crack initiation life will be investigated further.

Because of the dependency of the fatigue crack initiation life including surface roughness on the load frequency, no factor between the results including and excluding surface roughness could be established.

Fatigue crack initiation location

The influence of surface roughness on the fatigue crack initiation location has not been investigated directly in this study, but based on the results of a micro-pit at the pit bottom, a prediction can still be made.

It is expected that surface roughness has an equal effect on the stress and strain levels at both the pit bottom as the pit wall, dependent on the degree of surface roughness. As found in section 5.1, the stress gradient due to the surface roughness is such significant, that at high stress ranges, where the pit growth rate is high at the moment of fatigue crack initiation, the effect on the fatigue crack initiation life is low. When comparing fatigue crack initiation at the pit bottom and pit wall for different aspect ratios, it is important to note that in this study, the pit depth is taken as a measure to determine the pit growth rate. This means that the rate of material degradation is higher at the pit wall for blunt corrosion pits, and lower at the pit wall for sharp corrosion pits compared to the pit bottom. Therefore, for sharp pits, surface roughness will have more effect at the pit wall, and for blunt pits, surface roughness will have more effect at the pit bottom. Because these locations are the fatigue crack initiation locations without surface roughness, the location of fatigue crack initiation will not be different with surface roughness. For circular shaped pits, the difference in fatigue crack initiation at the pit wall and pit bottom is small. This is expected not to change when surface roughness is taken into account.

6

Sensitivity study

This chapter elaborates on the sensitivity of the corrosion fatigue model to the input parameters. The sensitivity will be tested for one geometry only: a circular shaped pit without surface roughness. The aspect ratio therefore is 0.5, which is the middle value of the aspect ratios used in chapter 4. Because the difference in the fatigue crack initiation life between the pit bottom and the maximum strain range location, which is at the pit wall for a circular shaped pit, for this aspect ratio is low, only the results of the corrosion fatigue crack initiation life at the pit bottom are shown in this chapter.

All input parameters are listed in figure 3.1 and discussed in section 3.1. Section 6.1 discusses the sensitivity of the corrosion fatigue model to pit growth parameters, section 6.2 discusses the sensitivity to the Chaboche hardening parameters, section 6.3 discusses the sensitivity to the strain-life parameters, section 6.4 discusses the sensitivity to the stress ratio, and the sensitivity of the corrosion fatigue model to the frequency is shown in section 6.5. It has been found that, for a pit depth of 20% of the specimen thickness, the influence of the specimen thickness on the stress and strain at the pit surface and below is negligible, e.g. the linear extrapolation of the stress and strain paths are still valid. Therefore the specimen thickness is not taken into account in this sensitivity study.

6.1. Pit depth parameters

In the corrosion fatigue model, the maximum pit depth model of Wang et al. [26] is implemented. This model consists of three parameters, i.e., d_m, α, and m, as shown in equation (6.1), where a is the maximum pit depth in mm after a certain amount of time t in years.

$$a(t) = d_\mathrm{m}\left(1 - \exp\left(-(\alpha \cdot t)^m\right)\right) \tag{6.1}$$

According to Wang's maximum pit depth model, d_m determines the maximum pit depth after an infinite amount of time, and is determined mainly by the temperature of the sea water. α determines the speed at which the maximum pit depth d_m will be reached, and is determined mainly by the dissolved oxygen in the sea water, and temperature of the sea water. m determines the corrosion pit growth rate at the start of the pit growth process. Wang et al. found no clear correlation between m and any environmental or materialistic parameter.

Parameter d_m

Originally, the value for the maximum pit depth parameter d_m was set to 2.72 mm, which corresponds to 11 degrees Celsius sea water according to Wang et al. Over a period of 25 years, an average pit growth rate of about 0.1 mm per year is found. Recent unpublished studies imply that the average maximum pit growth rate can be around 0.5 mm per year. Therefore, in this sensitivity study, the effect of changing the parameter d_m to a value of 12.5 mm on the corrosion fatigue in initiation life is investigated.

Figure 6.1 shows the fatigue initiation life results for the original pit growth parameters, and a change in the parameter d_m. Also, the pit growth model for both sets of parameters are shown in the figure. From the data points it can be seen that the influence of this parameter on the fatigue crack initiation life is null. Only for a stress range of 50 MPa a (small) difference in the number of cycles to initiation can be found, which is probably caused by a numerical error. The reason for the similarity in the fatigue crack initiation life results can be found in the linearity of the extrapolation of the stress and strains along a path from the pit bottom down into the material, and the linearity of d_m in the pit growth model. The parameter d_m is a linear factor on the maximum pit depth in equation (6.1), i.e. when d_m is twice the value, the maximum pit depth a and the maximum pit depth growth rate at that moment in time or at that number of cycles is also twice the value. Because the stress and strain along are linear extrapolated as well, this results in an equal amount of accumulated damage for any value of d_m.

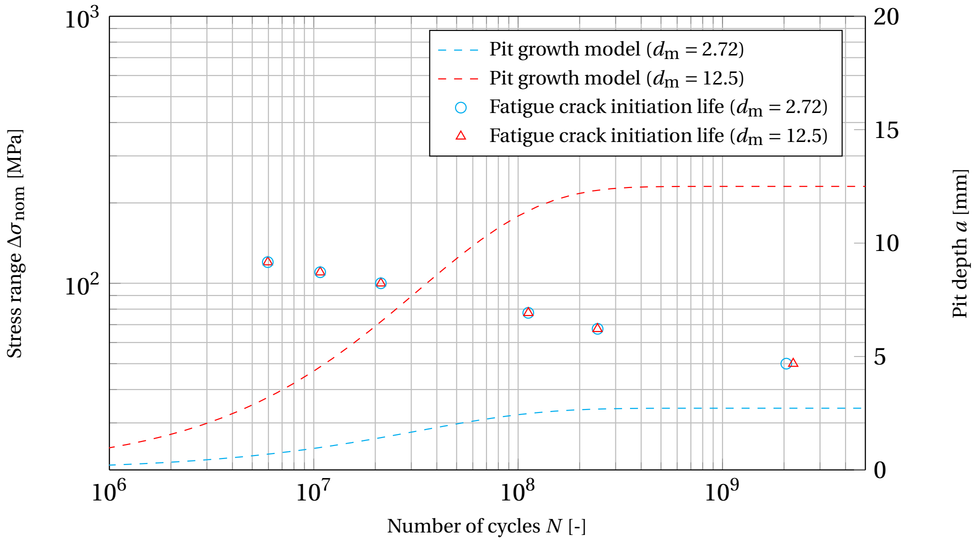

Figure 6.1: Corrosion fatigue initiation life results for an aspect ratio of $AR_\mathrm{p} = 0.5$ for crack initiation at the pit bottom where only the pit growth parameter d_m is varied. The lines represent the pit growth in time for the specified parameters.

Parameter α

Originally, the value of α was determined to be 0.195, corresponding to 5.6 mL dissolved oxygen per litre sea water according to Wang et al. To determine the sensitivity of the pit growth parameter α on the corrosion fatigue model, the effect of changing the value of α to 0.15 and 0.30 is investigated, which corresponds to about 4.5 and 6.5 mL dissolved oxygen per litre sea water respectively according to Wang et al.

Figure 6.2 shows the fatigue crack initiation life results for the original pit growth parameters, and the sets of parameter including changes in the parameter α. Also, the pit growth model for all sets of parameters is shown in the figure. It can be seen that for higher stress ranges, almost no difference is found in fatigue crack initiation life, while the difference is larger for lower stress ranges. For low stress ranges, the moment of fatigue crack initiation strongly depends on the pit growth rate. The lower the pit growth rate, the more damage is accumulated in the material, the sooner a fatigue crack will initiate. A higher value of α results in a higher pit growth rate at the beginning of the pit growth process, and a sooner decrease of the pit growth rate than for lower values for α.

Parameter m

Originally, the value of m was determined to be 0.722, corresponding to A3 steel in the Qingdao Sea according to Wang et al. This steel type and environment is comparable to S355 steel and the North Sea respectively. Wang et al. found no clear correlation between the parameter m and material or environmental parameters. Based on multiple experiments and corresponding pit growth parameters determined by Wang et al., values of 0.5 and 1.0 for the parameter m are chosen to be investigated in this sensitivity study.

Figure 6.3 shows the fatigue crack initiation life results for the original pit growth parameters, and the sets of parameters including changes in the parameter m. Also, the pit growth model for all sets of parameters is shown in the figure. It can be seen that a higher value for m results in higher initiation life at stress ranges above 80 MPa, and lower initiation life at stress ranges below 80 MPa. For lower values for m, the results are the same, but reversed. A lower value of m results in a fast pit growth at the beginning of the pit growth process, and a lower pit growth rate before reaching the maximum pit depth d_m. For higher values of m this is reversed. When the corrosion pit is expanding faster, the competition between the fatigue process and

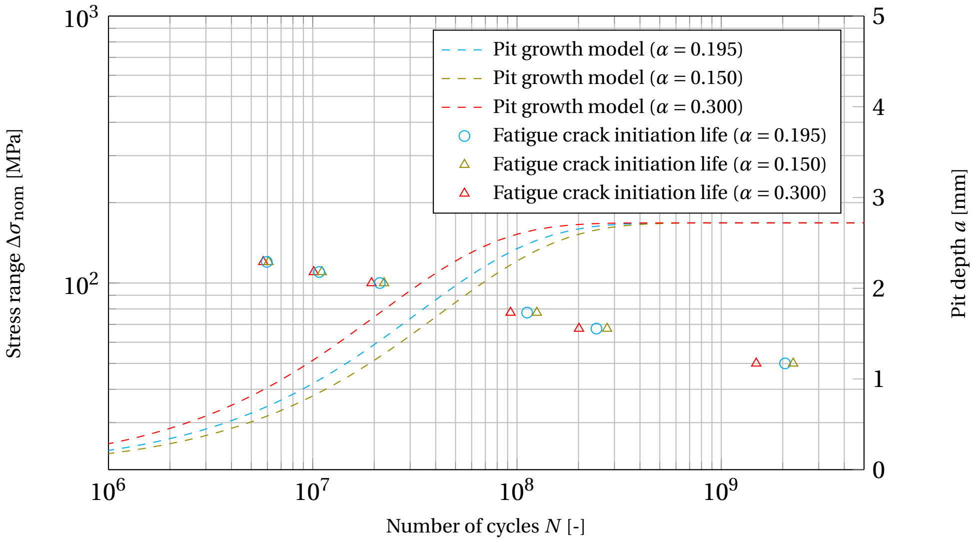

Figure 6.2: Corrosion fatigue initiation life results for an aspect ratio of $AR_{\mathrm{p}} = 0.5$ for crack initiation at the pit bottom where only the pit growth parameter α is varied. The lines represent the pit growth in time for the specified parameters.

the corrosion process is dominated by the corrosion process for a longer period. When the corrosion pit is expanding slower, this competition is dominated by the corrosion process for a shorter period. This explains the variance in fatigue crack initiation life for different values of m.

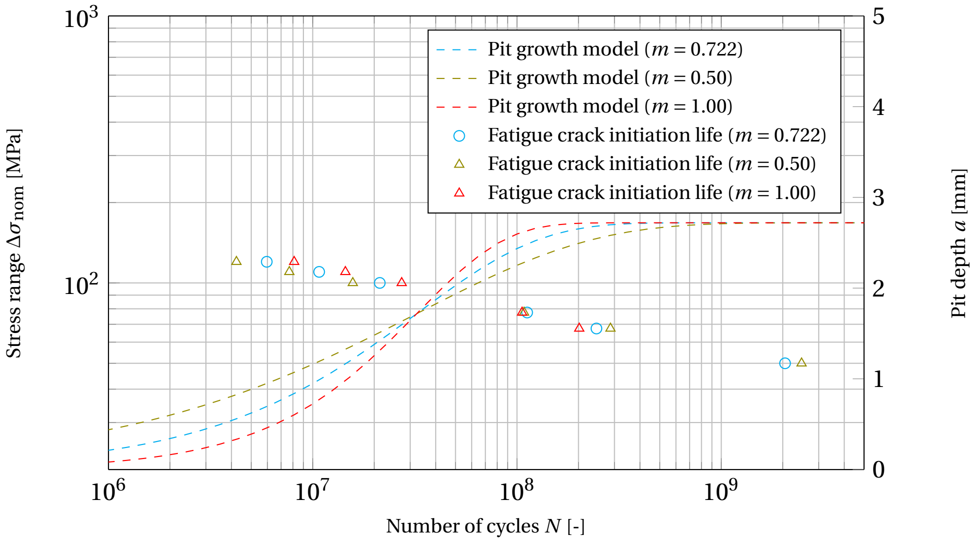

Figure 6.3: Corrosion fatigue initiation life results for an aspect ratio of $AR_{\mathrm{p}} = 0.5$ for crack initiation at the pit bottom where only the pit growth parameter m is varied. The lines represent the pit growth in time for the specified parameters.

6.2. Plastic hardening parameters

The stress-strain relation for stresses above the yield limit, is given in this corrosion fatigue model by the Chaboche hardening model. Originally, hardening parameters determined by Krolo et al. [100] are used in this model. Because a large spread in monotonic and cyclic stress-strain curves was observed in section 3.1.1, different input parameters for the hardening model will be investigated. The kinematic part of the Chaboche hardening model is used to determine the stress-strain curves corresponding to the hardening parameters. The stress-strain curves corresponding to the data and parameters of De Jesus, Ghahremani, Mrozinski, and Krolo et al. are shown in figure 6.4.

The parameters of the kinematic part, i.e. C_i and γ_i for i in range 1 to 3, are altered to create a cyclic stress-strain curve comparable to the highest positioned cyclic stress-strain curve. This would result in higher stresses at the same strain amplitude, which could result in lower fatigue initiation life. The isotropic part of the Chaboche hardening model is kept the same. This part consists of the yield limit $\sigma|_0$, the maximum change in size of the yield surface Q_∞, and the rate at which the yield surface size changes given the equivalent plastic strain b. The original and altered parameters of the Chaboche hardening model are shown in table 6.1. The stress-strain curves corresponding to the altered parameters of the Chaboche hardening model are shown in figure 6.4.

Parameter	Original value [100]	Updated value	Unit
$\sigma\|_0$	386	386	MPa
Q_∞	20.8	20.8	MPa
b	3.2	3.2	-
C_1	5327	6000	MPa
γ_1	75	60	-
C_2	1725	2500	MPa
γ_2	16	10	-
C_3	1120	2000	MPa
γ_3	10	10	-

Table 6.1: Chaboche hardening model parameters for S355 steel in air

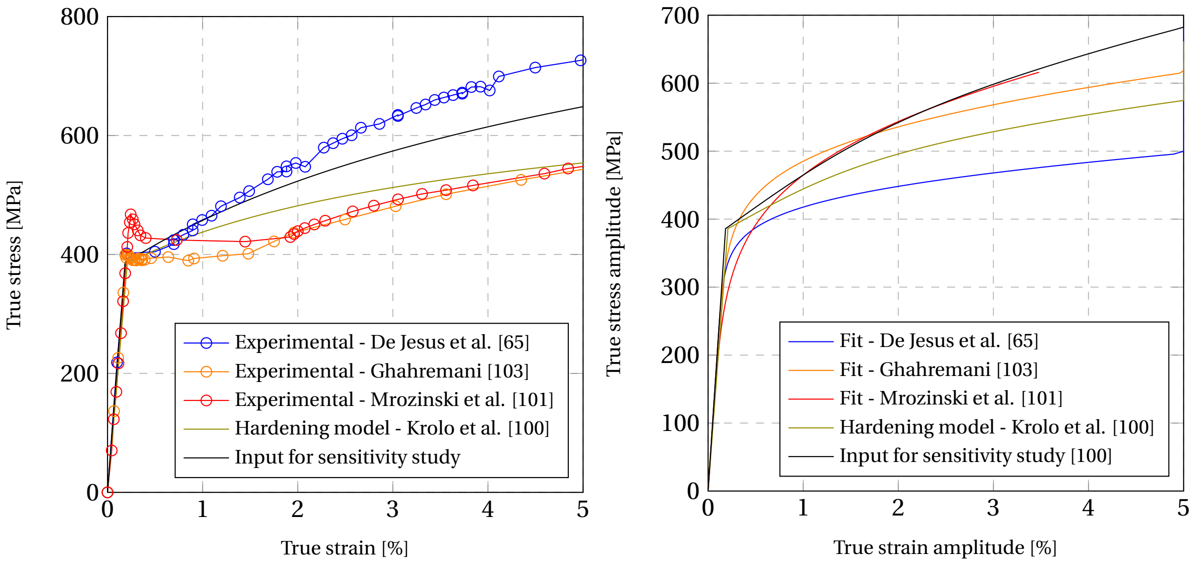

(a) Monotonic stress-strain curves in air

(b) Cyclic stress-strain curves for a fully reversed load

Figure 6.4: Stress-strain curves

Figure 6.5 shows the fatigue crack initiation life results using the original Chaboche hardening parameters, and the updated Chaboche hardening parameters. From the data points a negligible difference can be found due to the change of Chaboche hardening parameters in the corrosion fatigue model. From the stress and strain data from the FEM models, it was found that the difference in the strain ranges between both input parameter sets is negligible, while the stress was about 0.5% higher for the updated Chaboche hardening parameters. This difference is so small, that the effect on the fatigue crack initiation life is negligible.

6.3. Strain-life parameters

The strain-life curve implemented in this corrosion fatigue model is based on the strain-life curve as determined by Mrozinski et al., and is modified for the effect of corrosion (including hydrogen embrittlement) and considers fatigue crack initiation life instead of total fatigue life. This combination of aspects has not been found in any study in which strain-life parameters are determined. Therefore it is not possible to deduct a

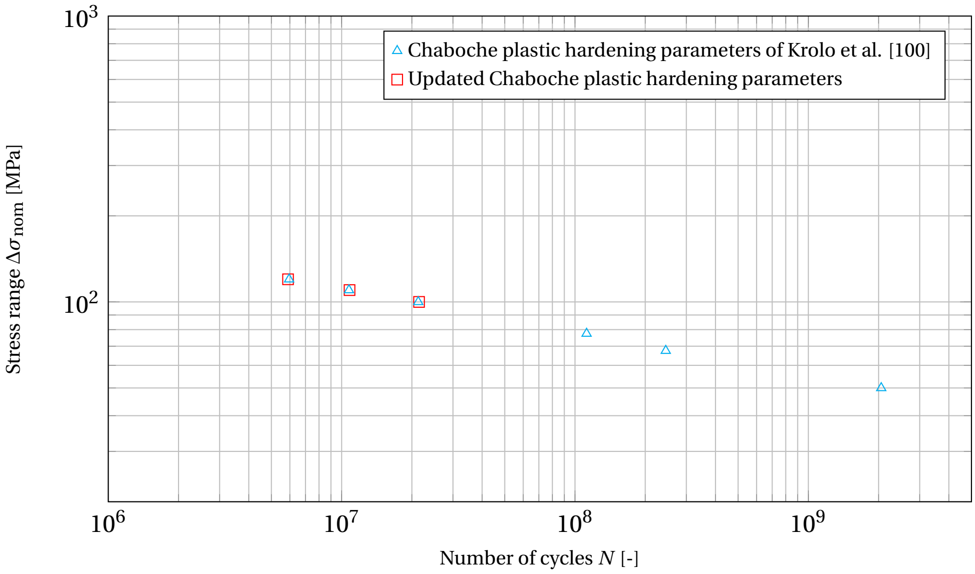

Figure 6.5: Corrosion fatigue initiation life results for an aspect ratio of $AR_{\text{p}} = 0.5$ for crack initiation at the pit bottom where there plastic hardening parameters are varied.

set of parameters which are realistic and different from the strain-life parameters used in the corrosion fatigue model. It has been chosen to apply the standard deviation used in the determination of SN-curves by the DNV GL [66] on the strain-life curve in the sensitivity study. The standard deviation $s_{\log(\text{N})}$ is 0.2, and is applied to the elastic and plastic part of the strain-life curve separately. Next, new strain-life parameters are fitted on the data in the same way as described in appendix B. The strain-life parameters are shown in table 6.2, and the corresponding curves are shown in figure 6.6.

	σ'_{f} [MPa]	b [-]	ϵ'_{f} [-]	c [-]
Original	838	-0.0952	0.0982	-0.519
Upper limit	888	-0.0954	0.160	-0.520
Lower limit	762	-0.0954	0.0616	-0.520

Table 6.2: Strain-initiation life (free corrosion) parameters for sensitivity study

Figure 6.7 shows the fatigue crack initiation life results of the corrosion fatigue model with the different sets of strain-life parameters as input. From the graph it appears that the deviation of the data points of the upper and lower limit strain-life curve from the original data points is larger at higher stress ranges, than at lower stress ranges. Only at the lowest stress range at which the fatigue crack initiation life is determined, a higher deviation can be found. When the standard deviation of both the upper limit as the lower limit data points is calculated, it can be found that the standard deviation of the lower limit data points have a larger standard deviation of $s_{\log(\text{N})} = 0.176$, than the upper limit data points, which have a standard deviation of $s_{\log(\text{N})} = 0.113$. Both standard deviations are lower than the applied standard deviation to the original strain-life curve. A reason for a lower standard deviation can be that the rate of damage accumulation in the material depends largely on the pit growth model as well. At a low fatigue crack initiation life, the fatigue process dominates the total corrosion fatigue process earlier, so the impact of different strain-life parameters will be larger. For the same reason, the pit growth model has a larger effect on the fatigue crack initiation at lower stress ranges. Though, at a certain moment in time, the pit growth rate is decreased such significantly, that the corrosion pit is almost not expanding. At this moment the fatigue process will start to dominate, which results in a larger effect of different strain-life parameters. This effect can be seen at the fatigue crack initiation life data points at a stress range of 50 MPa in figure 6.7.

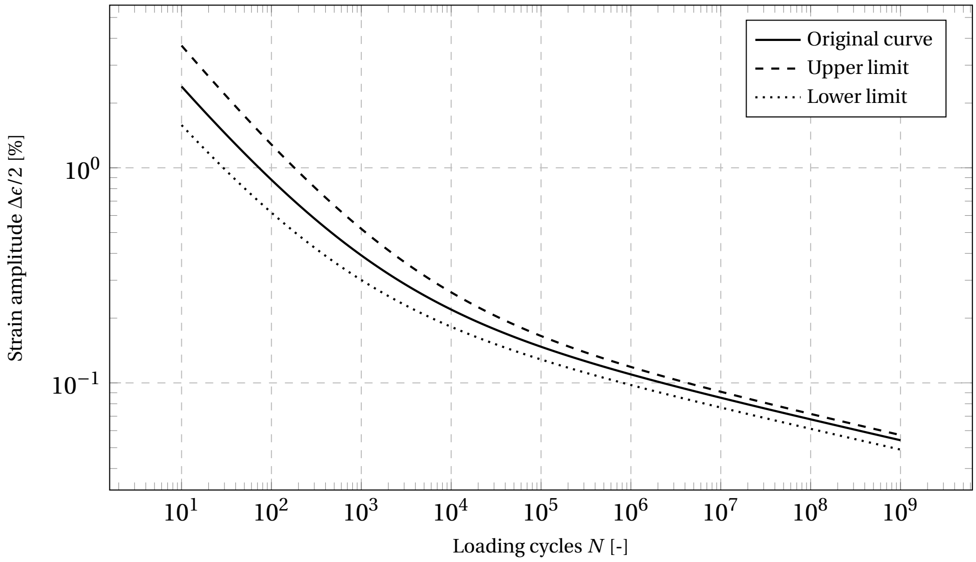

Figure 6.6: Strain-initiation life curve in free corrosion including standard deviation of $s_{\log(\mathrm{N})} = 0.2$

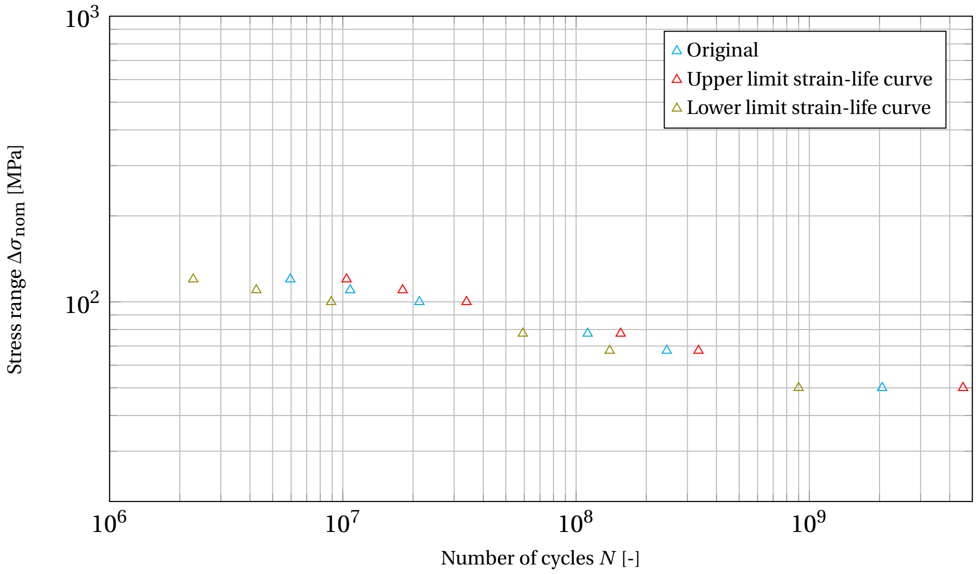

Figure 6.7: Corrosion fatigue initiation life results for an aspect ratio of $AR_\mathrm{p} = 0.5$ for crack initiation at the pit bottom where the strain-life parameters are varied by a standard deviation of $s_{log(N)} = 0.2$.

6.4. Stress ratio

A stress ratio of 0.5 is chosen in this study, because this can be expected in foundations of wind turbines at sea. A higher stress ratio of 0.8 may be expected in welds, where residual stresses increase the mean stress. For completeness, the effect of a lower stress ratio of 0.2 on the corrosion fatigue results is investigated as well in this sensitivity study.

Figure 6.8 shows the fatigue crack initiation life results of the corrosion fatigue model with different stress ratios. Because the corrosion fatigue model uses the maximum nominal stress as input parameter, the stress ranges of the data points do not match in this figure.

From the results it can be found that the effect of a different stress ratio is resulting in a larger deviation from the original results at low stress ranges than at high stress ranges.

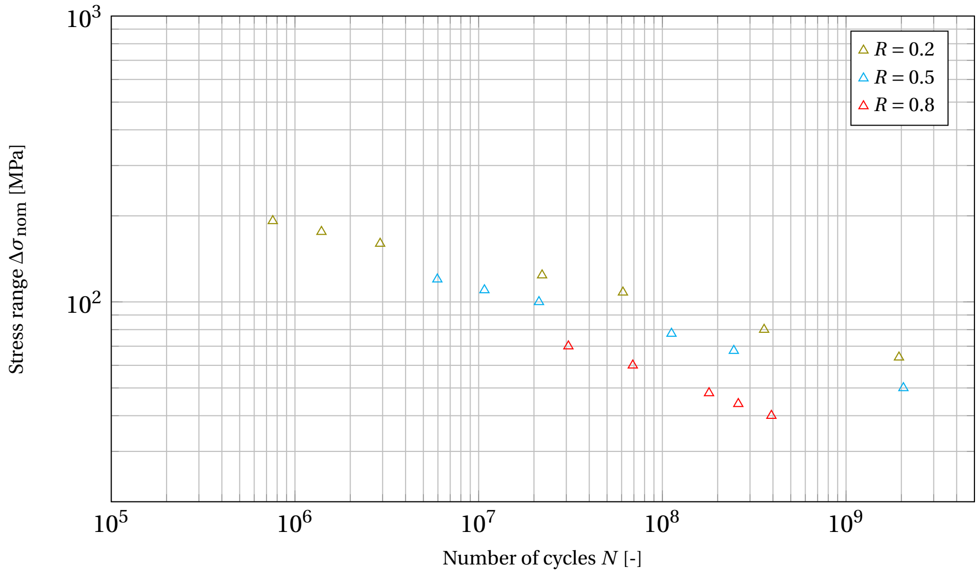

Figure 6.8: Corrosion fatigue initiation life results for an aspect ratio of $AR_{\text{p}} = 0.5$ for crack initiation at the pit bottom where the stress ratio R is varied.

6.5. Load frequency

The frequency of the cyclic loading is an important parameter in the corrosion fatigue model, because it is the factor that couples the cycle dependent fatigue process to the time dependent corrosion process. In the corrosion fatigue model, the frequency is implemented as a constant. As mentioned in section 5.1, this could be unrealistic, because low stress ranges will be more frequent in the load spectrum of a wind turbine foundation than high stress ranges. The constant load frequency applied in the corrosion fatigue model is 0.2 Hz, which is based on the average wave frequency in the North Sea. In this section, the influence of a factor 10 higher and lower frequency of 2.0, and 0.02 Hz respectively, on the fatigue crack initiation life will be investigated.

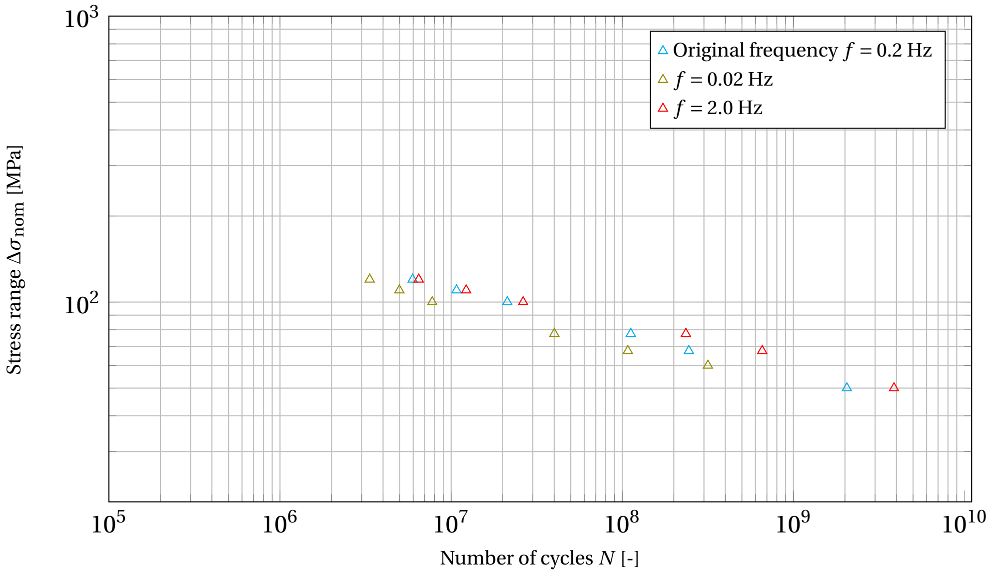

Figure 6.9: Corrosion fatigue initiation life results for an aspect ratio of $AR_{\text{p}} = 0.5$ for crack initiation at the pit bottom where the load frequency f is varied.

Figure 6.9 shows the fatigue crack initiation life results of the corrosion fatigue model with different (constant) load frequencies. From the results it can be found that the influence of the load frequency is higher at low stress ranges. At high stress ranges, the corrosion fatigue life results tend to follow the same line, where a larger spread is found at lower stress ranges. This is due to the fatigue process being more dominating at high stress ranges than the corrosion process, due to a higher damage per cycle. At low stress ranges, the corrosion process, i.e. the pit growth, has more influence, which is shifted in the SN-diagram by the frequency.

It can also be found that for very low stress ranges, the spread in the fatigue initiation life results appears to become slightly lower. For a lower frequency, this effect is found to appear at higher stress ranges with respect to higher frequencies. This effect is due to the pit growth model. The pit growth rate is decreasing according to the pit growth model until a maximum pit depth is reached. This means that the pit depth is changing less and less, which means that after a certain amount of time, the pit depth will be equal for different frequencies. Because of the history, a difference in accumulated damage at the pit surface is found at this moment in time, but after a larger amount of time, this difference will become lower. This results in a lower spread in the fatigue crack initiation life results at very low stress ranges. Note that the definition of these very low stress ranges is dependent on the load frequency.

6.6. Combined case and comparison to DNV GL SN-curves

It has been found in chapter 4 that a comparison of the results of this research work with SN-curves of the DNV GL standard is hard, due to the large uncertainty of the input parameters. Sections 6.1 to 6.5 show the impact of each input parameter of the developed corrosion fatigue model separately. This section shows the effect of two combined cases of changing the pit depth model parameters, strain-life parameters, stress ratio, and load frequency. The first case is the lower case, which takes of each input parameter the parameter that shifts the resulting data points in the SN-diagram to the left. The second case is the upper case, which takes of each parameter the parameter that shifts the resulting data points in the SN-diagram to the right. The combination of input parameters is given in table 6.3. The stress-strain parameters are not changed, because in section 6.2 it has been found that this has a negligible effect. It must be noted that this combination of parameters does not represent an upper or lower limit of the fatigue crack initiation life results, but these cases are presented to give insight into the combined sensitivity of the developed corrosion fatigue model, and with that also insight into the conservativism of the SN-curves of the DNV GL standard.

Parameter		Original	Lower case	Upper case
Pit depth parameters	d_m [mm]	2.72	2.72	2.72
	α [-]	0.195	0.300	0.150
	m [-]	0.722	1.00	0.50
Strain-life parameters	σ'_f [MPa]	838	762	888
	b [-]	-0.0952	-0.0954	-0.0954
	ϵ'_f [-]	0.0982	0.0616	0.160
	c [-]	-0.519	-0.520	-0.520
Stress ratio	R [-]	0.5	0.8	0.2
Load frequency	f [Hz]	0.2	0.02	2.0

Table 6.3: Combination of input parameters for two cases.

Figure 6.10 shows the fatigue crack initiation life results of the combined cases as presented in table 6.3. The graph also shows the mean, and design B1-curve of the DNV GL standard in free corrosion conditions. It can be seen from the graph, that the combined cases show a significant spread of the data points compared to the original data points, and the spread found from in sections 6.1 to 6.5. The lower case is found to be nearing the B1 design SN-curve of the DNV GL standard.

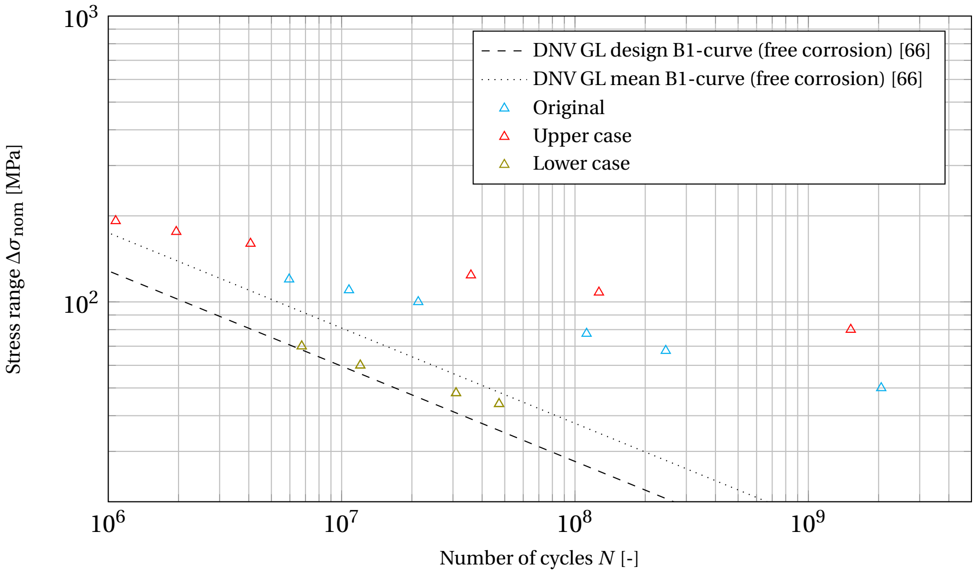

Figure 6.10: Corrosion fatigue initiation life results for an aspect ratio of $AR_{\text{p}} = 0.5$ for crack initiation at the pit bottom. The results of two combined cases, implementing the input parameters from table 6.3, are shown.

6.7. Discussion and conclusions

This section discusses the results of the sensitivity study performed in this chapter. The first part discusses the fatigue crack initiation life time, which is assumed to be equal to the moment of the pit-to-crack transition in this study. The second part discusses the location of the pit-to-crack transition in the corrosion pit.

Fatigue crack initiation life

The maximum pit depth model of Wang [26] consists of three parameters, of which d_m denotes the pit depth after an infinite amount of time. This parameter scales the pit depth linearly, which is, combined with the finding that the stress gradient scales linearly with the pit depth, and the SCF is constant up to a pit depth of 20% of the plate thickness, the reason that there is no effect of this parameter on the fatigue crack initiation life up to this depth. The parameters α and m describe the rate at which the maximum pit depth d_m is reached. These parameters have a larger influence on the fatigue crack initiation life. It has been found that the influence is larger at the moments in time where the pit growth rate is different, because at these moments, the competition between the SCF and stress gradient is influenced by the pit growth.

The influence of the parameters used in the Chaboche hardening model on the pit-to-crack transition has been found to be negligible. The maximum value of the maximum principal plastic strain has been decreased by about 1.5% (on plastic strains in the order of 0.06%) for a nominal stress range of 120 MPa. The maximum strain range at the pit bottom is in the order of 0.11% for a nominal stress range of 120 MPa. It can be concluded that the stress ranges are too low for the plastic strain to be affected significantly by the stress-strain parameters for this geometry. For a geometry that includes surface roughness, the effect may be larger due to the larger SCF, but due to the large stress gradient the effect will be limited.

There is a large uncertainty on the strain-life parameters due to the small number of experiments available in literature on strain-life parameters in free corrosion, especially for S355 steel only. Therefore it is of importance to understand the influence of these parameters on the pit-to-crack transition results. It has been found that by changing the strain-life curve with a standard deviation of 0.2, the fatigue crack initiation life results shift with a 10-45% lower standard deviation. Due to the competition between the corrosion process and the fatigue process, the standard deviation is lower than when only the fatigue process would affect the pit-to-crack transition. Difference in the standard deviation of individual fatigue crack initiation life data points has been found to be influenced by the pit growth rate.

The stress ratio has been found to affect the fatigue crack initiation life significantly at low nominal stress ranges, and less significant at high nominal stress ranges. This could be caused by the strain range converging at higher nominal stress ranges due to plasticity. At a higher stress ratio, the maximum stress will be at the yield stress at a lower stress range, than at a lower stress ratio. Therefore, the results at a higher stress ratio tend to converge towards the original results from lower stress ranges on, than the results at a lower stress ratio. At welds the stress ratio could be higher than the 0.5 as implemented in this research work, due to residual stresses. Therefore, it will be important to investigate this input parameter further.

The load frequency has been assumed to be constant in this study. In reality, the frequency will be higher for low stress ranges, than for high stress ranges, because these stress ranges are more frequent in the load spectrum of wind turbine foundations. This will mean that the resulting SN-curve for a variable frequency will be less steep than the SN-curve for a constant load frequency. The difference in fatigue crack initiation life between the different frequencies investigated in this chapter has been found to be higher at low stress ranges, than high stress ranges. This is due to the fatigue process being more dominant in the high stress ranges, due to the larger amount of damage per load cycle. More research on the load frequency of the stress ranges will be necessary to be able to use the developed model in engineering solutions.

The only input parameter that has not been taken into account in this sensitivity study is the wall thickness of the wind turbine foundation. It has been found that the influence of the wall thickness on the stress and strain levels at and below the corrosion pit surface up to a pit depth of at least 20% of the wall thickness is negligible. When the pit depth is larger, the linear extrapolation to obtain the maximum stress and strain range paths, as implemented in the developed model, might be invalid.

The combined case, as presented in section 6.6, gives insight in the sensitivity of the model to a change in all input parameters discussed in this chapter. The parameters have been varied in such a way, that a lower and a upper case is found, according to the variations of input parameters discussed in this chapter. This means that these cases do not represent an upper and lower limit, because the variations of input parameters are not based on realistic data, but are educated estimates. Nevertheless, the results of the two combined cases can be used to give insight in the comparison of the results of the developed model to the DNV GL standard SN-curves for free corrosion conditions. It has been found, that for the original input parameters, the SN-curve of DNV GL appears to be conservative, as seen in chapter 4. From the results in this chapter, it has been found that the lower case nears the design B1 SN-curve of the DNV GL standard. Also the slope of the results of the lower case nears the slope of the B1 SN-curve. These results are for an aspect ratio of $AR_\mathrm{p} = 0.5$. It has been found that a sharper pit has a lower fatigue life, and the corresponding curve will therefore probably be positioned left of the B1 SN-curve. It must be noted that the developed corrosion fatigue model does not implement fatigue crack propagation life, where the SN-curve does. This means that the data points will shift to the right, when propagation life is added to the model. Also, the variations on the original input parameters are an estimation, and could be unrealistic. The results imply that the DVNGL B1 SN-curve for free corrosion conditions may not be necessarily conservative, although it is doubtful whether pitting corrosion has occurred in the tests on which the DNV GL B1 SN-curve is based upon, due to the relatively short exposure to free corrosion conditions. More research is necessary on the input parameters, to be able to reduce the spread on the fatigue crack initiation life results of corrosion pits.

Pit-to-crack transition location

The effect of the parameters studied in this chapter on the location of the pit-to-crack transition in the corrosion pit has not been investigated. Though it is expected that this effect is negligible. None of the parameters have an effect on either the SCF or stress gradient only, or significantly more on one or the other. Therefore, via this parameter no significant difference will be caused in the location of the pit-to-crack transition. Due to different pit growth parameters or frequency, the pit growth relative to the number of cycles will change. This could have an effect on the location of the pit-to-crack transition by making the influence of the stress gradient compared to the SCF larger. Though, because the stress range does not have a significant influence on the location of the pit-to-crack transition, and at the number of cycles to initiation at high stress ranges the pit growth rate is higher than at low stress ranges, it is expected that the parameters investigated in this chapter do not have a significant influence on the location of the pit-to-crack transition as well.

7

Conclusions & recommendations

This chapter provides conclusions based on the results and discussions as given in this research work. Next, recommendations for future work are given with respect to experimental and modelling work.

7.1. Conclusions

Both the corrosion process and the fatigue process are research fields on their own. The combination of both processes is studied well, though a complete understanding of the significance of all parameters of influence on this process is not yet available in literature. In particular, the transition from a corrosion pit (a time-dependent process) to a fatigue crack (a cycles-dependent process) is a relatively unknown, but important process. When a better prediction of the pit-to-crack transition can be made, design studies of steel offshore structures can allow for the impact of corrosion fatigue with over-conservative nor ignorant design choices. Current models that predict the pit-to-crack transition are phenomenological and do not consider local mechanics and interaction between the material variables, environmental (chemistry) variables, and applied load.

One of the main objectives of this research study is to create a model, that is able to predict the moment in time, and the location in the corrosion pit of the pit-to-crack transition. The hypothesis used in the development of the corrosion fatigue model, is that the pit-to-crack transition occurs at the moment of the initiation of a fatigue crack, which can be predicted based on the stress and strain history in the material.

Corrosion fatigue model

The methodology that has been used in the developed corrosion fatigue model covers the basic principles of the corrosion fatigue process. The developed model gives a comprehensive basis, which can be expanded to be finally implemented in engineering solutions. Burns et al. [93] identified four driving forces of the pit-to-crack transition: (i) geometry, (ii) strain and local plasticity, (iii) hydrogen embrittlement, and (iv) chemical processes. In the developed model, different pit shapes (macro-topography) have been taken into account, and also surface roughness (micro-topography) is implemented. Strain and local plasticity have been taken into account in the model by using the strain-life equation to determine the fatigue crack initiation life. Hydrogen embrittlement is not implemented in the stress-strain relation used in the developed model, because the degree and extend into the material of the effect of hydrogen absorption is relatively unknown. Although, it has been found that different plastic hardening parameters do not influence the pit-to-crack transition significantly. Hydrogen embrittlement also influences the strain-life behaviour of steel, which has been implemented using data of Bignonnet et al. [76]. The influence of chemical processes on the pit-to-crack transition has only been taken into account globally by means of the pit growth model of Wang [26]. The influence of local chemical solution is not implemented, due to the little available literature that is documented such that it can be used as input in the developed model. The influence of local solution chemistry on the pit shape and depth is expected to be of importance, and it has been found that a different pit growth rates and corrosion pit shapes can affect the pit-to-crack transition significantly. Linearly scaling the pit growth model has been found to have no influence on the pit-to-crack transition. This is because the stress concentration factor of a corrosion pit is independent of the thickness of the specimen up to a pit depth of 20% of the specimen thickness, and the stress and strain paths from the corrosion pit surface into the material is linearly scalable by the pit depth.

The results of the corrosion fatigue model depend on the assumptions and simplifications made in the model, which have been discussed in chapter 3. Summarized, the following assumptions and simplifications have been implemented:

- The global shape of a corrosion pit has been simplified as an ellipse.
- A corrosion pit grows in time following a power function, according to Wang's maximum pit depth model. Therefore, the effect of stress on the pit growth has been neglected, just as the effect of local solution chemistry.
- A corrosion pit has been assumed to grow with a constant aspect ratio.
- Surface roughness has been simplified as certain sized micro-pits. The micro-pits grow equally as the corrosion pit, i.e. remaining its aspect ratio, and the ratio of micro-pit depth with regard to the corrosion pit depth.
- The load frequency has been assumed to be constant for all stress ranges.
- The influence of hydrogen absorption on the stress-strain behaviour has not been taken into account in this thesis due to lack of available research on this influence on steel types.
- Fatigue damage has been determined using Miner's Rule. In the developed model, the applied load has been taken to be constant, but the geometry has not, which could result in changing stress and strain levels in time. This means that sequence effects could occur, but these effects have been assumed to be negligible in this research study.
- The strain-life relation has been used to determine the number of cycles to fatigue crack initiation including the effects of corrosion based on the stress and strain level. To be able to approach fatigue crack initiation based on total life until failure of thin specimen, assumptions have been made with regard to the part of initiation in the total life until failure of strain-life specimen based on the research of Dowling et al. [59, 102]. Because Dowling et al. performed low cycle fatigue tests only, fatigue crack initiation life has been assumed to be 70% of the total fatigue life in the high cycle fatigue region. Also, Dowling et al. found a large spread, so a mathematical function has been fitted through these points. The effect of free corrosion on the fatigue crack initiation life has been implemented using a factor found from the research of Bignonnet et al. [76]. This research performed mainly low cycle fatigue tests, and also the number of tests is limited.

Fatigue crack initiation life

Typically, steel offshore structures are designed in accordance with the DNV GL standards. The fatigue crack initiation life found by the developed model can be compared to the SN-curves of base material in free corrosion of DNV GL, but only by taking notice that the SN-curves include fatigue crack propagation life, where the corrosion fatigue model of this study does not. Also, one should take into account the assumptions made in the developed model, which influence the results of the corrosion fatigue model.

A comparison between experiments and the fatigue crack initiation life of the developed corrosion fatigue model has not been made, due to the lack of comparable experiments. Corrosion fatigue experiments that include a fatigue loading while a corrosion pit is expanding due to the corrosive environment have been little found, and all without enough documentation to use it as input values to validate the corrosion fatigue model. This is not illogical, due to the large number of parameters involved in the corrosion fatigue process, and the difficulty of accelerating the corrosion process in a controlled way. Therefore, the final results of the model have not been validated in this study. Most input values are based on experimental or field data.

The following conclusions can be drawn with regard to the fatigue crack initiation life:

- From the results it has been found that the fatigue crack initiation life of perfectly elliptic corrosion pits is larger than the total fatigue life given by the SN-curves for the same stress ranges for the input parameters given in chapter 3. The model also shows that the slope of the fatigue crack initiation results ($m \approx 6$) is more flat compared to the SN-curve of DNV GL in free corrosion conditions ($m = 3$). From the sensitivity study it has been found that a combination of changes in the input parameters results in a significant spread in the fatigue crack initiation life results, and that it could result in fatigue crack initiation life close to the DNV GL SN-curve for free corrosion conditions. It can be concluded that more (experimental) research is necessary on the input parameters, to be able to reduce the spread on the fatigue crack initiation life results of corrosion pits, and to draw any conclusions with regard to the SN-curves of DNV GL in free corrosion conditions.

- From the results it has been found that a fatigue crack will initiate from a sharp corrosion pit earlier than from a more blunt corrosion pit for an equal applied stress range. The slope of the data points of the pit-to-crack transition in an SN-diagram is for each aspect ratio about equal.
- The process of fatigue crack initiation in corrosion pits can be seen as a competition between the corrosion and the fatigue process. In the developed corrosion fatigue model, this competition can be seen as a competition between the maximum pit depth model, stress concentration factor, and the stress gradient.
- Surface roughness has been found to have a significant influence on the fatigue crack initiation life, specifically for low stress ranges, where at the moment of fatigue crack initiation the pit growth has come to arrest. This is not realistic, because the load frequency has been taken as a constant in this research, and in reality the load frequency is dependent on the nominal stress range. The effect of the frequency on the fatigue crack initiation life results has been found to be significant. A variable load frequency will result in a more flat SN-curve in free corrosion compared to a constant load frequency. Because of the dependency of the fatigue crack initiation life including surface roughness on the load frequency, no factor between the fatigue crack initiation life results including and excluding surface roughness could be established.
- From the sensitivity study on the developed corrosion fatigue model, it has also been found that the influence of the strain-life parameters, and the stress ratio on the pit-to-crack transition life is significant. More research is necessary to establish these input parameters for wind turbine foundations in free corrosion conditions.

Fatigue crack initiation location

Some current models available in literature that predict the pit-to-crack transition, assess the corrosion pit as a crack, and thereby imply that a fatigue crack will propagate from the pit bottom. Some experimental studies show cracks initiate at the pit bottom [24], where others show cracks initiate at the pit wall/mouth [86, 96], or at both locations [15, 93]. In this study, for perfectly elliptical corrosion pits, it was found that the location of fatigue crack initiation strongly depends on the pit aspect ratio.

The pit wall/mouth has been found to be a more favourable location for fatigue crack initiation in a sharp corrosion pit (AR_p = 1.00), where the pit bottom is a more favourable location for fatigue crack initiation in a blunt corrosion pit (AR_p = 0.25). For circular shaped corrosion pits (AR_p = 0.50), the difference between the fatigue crack initiation life at the pit wall and the pit bottom is found to be negligible.

7.2. Recommendations for future work

Following the discussions and conclusions from this research work, recommendations for future research works are listed in this section. The recommendations are split up in experimental works, and modelling works.

Experiments

Due to the large number of parameters involved in the pit-to-crack transition, it is hard to identify the degree of influence of each parameter by performing realistic corrosion fatigue experiments that involve all parameters. The influence of each parameter will need to be identified by experiments where the parameter is uncoupled from other parameters. This way the influence of each parameter can also be taken into account in a corrosion fatigue model as developed in this study.

The effect of the following processes are identified as possible experimental research topics:

- The effect of hydrogen absorption (hydrogen embrittlement) on the fatigue crack initiation and stress-strain behaviour of S355 hot-rolled steel, including regarding the depth up to which hydrogen absorption is of importance.
- The effect of stress and plasticity on the (local) pit growth rate and thereby the pit shape and depth.
- The effect of local solution chemistry on the (local) pit growth rate and thereby the pit shape and depth.

- Strain-life behaviour of hot-rolled S355 steel for fatigue crack initiation, and its relation to the total fatigue life of strain-life experiments, especially in the high cycle fatigue region.

Modelling
The developed corrosion fatigue model can be expanded in many ways. A number of options is listed below:

- The developed corrosion fatigue model can be expanded by coupling it to a numerical pit growth model instead of an analytic maximum pit depth model. This way, the effect of local mechanics (stress and strain) and local solution chemistry to the pit shape could be taken into account in the determination of the fatigue crack initiation life if the corrosion pit growth model allows this. A disadvantage of this coupling is that the computation time will increase significantly, mainly due to a significant increase in the amount of FEM calculations.

- The developed corrosion fatigue model can be expanded by implementing multiple corrosion pits in the FEM models, such that an interaction will appear between the corrosion pits. This could affect the fatigue crack initiation life significantly, as has been found experimentally by Fatoba [15].

- The developed corrosion fatigue model can be expanded by including the geometry and material parameters of welds. Welds are typically more favourable locations for fatigue crack initiation than a steel plate, which is regarded in this research work. It would be interesting to investigate whether the effect of welds on the fatigue life of a steel plate in a corrosive environment is equal to the effect of welds on the fatigue life of a steel plate in air.

Bibliography

[1] WindEurope Business Intelligence. Wind energy in europe in 2018. Technical report, WindEurope, 2019.

[2] WindEurope Business Intelligence. Offshore wind in europe. Technical report, WindEurope, 2018.

[3] D. Moulas, M. Shafiee, and A. Mehmanparast. Damage analysis of ship collisions with offshore wind turbine foundations. *Ocean Engineering*, 143:149 – 162, 2017.

[4] Z.C. Petrovic. Catastrophes caused by corrosion. *Military Technical Courier*, 64(4):1048–1064, 2016.

[5] J. Kruger. *Cost of Metallic Corrosion*, chapter 2, pages 15–20. John Wiley & Sons, Ltd, 2011.

[6] B.N. Popov. Chapter 1 - Evaluation of corrosion. In B.N. Popov, editor, *Corrosion Engineering*, pages 1 – 28. Elsevier, Amsterdam, 2015.

[7] V. Igwemezie, A. Mehmanparast, and A. Kolios. Materials selection for XL wind turbine support structures: A corrosion-fatigue perspective. *Marine Structures*, 61:381–397, 2018.

[8] NEN-EN. Hot rolled products of structural steels - part 2: Technical delivery conditions for non-alloy structural steels. Standard, NEN-EN 10025-2, 2019.

[9] A. McCafferty. *Introduction to Corrosion Science*. Springer, New York, 2010.

[10] J. Bhandari, F. Khan, R. Abbassi, V. Garaniya, and R. Ojeda. Modelling of pitting corrosion in marine and offshore structures - a technical review. *Journal of Loss Prevention in Process Industries*, 2015:39–62, 2015.

[11] R.E. Melchers. Modeling of marine immersion corrosion for mild and low-alloy steels-part 1: phenomenological model. *Corrosion Science*, 59(4):319–334, 2003.

[12] R.E. Melchers. Pitting corrosion of mild steel in marine immersion environment - part 1: maximum pit depth. *Corrosion*, 60(9):824–836, 2004.

[13] B. Baroux. Further insights on the pitting corrosion of stainless steels. In P. Marcus, editor, *Corrosion Mechanisms in Theory and Practice*, pages 419–447. CRC Press, Boca Raton, 2011.

[14] J. Telegdi, A. Shaban, and L. Trif. 8 - Microbiologically influenced corrosion (MIC). In A.M. El-Sherik, editor, *Trends in Oil and Gas Corrosion Research and Technologies*, Woodhead Publishing Series in Energy, pages 191 – 214. Woodhead Publishing, Boston, 2017.

[15] O.O. Fatoba. *Experimental and modelling studies of corrosion fatigue damage in a linepipe steel*. PhD thesis, University of Manchester, 2015.

[16] J. Ma, B. Zhang, J. Wang, G. Wang, E.-H. Han, and W. Ke. Anisotropic 3d growth of corrosion pits initiated at mns inclusions for a537 steel during corrosion fatigue. *Corrosion Science*, 52:2867–2877, 2010.

[17] E.M. Gutman. *Mechanochemistry of Materials*. Cambridge International Science Publishing, Cambridge, 1998.

[18] L. Guan, B. Zhang, X.P. Yong, J.Q. Wang, E.-H. Han, and W. Ke. Effects of cyclic stress on the metastable pitting characteristic for 304 stainless steel under potentiostatic polarization. *Corrosion Science*, 93:80–89, 2015.

[19] R. Ebara. Corrosion fatigue crack initiation behavior of stainless steels. *Procedia engineering*, 2:1297–1306, 2010.

[20] S. Ishihara, S. Saka, Z.Y. Nan, T. Goshima, and S. Sunada. Prediction of corrosion fatigue lives of aluminium alloy on the basis of corrosion pit growth law. *Fatigue & Fracture of Engineering Materials & Structures*, 29(6):472–480, 2006.

[21] R. Akid. 2.12 - Corrosion fatigue. In B. Cottis, M. Graham, R. Lindsay, S. Lyon, T. Richardson, D. Scantlebury, and H. Stott, editors, *Shreir's Corrosion*, pages 928–953. Elsevier, Oxford, 2010.

[22] A. Turnbul. 6.04 - Environment-assisted fatigue in liquid environments. In I. Milne, R.O. Ritchie, and B. Karihaloo, editors, *Comprehensive Structural Integrity*, pages 163–210. Pergamon, Oxford, 2003.

[23] M. Romanoff. *Underground corrosion*. Circular of the National Bureau of Standards. National Bureau of Standards, United States, 1957.

[24] Y. Kondo. Prediction of fatigue crack initiation life based on pit growth. *Corrosion Science*, 45(1):7–11, 1989.

[25] J.C. Velázquez, J.A.M. Van der Weide, E. Hernández, and H.H. Hernández. Statistical modelling of pitting corrosion: Extrapolation of the maximum pit depth-growth. *International Journal of Electrochemical Science*, 9:4129–4143, 2014.

[26] Y.-W. Wang, Y.-F. Wang, X.-P. Huang, and W.-C. Cui. A simplified maximum pit depth model of mild and low alloy steels in marine immersion environments. *Journal of Ship Mechanics*, 12(3):401–417, 2008.

[27] R.E. Melchers. Pitting corrosion of mild steel in marine immersion environment - part 2: variability of maximum pit depth. *Corrosion*, 60(10):937–944, 2004.

[28] R.E. Melchers. A review of trends for corrosion loss and pit depth in longer-term exposures. *Corrosion and materials degradation*, 1:42–58, 2018.

[29] F. Blekkenhorst, G.M. Ferrari, C.J. Van der Wekken, and F.P. IJsseling. Development of high strength low alloy steels for marine applications - part 1: Results of long term exposure tests on commercially available and experimental steels. *British Corrosion Journal*, 21(3):163–176, 1986.

[30] S. Jafarzadeh, Z. Chen, and F. Bobaru. Computational modeling of pitting corrosion. *Corrosion Reviews*, 37(5):419–439, 2019.

[31] S. Scheiner and C. Hellmich. Finite volume model for diffusion- and activation-controlled pitting corrosion of stainless steel. *Comput. Methods Appl. Mech. Engrg.*, 198:2898–2910, 2009.

[32] H. Wang and E.-H. Han. Simulation of metastable corrosion pit development under mechanical stress. *Electrochimica Acta*, 90:128–134, 2013.

[33] C Evans, R. Leiva-Garcia, and R. Akid. Strain evolution around corrosion pits under fatigue loading. *Theoretical and Applied Fracture Mechanics*, 95:253–260, 2018.

[34] Z. Chen and F. Bobaru. Peridynamic modeling of pitting corrosion damage. *Journal of the Mechanics and Physics of Solids*, 78:352–381, 2015.

[35] R. Duddu. Numerical modeling of corrosion pit propagation using the combined extended finite element and level set method. *Computational Mechanics*, 54:613–627, 2014.

[36] W. Mai, S. Soghrati, and R.G. Buchheit. A phase field model for simulating the pitting corrosion. *Corrosion Science*, 110:157–166, 2016.

[37] A.A. Ahmed, M. Mhaede, M. Wollmann, and L. Wagner. Effect of surface and bulk plastic deformations on the corrosion resistance and corrosion fatigue performance of AISI 316L. *Surface & Coatings Technology*, 259:448–455, 2014.

[38] S.J. Price and R.B. Figueira. Corrosion protection systems and fatigue corrosion in offshore wind structures: current status and future perspectives. *Coatings*, 7(2), 2017.

[39] K. Komai. 4.13 - Corrosion fatigue. In I. Milne, R.O. Ritchie, and B. Karihaloo, editors, *Comprehensive Structural Integrity*, pages 345 – 358. Pergamon, Oxford, 2003.

[40] R. Hill and A. L. Perez. 26 - New steels and corrosion-resistant alloys. In A.M. El-Sherik, editor, *Trends in Oil and Gas Corrosion Research and Technologies*, Woodhead Publishing Series in Energy, pages 613 – 626. Woodhead Publishing, Boston, 2017.

[41] C.D. Lykins, S. Mall, and V. Jain. An evaluation of parameters for predicting fretting fatigue crack initiation. *International Journal of Fatigue*, 22:703–716, 2000.

[42] J. Polák. Cyclic deformation, crack initiation, and low-cycle fatigue. In *Reference Module in Materials Science and Materials Engineering*. Elsevier, Amsterdam, 2016.

[43] K.S. Chan. Roles of microstructure in fatigue crack initiation. *International Journal of Fatigue*, 32:1428–1447, 2010.

[44] S.-T. Tu and X.-C. Zhang. Fatigue crack initiation mechanisms. In *Reference Module in Materials Science and Materials Engineering*. Elsevier, Amsterdam, 2016.

[45] M.D. Sangid. The physics of fatigue crack initiation. *International Journal of Fatigue*, 57:58–72, 2013.

[46] J. Schijve. *Fatigue of Structures and Materials*. Springer Netherlands, 2009.

[47] A. Pineau, D.L. McDowell, E.P. Busso, and S.D. Antolovich. Failure of metals ii: Fatigue. *Acta Materialia*, 107:484–507, 2016.

[48] D.L. McDowell and F.P.E. Dunne. Micro-structure sensitive computational modeling of fatigue crack formation. *International Journal of Fatigue*, 32:1521–1542, 2010.

[49] A. Nicolas, N.E.C. Co, J.T. Burns, and M.D. Sangid. Predicting fatigue crack initiation from coupled microstructure and corrosion morphology effects. *Engineering Fracture Mechanics*, 220, 2019.

[50] N.O. Larrosa, R. Akid, and R.A. Ainsworth. Corrosion-fatigue: a review of damage tolerance models. *International Materials Reviews*, 63(5):283–308, 2018.

[51] T. Mura and Y. Nakasone. A theory of fatigue crack initiation in solids. *Journal of Applied Mechanics*, 57(1):1–6, 1990.

[52] S. Silitonga, J. Maljaars, F. Soetens, and H.H. Snijder. Survey on damage mechanics models for fatigue life prediction. *HERON*, 58(1):25–60, 2013.

[53] J. Lemaitre and R. Desmorat. *Engineering Damage Mechanics*. Springer, Berlin, Heidelberg, 2005.

[54] G. Masing. Eigenspannungen and verfestigung beim messing. *Proceedings of Second International Congress of Applied Mechanics, Zurich*, 332, 1926.

[55] O.H. Basquin. The exponential law of endurance tests. *Proceedings of Americal Society for Testing and Materials*, 10:625–630, 1910.

[56] L.F. Coffin. A study of the effect of cyclic thermal stresses on a ductile material. *Journal of applied mechanics*, 76:931–950, 1954.

[57] S.S. Manson. Behavior of materials under conditions of thermal stress. In *Heat transfer symposium*, pages 9–75, Ann Arbor, 1953. The University of Michigan Engineering Research Institute.

[58] N.E. Dowling. 4.03 - Local strain approach to fatigue. In I. Milne, R.O. Ritchie, and B. Karihaloo, editors, *Comprehensive Structural Integrity*, pages 77 – 94. Pergamon, Oxford, 2003.

[59] N. E. Dowling. Crack growth during low-cycle fatigue of smooth axial specimens. *American Society for Testing and Materials Technical Publication 637*, pages 97–121, 1977.

[60] J. Morrow. Cyclic plastic strain energy and fatigue of metals. In B. Lazan, editor, *Internal Friction, Damping, and Cyclic Plasticity*, pages 45–87, West Conshohocken, PA, 1965. ASTM International.

[61] K.N. Smith, P. Watson, and T.H. Topper. A stress-strain function for the fatigue of metals. *Journal of Materials*, 5(4):767–778, 1970.

[62] H. Xin and M. Veljkovic. Fatigue crack initiation prediction using phantom nodes-based extended finite element method for s355 and s690 steel grades. *Engineering Fracture Mechanics*, 214:164–176, 2019.

[63] P. Paris and F. Erdogan. A critical analysis of crack propagation laws. *Journal of basic engineering*, 85(4):528–533, 1963.

[64] S. İriç and A.O. Ayhan. Dependence of fracture toughness on rolling direction in aluminium 7075 alloys. In *Acta Physica Polonica A*, volume 132, pages 892–895, 2017.

[65] A.M.P. de Jesus, R. Matos, B.F.C. Fontoura, C. Rebelo, L.S. da Silva, and M. Veljkovic. A comparison of the fatigue behavior between S355 and S690 steel grades. *Journal of Constructional Steel Research*, 79:140–150, 2012.

[66] DNVGL-RP-C203. Fatigue design of offshore steel structures. Standard, DNVGL, 2016.

[67] DNVGL-RP-0416. Corrosion protection for wind turbines. Standard, DNVGL, 2016.

[68] DNVGL-OS-C101. Design of offshore steel structures, general - LRFD method. Standard, DNVGL, 2018.

[69] I. Lotsberg. *Fatigue Design of Marine Structures*. Cambridge University Press, 2016.

[70] R.E. Melchers and R. Jeffrey. Corrosion of long vertical steel strips in the marine tidal zone and implications for ALWC. *Corrosion Science*, 65:26–36, 2012.

[71] D.J. Duquette. Corrosion fatigue. In J.K.H. Buschow, R.W. Cahn, M.C. Flemings, B. Ilschner, E.J. Kramer, S. Mahajan, and P. Veyssière, editors, *Encyclopedia of Materials: Science and Technology*, pages 1686 – 1687. Elsevier, Oxford, 2001.

[72] S.X. Li and R. Akid. Corrosion fatigue life prediction of a steel shaft material in seawater. *Engineering Failure Analysis*, 34:324–334, 2013.

[73] T. Palin-Luc, R. Pérez-Mora, C. Bathias, G. Domínguez, P.C. Paris, and J.L. Arana. Fatigue crack initiation and growth on a steel in the very high cycle regime with sea water corrosion. *Engineering Fracture Mechanics*, 77:1953–1962, 2010.

[74] X.Y. Zhang, S.X. Li, R. Liang, and R. Akid. Effect of corrosion pits on fatigue life and crack initiation. *13th International Conference on Fracture*, 2013.

[75] B.M. Schönbauer, S.E. Stanzl-Tschegg, A. Perlega, R.N. Salzman, N.F. Rieger, A. Turnbull, S. Zhou, M. Lukaszewicz, and D. Gandy. The influence of corrosion pits on the fatigue life of 17-4PH steam turbine blade steel. *Engineering Fracture Mechanics*, 147:158–175, 2015.

[76] A. Bignonnet, J.L. Brazy, C. Vallet, and F. Barrere. The influence of electrochemical parameters on the corrosion fatigue at notches of structural steel. *Steel in Marine Structures*, 37, 1987.

[77] G.S. Chen, K.C. Wan, M. Gao, R.P. Wei, and T.H. Flournoy. Transition from pitting to fatigue crack growth - modeling of corrosion fatigue crack nucleation in a 2024-T3 aluminium alloy. *Materials Science and Engineering*, 219(1-2):126–132, 1996.

[78] F. Farhad, X. Zhang, and D. Smyth-Boyle. Fatigue behaviour of corrosion pits in X65 steel pipelines. *Journal of Mechanical Engineering Science*, 233(5):1771–1782, 2018.

[79] V. Sabelkin, S. Mall, and H. Misak. Investigation into corrosion pit-to-fatigue crack transition in 7075-t6 aluminum alloy. *Materials Engineering and Performance*, 26(6):2535–2541, 2017.

[80] Q. Wang, M. Palakal, and R. Pidaparti. Comparative study of corrosion fatigue in aircraft materials. *AIAA Journal*, 39:325–330, 02 2001.

[81] Y. Murakami and M. Endo. Effects of small defects and non-metallic inclusions. *Engineering fracture mechanics*, 17(1):1–15, 1983.

[82] M.R. Sriraman and R.M. Pidaparti. Crack initiation life of materials under combined pitting corrosion and cyclic loading. *Journal of Materials Engineering and Performance*, 19(1):7–12, 2008.

[83] M. Mao, X. Zhang, Sh. Tu, and F. Xuan. Prediction of crack initiation life due to corrosion pits. *Journal of Aircraft*, 51(3):805–810, 2014.

[84] M. Cerit, K. Genel, and S. Eksi. Numerical investigation on stress concentration of corrosion pit. *Engineering Failure Analysis*, 16:2467–2472, 2009.

[85] B.M. Schönbauer, S.E. Stanzl-Tschegg, A. Perlega, R.N. Salzman, N.F. Rieger, S. Zhou, A. Turnbull, and D. Gandy. Fatigue life estimation of pitted 12% Cr steam turbine blade steel in different environments and at different stress ratios. *International Journal of Fatigue*, 65:33–43, 2014.

[86] B.M Schönbauer, A Perlega, U.P Karr, D. Gandy, and S.E. Stanzl-Tschegg. Pit-to-crack transition under cyclic loading in 12% Cr steam turbine blade steel. *International Journal of Fatigue*, 76:19–32, 2015.

[87] R. Pérez-Mora, T. Palin-Luc, C. Bathias, and P.C. Paris. Very high cycle fatigue of a high strength steel under sea water corrosion: A strong corrosion and mechanical damage coupling. *International Journal of Fatigue*, 74:156–165, 2015.

[88] M.H. El Haddad, T.H. Topper, and K.N. Smith. Prediction of non propagating cracks. *Engineering Fracture Mechanics*, 11:573–584, 1979.

[89] Newman J.C. Jr. and I. Raju. Stress-intensity factor equations for cracks in three-dimensional finite bodies subjected to tension and bending loads. *Computational Methods in The Mechanics of Fracture*, 2:311–334, 1986.

[90] R. Salzman, N.F. Rieger, S. Stanzl-Tschegg, B. Schönbauer, A. Turnbull, S. Zhou, and D. Gandy. Corrosion-fatigue in steam turbine blades. In *Advances in Materials Technology for Fossil Power Plants: Proceedings from the Sixth International Conference 2010*, pages 450–469. ASM International, 2011.

[91] R. Salzman, D. Gandy, N. Rieger, B. Schönbauer, S. Tschegg, S. Zhou, and A. Turnbull. Corrosion-fatigue prediction methodology for 12% Cr steam turbine blades. In *Volume 1: Fuels and Combustion, Material Handling, Emissions; Steam Generators; Heat Exchangers and Cooling Systems; Turbines, Generators and Auxiliaries; Plant Operations and Maintenance.* ASME Power Conference, 2013.

[92] S. Zhou and A. Turnbull. Influence of pitting on the fatigue life of a turbine blade steel. *Fatigue & Fracture of Engineering Materials & Structures*, 22(12):1083–1093, 1999.

[93] J.T. Burns, J.M. Larsen, and R.P. Gangloff. Driving forces for localized corrosion-to-fatigue crack transition in Al–Zn–Mg–Cu. *Fatigue & Fracture of Engineering Materials & Structures*, 34:745–773, 2011.

[94] M. Cerit. Corrosion pit-induced stress concentration in spherical pressure vessel. *Thin-Walled Structures*, 136:106–112, 2019.

[95] A. Turnbull, L. Wright, and L. Crocker. New insight into the pit-to-crack transition from finite element analysis of the stress and strain distribution around a corrosion pit. *Corrosion Science*, 52:1492–1498, 2010.

[96] D.A. Horner, B.J. Connoly, S. Zhou, L. Crocker, and A. Turnbull. Novel images of the evolution of stress corrosion cracks from corrosion pits. *Corrosion Science*, 53:3466–3485, 2011.

[97] A. Turnbull, D.A. Horner, and B.J. Connolly. Challenges in modelling the evolution of stress corrosion cracks from pits. *Engineering Fracture Mechanics*, 76:633–640, 2009.

[98] T. Magnin. Fatigue crack initiation: Effect of environment. In J.K.H. Buschow, R.W. Cahn, M.C. Flemings, B. Ilschner, E.J. Kramer, S. Mahajan, and P. Veyssière, editors, *Encyclopedia of Materials: Science and Technology*, pages 2877–2882. Elsevier, Oxford, 2001.

[99] J.L. Chaboche. Time-independent constitutive theories for cyclic plasticity. *International Journal of Plasticity*, 2(2):149–188, 1986.

[100] P. Krolo, D. Grandić, and Ž. Smolĉić. Experimental and numerical study of mild steel behaviour under cyclic loading with variable strain ranges. *Advances in Materials Science and Engineering*, 2016:13, 2016.

[101] S. Mrozinski and M. Piotrowski. Effect of strain level on cyclic properties of S355 steel. *AIP Conference Proceedings*, 1780(02005), 2016.

[102] N. E. Dowling. Notched member fatigue life predictions combining crack initiation and propagation. *Fatigue of Engineering Materials and Structures*, 2:129–138, 1979.

[103] K. Ghahremani. *Fatigue Assessment of Repaired Highway Bridge Welds Using Local Approaches.* PhD thesis, University of Waterloo, 2015.

[104] NIOZ, Deltares, IMARES, and Rijkswaterstaat. De staat van de noordzee. Presented at Noordzeedagen, 2014.

[105] I. Hinrichs and V. Gouretski. Baltic and north sea climatology hydrographic part (version 1.0), 2018.

[106] B.Y. Queste, L. Fernand, T.D. Jickells, and K.J. Heywood. Spatial extend and historical context of north sea oxygen depletion in august 2010. *Biogeochemistry*, 113:53–68, 2013.

[107] Northwester 2 offshore wind farm. `https://www.nsenergybusiness.com/projects/northwester-2-offshore-wind-farm/`.

[108] Abaqus manual. `https://abaqus-docs.mit.edu/`.

[109] C.E. Inglis. Stresses in a plate due to the presence of cracks and sharp corners. *Transactions of the Institute of Naval Architects*, 55:219–241, 1913.

[110] S.-H. Ahn, F.V. Lawrence, and M.M. Metzger. Corrosion fatigue of an HSLA steel. *Fatigue & Fracture of Engineering Materials & Structures*, 15(7):625–642, 1992.

[111] M.A. Miner. Cumulative damage in fatigue. *Journal of Applied Mechanics*, 12:A159–A164, 1945.

[112] H.F.S.G. Pereira, A.M.P. de Jesus, A.S. Ribeiro, and A.A. Fernandas. Influences of loading sequence and stress ratio on fatigue damage accumulation of a structural component. *Science and Technology of Materials*, 20:60–67, 2008.

[113] D. Dewees. Ratcheting and cyclic plasticity considerations for code analysis. `https://www.lehigh.edu/~ak01/ratcheting/ratcheting.pdf`, 2013.

[114] E. Kullig, R. Rennert, M. Vormwald, A Esderts, and D. Siegele. *Analytical Strength Assessment of Components: Made of Steel, Cast Iron and Aluminum Materials in Mechanical Engineering*. FKM Guideline. 2012.

A

Plastic material properties

This chapter discusses the selection of the plastic material properties implemented in the corrosion fatigue model to describe the behaviour of hot-rolled S355 steel. The hardening model of Chaboche [99] is used in this study. This hardening model consists of two parts: (i) an isotropic part, and (ii) a kinematic part.

The isotropic part of the hardening model defines the change in size of the yield surface σ^0 given the equivalent plastic strain $\bar{\epsilon}^p$ and is expressed as

$$\sigma_0 = \sigma|_0 + Q_\infty \left(1 - \exp\left(-b\bar{\epsilon}^{\mathrm{p}}\right)\right) \tag{A.1}$$

where $\sigma|_0$ is the initial yield stress at zero plastic strain, Q_∞ is the maximum change in size of the yield surface and b the rate at which the yield surface size changes given the equivalent plastic strain. The material parameters Q_∞ and b are to be calibrated using cyclic stress-strain data from experiments.

The kinematic part of the hardening model defines the change in back stress α and can shift the hysteresis loop in total up and down. This part is expressed as

$$\begin{gathered} d\alpha = \sum d\alpha_i \\ d\alpha_i = \frac{C}{\sigma_0}\left(\sigma_i - \alpha_i\right) d\bar{\epsilon}^{\mathrm{p}} - \gamma\alpha_i d\bar{\epsilon}^{\mathrm{p}} \\ \text{for } i = 1,2,3 \end{gathered} \tag{A.2}$$

where C is the initial kinematic hardening factor, γ is the rate at which the kinematic hardening factor changes given a change in plastic strain. Chaboche proposed that the overall back stress can be computed by accumulating three back stresses.

Krolo et al. [100] calibrated the isotropic and kinematic parameters for hot-rolled S355 steel in air. Krolo et al. validated the calibrated hardening parameters by reproducing multiple experiments with a cyclic variable amplitude load in FEA. The hardening parameters are given in table A.1.

Parameter	Value	Unit
Change in size of the yield surface $\sigma\|_0$	386	MPa
Maximum change in yield surface size Q_∞	20.8	MPa
Rate in yield surface change b	3.2	-
Kinematic hardening factor C_1	5327	MPa
Rate of change in kinematic hardening factor γ_1	75	-
Kinematic hardening factor C_2	1725	MPa
Rate of change in kinematic hardening factor γ_2	16	-
Kinematic hardening factor C_3	1120	MPa
Rate of change in kinematic hardening factor γ_3	10	-

Table A.1: Chaboche hardening model parameters for S355 steel in air [100]

To verify the data of Krolo et al., a comparison of monotonic and cyclic stress strain curves of hot-rolled S355 steel from different papers is made. Because true stress and strain input is necessary for FEM calculations, all stress-strain relations are converted to true stress-strain relations using

$$\epsilon_{\text{true}} = \ln\left(1+\epsilon_{\text{eng}}\right) \tag{A.3}$$

$$\sigma_{\text{true}} = \sigma_{\text{eng}}\left(1+\epsilon_{\text{eng}}\right) \tag{A.4}$$

where ϵ_{true} and σ_{true} are respectively the true strain and stress and ϵ_{eng} and σ_{eng} are respectively the engineering strain and stress. Monotonic and cyclic stress-strain curves are found from the Chaboche hardening parameters of Krolo et al. by equation (A.5) and A.6 respectively, which result from (continued) integration [113].

$$\textbf{Monotonic curve} \qquad \sigma(\epsilon^{\text{p}}) = \sigma_0 + \sum_{i=0}^{3} \frac{C_i}{\gamma_i}\left(1-\exp\left(-\gamma_i \epsilon^{\text{p}}\right)\right) \tag{A.5}$$

$$\textbf{Cyclic curve} \qquad \sigma_{\text{a}}(\epsilon_{\text{a}}^{\text{p}}) = \sigma_0 + \sum_{i=0}^{3} \frac{C_i}{\gamma_i}\tanh\left(\gamma_i \epsilon_{\text{a}}^{\text{p}}\right) \tag{A.6}$$

Stress-strain data of hot-rolled S355 steel from four different papers is shown in figure A.1. All studies use different types of hot-rolled S355 steel or equivalent, but are comparable in material properties. A comparison of the alloy composition of the steels can be found in table 3.4. From the monotonic stress-strain curves of figure A.1a it can be found that the data of Krolo et al. corresponds reasonably with the experimental data of experiments by Ghahremani [103] and Mrozinski et al. [101], except for the overshoot and plateau that the data of Krolo et al. does not show. The experimental monotonic stress-strain data of De Jesus et al. [65] is found to be overestimating the stress with respect to the other curves for $\epsilon_{\text{true}} \geq 1\%$. From the cyclic stress-strain curves of figure A.1b, a greater spread can be found between the curves of Ghahremani and Mrozinski et al. The cyclic stress-strain curve of Krolo is located in between the curves of Ghahremani and De Jesus et al. Due to the large scatter between the stress-strain curves, no conclusion can be drawn with regards to the reliability of the Chaboche hardening parameters of Krolo et al. besides that it is in range with other stress-strain relations of hot-rolled S355 steel.

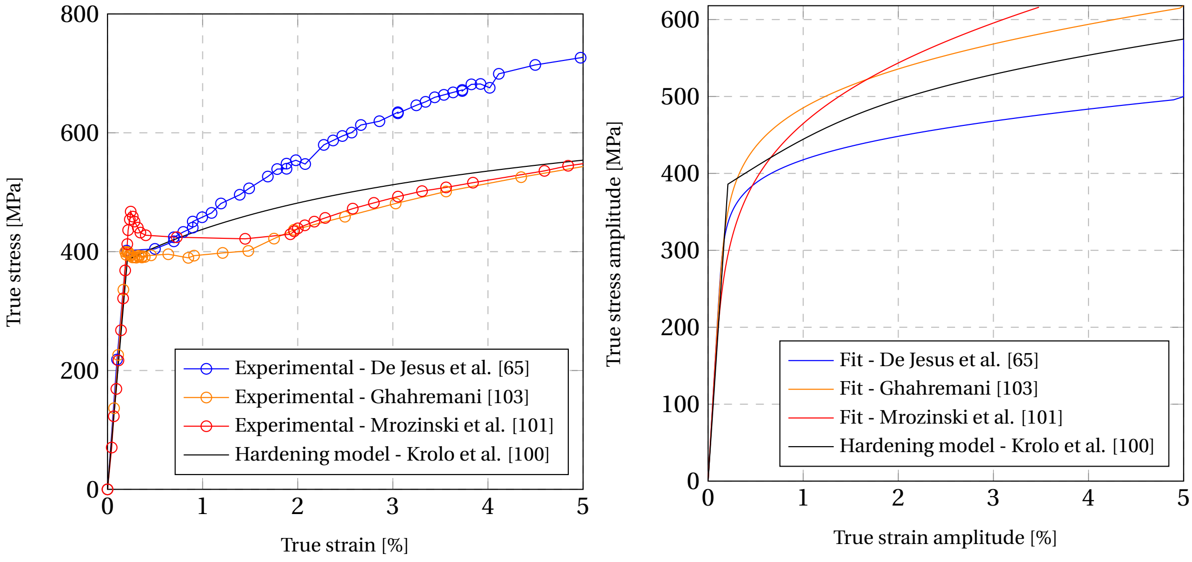

(a) Monotonic stress-strain curves in air

(b) Cyclic stress-strain curves for a fully reversed load

Figure A.1: Stress-strain curves

To validate the implementation of the hardening parameters in Abaqus and compare the Chaboche hardening model parameters of Krolo et al. to hysteresis curves of hot-rolled S355 steel of De Jesus et al., a simple beam model is used under a strain-controlled uniaxial fully reversed cyclic loading. The results for two strain ranges are shown in figure A.2, and show good comparison in the stress range. The shape of the hysteresis loops shows large differences. Since the strain-life method is used for determining the fatigue initiation life, and for this method only strain ranges and mean stress are used as input, this difference is assumed to have no impact.

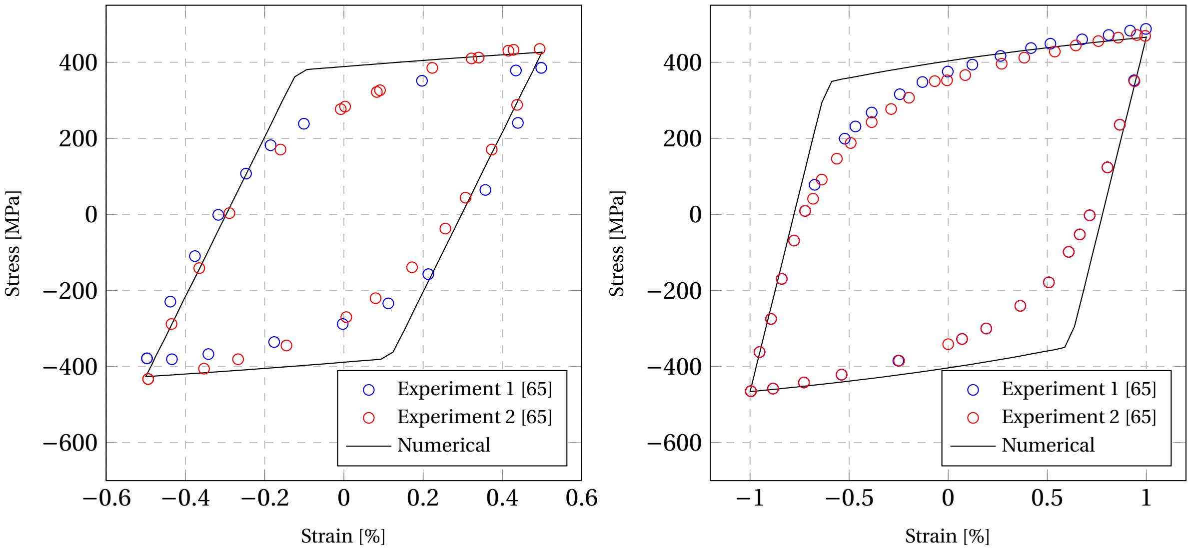

(a) Strain range $\Delta\epsilon = 1\%$

(b) Strain range $\Delta\epsilon = 2\%$

Figure A.2: Uniaxial strain-controlled data comparison of experiments with S355 steal by De Jesus et al. [65] and numerical FE results of a simple beam model

B

Fitting the Coffin-Manson-Morrow parameters

This appendix focusses discusses the fitting process and factorization of the strain-life curves used in this study. First the strain-life curves of hot-rolled S355 steel obtained from literature will be compared and discussed. Next, the factorization of the curves to compensate for the environment, and the definition of initiation (the fatigue crack length), is discussed.

It is expected that there is an influence of the corrosion process on the fatigue life of a specimen when pitting does not occur. This effect is expected to be due to hydrogen absorption, which causes embrittlement of the material. Therefore, preferably data of strain-life experiments in seawater (free corrosion conditions) or a NaCl-solution are used. Bignonnet et al. [76] performed experiments to obtain the strain-life curve in air as well as free corrosion. The experiments were ceased at crack initiation, which was measured using variation in the applied load, and by monitoring the change in the cathodic current. Bignonnet et al. claimed that crack initiation corresponds to a crack length of 0.1 mm using these methods. Note that, due to this corrosive environment, a certain surface roughness will be found on the surface of the specimens as well.

The data of Bignonnet et al. is the only retrieved source in which strain-life experiments using hot-rolled S355 steel are performed in free corrosion. Therefore, only the strain-life curve of Bignonnet et al. in air can be compared to others. Because the fatigue parameters given by Bignonnet et al. seem to be off compared to figure 2.12, the fatigue parameters are estimated. Figure B.1 shows the plastic and elastic part of the strain-life curves for different environment by Bignonnet et al. By laying a graph on top of this figure, the fatigue parameters of the curves are determined. For this study, only the curves for free corrosion and air are of importance. In table B.1 the Coffin-Manson-Morrow parameters are listed. Bignonnet et al. claimed that the elastic curve was equal for all environments, as can be seen in figure B.1. The corresponding strain-life curve is plotted in figure B.2, and the strain-life parameters are given in table B.2. From the graph it can be seen that the curve for air conditions shows good correspondence with the data points. The curve for free corrosion conditions shows less correspondence to the data points. Nevertheless, by absence of more data points and other strain-life experiments which include free corrosion conditions and hot-rolled S355 (equivalent) steel, this curve is used in this study.

Parameter	**Value**		**Unit**
	Air [76]	Free corrosion [76]	
Fatigue strength coefficient σ'_f/E	0.0051	0.0051	-
Fatigue ductility coefficient ϵ'_f	1.30	0.91	-
Fatigue strength exponent b	-0.126	-0.126	-
Fatigue ductility exponent c	-0.685	-0.683	-

Table B.1: Coffin-Manson-Morrow parameters fitted on data of Bignonnet et al.

Together with curves obtained from De Jesus et al. [65], Ghahremani [103], and Mrozinski et al. [101], the curves of Bignonnet et al. in air and free corrosion can be found in figure B.3.

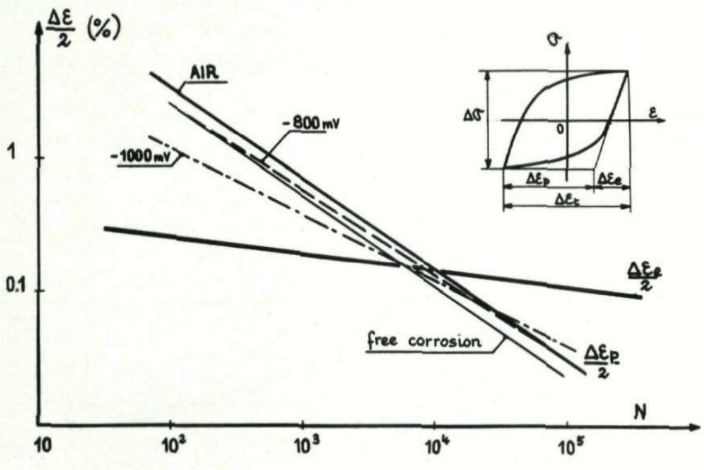

Figure B.1: Plastic and elastic part of the strain-life curve for different environments by Bignonnet et al. [76]

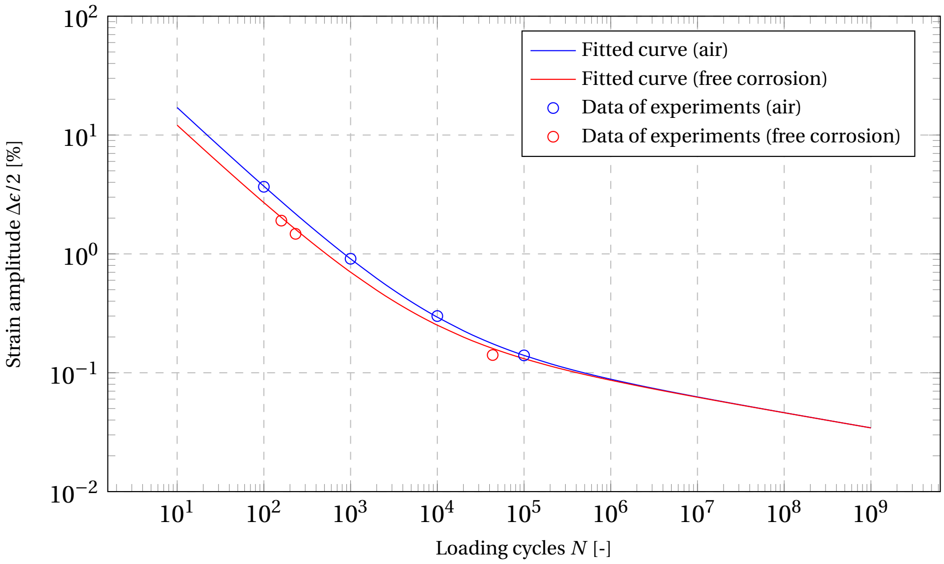

Figure B.2: Coffin-Manson relation fitted on data of Bignonnet et al. [76]

For the low- and medium-cycle fatigue range, most curves are in the same range, except for the strain-life curve of Bignonnet et al. Because the other three studies stopped the fatigue experiments at failure of the specimen, it is more remarkable that the fatigue life is larger for the strain-life curve of Bignonnet et al. for strains of $\epsilon \geq 0.1\%$.

In the medium-cycle fatigue region, all curves show overlap, where the curve of Bignonnet et al. has a different slope than the other three curves. In the high-cycle fatigue region, a significant scatter of all strain-life curves can be found. The strain-life curve of Bignonnet et al. is clearly most conservative of all curves. The high-cycle fatigue region is dominated by the elastic part of the strain-life relation, which is shown in equation (B.1).

$$\epsilon_{\mathrm{a}} \approx \epsilon_{\mathrm{a}}^{\mathrm{e}} = \frac{\sigma_{\mathrm{f}}'}{E}(2N_{\mathrm{f}})^{b} \tag{B.1}$$

Because strain-life curves are typically fitted on fatigue data in the low cycle fatigue region, where plasticity plays a significant role, the strain-life curve in the high cycle fatigue region can be unreliable. SN-curves are typically fitted on data of higher fatigue lives, and can therefore be more reliable in the high cycle fatigue region.

Figure B.4 shows the elastic part of all discussed strain-life curves in combination with the SN-curve for the matching circumstances according to the FKM guideline [114], and the mean B1-curve of the DNV GL

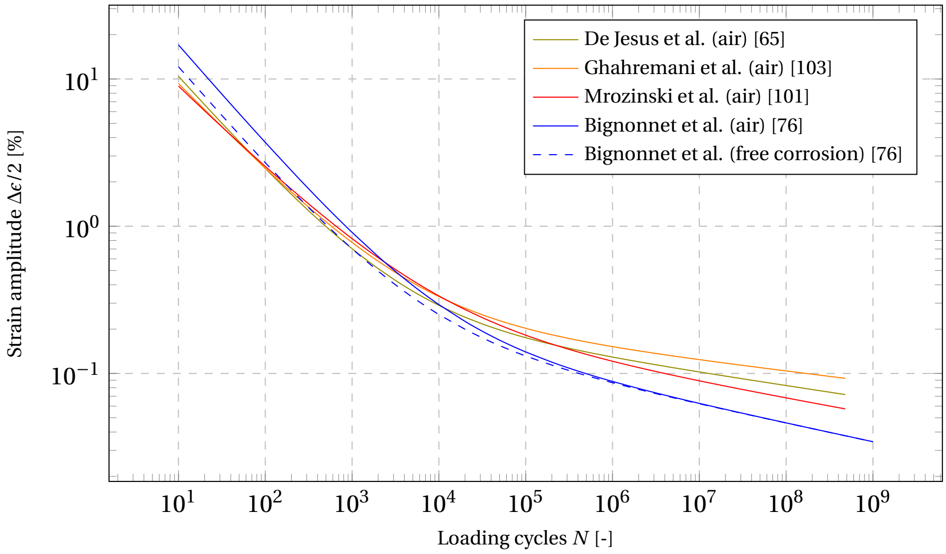

Figure B.3: Coffin-Manson relations for a fully reversed cyclic load

standard [66]. A stress ratio R of 0.5, and a roughness factor $K_{R,\sigma}$ of 0.83 has been applied to all curves excluding the mean B1-curve to be able to compare all curves in one figure. The roughness factor corresponds to an average roughness R_z of 50 μm for a tensile strength R_m of 540 MPa. The mean stress is taken into account in the Coffin-Manson-Morrow equation using the Smith-Watson-Topper stress correction, which is discussed in section 3.3. From the figure, it can be seen hat the FKM guideline does not correspond well to the B1-curve of DNV GL in the high cycle fatigue regime. This is because the FKM guideline does not elaborate on a variable amplitude load correction in the high cycle fatigue regime. To compensate for this, a slope of $m+2$ is adapted in the high cycle fatigue regime. A modified version of the SN-curve by the FKM guideline is added in the graph.

Even though the fraction of fatigue crack initiation life of the total fatigue life is large in the high cycle fatigue region, it should be kept in mind that the strain-life curves do not take (long) fatigue crack propagation into account, where SN-curves do. This means that the strain-life curves should be locate left of the SN-curves. The strain-life curves of Bignonnet et al. and Mrozinski et al. appear to correspond best to this criterion.

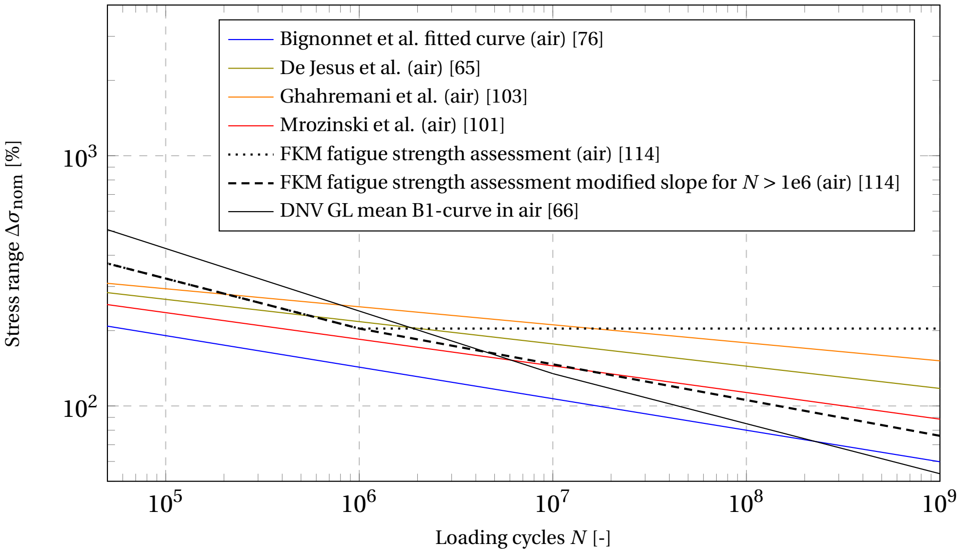

Figure B.4: Comparison between elastic part of strain-life curves and SN-curves

Because the data of Bignonnet et al. is found to be unreliable, especially in the low cycle fatigue region, a factor will be determined between the curves in air and free corrosion. The factor will be applied to the strain-life curve of Mrozinski et al., which was found to correspond well to the SN-curves given in figure B.4.

The elastic part of the strain-life graph of Bignonnet et al. is equal for both environments. Therefore a factor is determined for the plastic part of the strain-life graph only. It was found that the plastic strain amplitude was a factor of about 0.71 smaller in free corrosion for an equal number of cycles compared to air.

$$\begin{aligned} \Delta\epsilon^{\mathrm{p}}_{\text{free corrosion}} &\approx 0.71 \cdot \Delta\epsilon^{\mathrm{p}}_{\mathrm{air}} \\ \Delta\epsilon^{\mathrm{e}}_{\text{free corrosion}} &\approx \Delta\epsilon^{\mathrm{e}}_{\mathrm{air}} \end{aligned} \tag{B.2}$$

As mentioned in section 2.3.1.1, strain-life curves, which are determined based on experiments which are performed up to failure of the specimen, can be used to determine relatively large fatigue cracks for initiation. Dowling studied the crack lengths during fatigue experiments, and found that the fraction of fatigue initiation life of a fatigue crack of 0.076 mm can be as small as 10% of the total fatigue life in the low cycle fatigue region for A533B steel, which is comparable to S355 steel [59]. In a consecutive study for a higher strength steel, Dowling found that for a higher number of cycles to failure, the fraction $N_\mathrm{i}/N_\mathrm{f}$ increases [102].

Figure B.5 shows data points of the fraction $N_\mathrm{i}/N_\mathrm{f}$ for a crack length of 76 μm at the moment of initiation. The fractions are adapted from Dowling [102], but compensated for the steel type by decreasing the fractions so the lowest values equal 10%, which corresponds to the lowest fractions found for A533B steel [59]. Through these data points a linear curve is fitted. For strain-life fatigue experiments of over 50,000 cycles to failure, it is unknown what the fraction of initiation is. For this study, the assumption is made that the fraction of initiation life over the fatigue life until failure is maximal 0.7. This is a conservative assumption, because the total initiation life will rather be underestimated than overestimated using this assumption. A logistic function is fitted on the data to create a smooth transition to the fraction value of 0.7. The fitted function can be found in figure B.5.

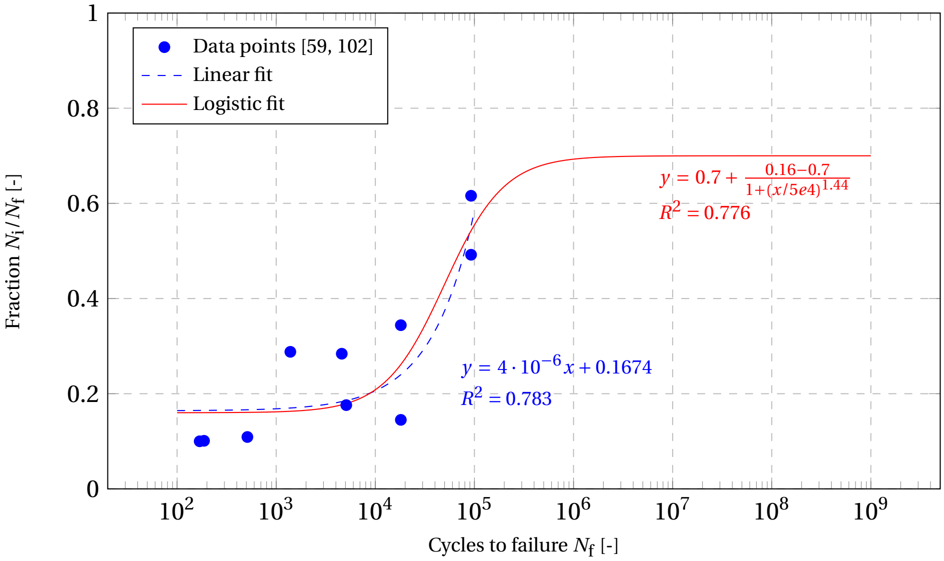

Figure B.5: Fraction of fatigue crack initiation life over total fatigue life for a range of fatigue lives

The strain-life curve that will be used in this study can be determined with all factors known. Because Mrozinski et al. do not give data points to which the strain-life curve is fitted, a set of points are generated from the strain-life curve. The strain values of the data points are multiplied with a factor to compensate for a corrosive environment accordingly equation (B.2). Next, the number of cycles of the data points are multiplied with a factor accordingly the logistic function of figure B.5. The resulting data points are shown in figure B.6. In the same graph the fitted functions of both the elastic and plastic part of the strain-life data are shown. The x-, and y-axis are switched, to ensure a correct fit using the least squares method.

The parameters of the fitted power functions from figure B.6 are converted to match the formulation of the Coffin-Manson-Morrow equation. The fatigue parameters for the strain-life curve are listed in table B.2, and the corresponding strain-life curves are shown in figure B.7. It can be seen that the factorization mostly has had an effect on the strain-life curve in the low cycle fatigue region.

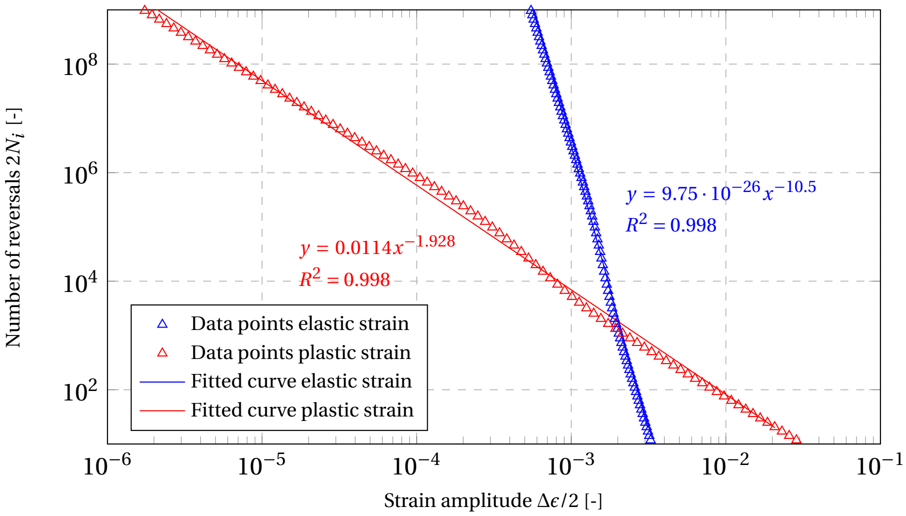

Figure B.6: Fitting elastic and plastic strain-life data

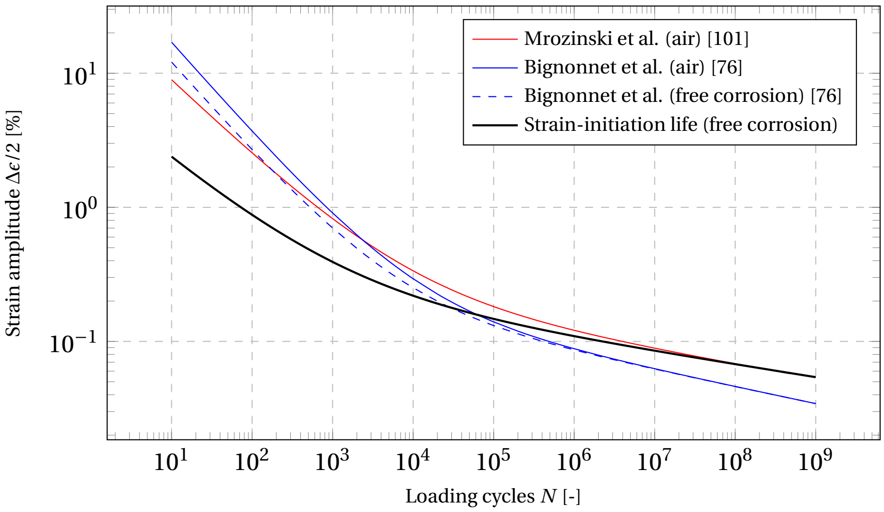

Figure B.7: Final strain-initiation life curve in combination with original strain-life curves

	σ'_f [MPa]	b [-]	ϵ'_f [-]	c [-]
Bignonnet et al. (air) [76]	1071	-0.126	1.30	-0.685
Bignonnet et al. (free corrosion) [76]	1071	-0.126	0.91	-0.683
Mrozinski et al. (air) [101]	1041	-0.1064	0.4865	-0.5796
Strain-initiation life (free corrosion)	838	-0.0952	0.0982	-0.519

Table B.2: Coffin-Manson-Morrow parameters of S355 steel

C

Results

In this appendix results of the corrosion fatigue model are listed, and several graphs of results are shown.

C.1. Linear corrosion fatigue results

In this section results of the linear corrosion fatigue calculations are shown. The number of cycles to, time to and pit depth at the moment of the pit-to-crack transition are listed in table C.1.

AR_p [-]	$\Delta\sigma_{nom}$ [MPa]	$\sigma_{nom,max}$ [MPa]	Location	a_{final} [mm]	N_i [-]	Time [years]
0.25	67.5	135.0	Pit bottom	2.7200	890142977	141.13
			Max. strain range	2.7200	891748996	141.39
	82.5	165.0	Pit bottom	2.6403	185533847	29.42
			Max. strain range	2.6397	185045889	29.34
	97.5	195.0	Pit bottom	2.0982	55446683	8.79
			Max. strain range	2.0952	55200589	8.75
0.5	50.0	100.0	Pit bottom	2.7200	2052281429	325.39
			Max. strain range	2.7200	2043010857	323.92
	67.5	135.0	Pit bottom	2.6836	244872439	38.82
			Max. strain range	2.6732	225507173	35.75
	77.5	155.0	Pit bottom	2.4861	112118598	17.78
			Max. strain range	2.4434	101653008	16.12
1.0	50.0	100.0	Pit bottom	2.7195	632107834	100.22
			Max. strain range	2.7153	420130222	66.61
	60.0	120.0	Pit bottom	2.6914	264021181	41.86
			Max. strain range	2.5823	147002748	23.31
	67.5	135.0	Pit bottom	2.5993	156045687	24.74
			Max. strain range	2.2665	72524007	11.50

Table C.1: Pit-to-crack transition results for elastic stress ranges

C.2. Non-linear corrosion fatigue results

In this section results of the non-linear corrosion fatigue calculations are shown. Table C.2 shows the locations of maximum strain range, maximum stress and minimum life for all aspect ratios and corresponding stress ranges. Of the pit bottom and maximum strain range location the maximum stress and strain range paths are given in figures C.1 to C.12. Figures C.1 to C.3 show the maximum stress along a path from the maximum strain range location at the pit surface into the material, figures C.4 and C.5 show the maximum stress along a path from the pit bottom into the material, figures C.6 to C.9 show the maximum strain range along a path from the maximum strain range location at the pit surface into the material, and figures C.10 to C.12 show the maximum strain range along a path from the pit bottom into the material. Table C.3 lists number of cycles, time and pit depth at the moment of the pit-to-crack transition for the non-linear calculations.

AR_p [-]	$\Delta\sigma_\mathrm{nom}$ [MPa]	$\sigma_\mathrm{nom,max}$ [MPa]	Location	$y_\mathrm{coordinate}/a_\mathrm{p}$ [-]	$\{x,z\}_\mathrm{coordinate}/a_\mathrm{p}$ [-]
0.25	125.0	250.0	Maximum strain range	0.145	1.982
			Maximum stress	0.994	0.220
			Minimum life	0.994	0.22
	137.5	275.0	Maximum strain range	0.145	1.982
			Maximum stress	0.992	0.257
			Minimum life	0.989	0.293
	150.0	300.0	Maximum strain range	0.145	1.982
			Maximum stress	0.967	0.512
			Minimum life	0.63	1.553
0.5	100.0	200.0	Maximum strain range	0.236	0.973
			Maximum stress	0.999	0.045
			Minimum life	0.580	0.815
	110.0	220.0	Maximum strain range	0.236	0.973
			Maximum stress	0.756	0.655
			Minimum life	0.458	0.889
	120.0	240.0	Maximum strain range	0.236	0.973
			Maximum stress	0.756	0.655
			Minimum life	0.458	0.889
1.0	80.0	160.0	Maximum strain range	0.220	0.488
			Maximum stress	0.365	0.931
			Minimum life	0.256	0.967
	90.0	180.0	Maximum strain range	0.220	0.488
			Maximum stress	0.577	0.817
			Minimum life	0.365	0.931
	503.0	200.0	Maximum strain range	0.220	0.488
			Maximum stress	0.543	0.84
			Minimum life	0.365	0.931

Table C.2: Investigated locations at pit surface of non-linear calculations

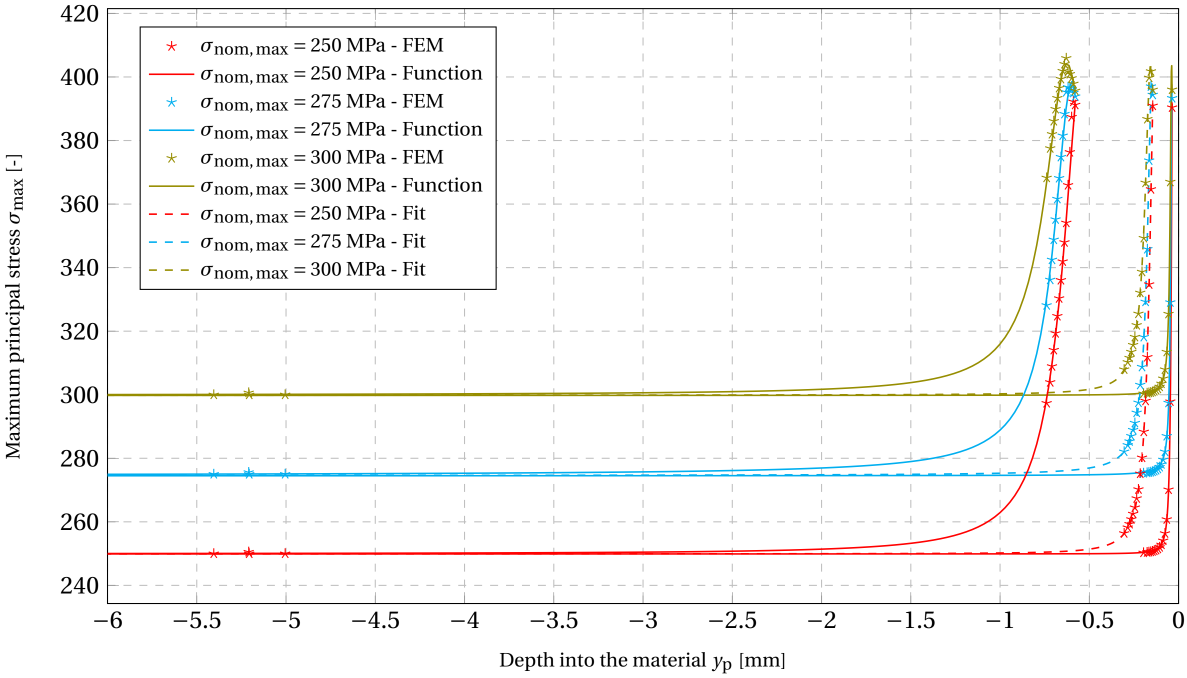

Figure C.1: Maximum principal stress along a path from the maximum strain range location into the material for $AR_{\mathrm{p}} = 0.25$

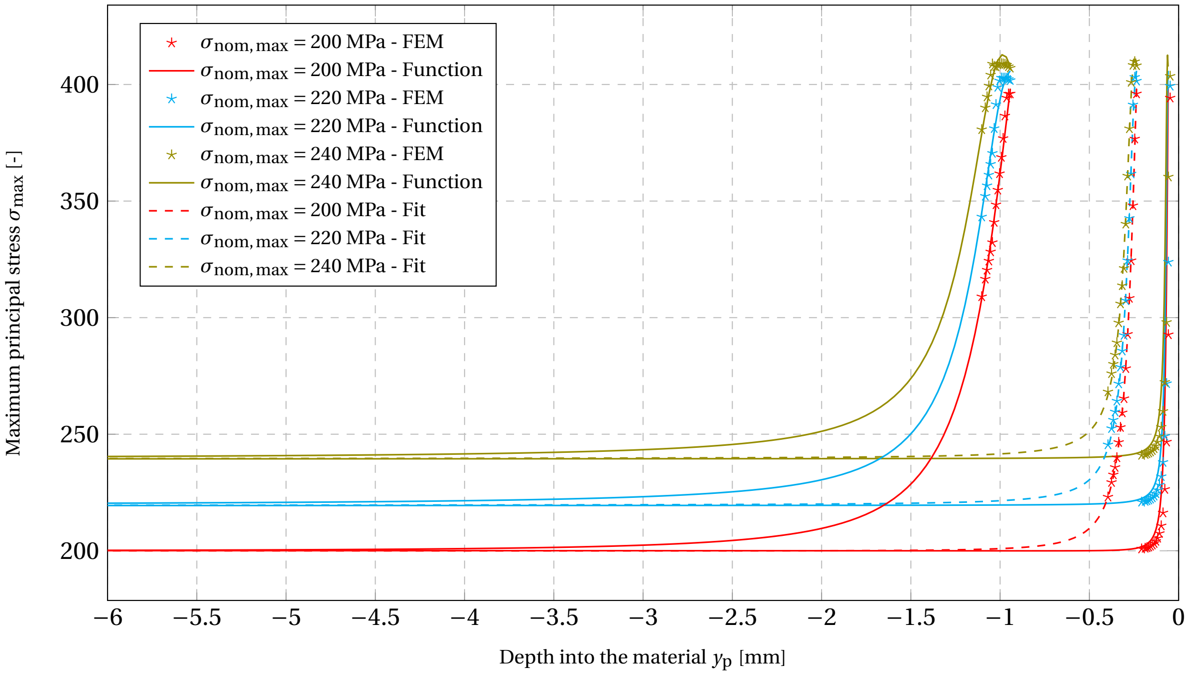

Figure C.2: Maximum principal stress along a path from the maximum strain range location into the material for $AR_{\mathrm{p}} = 0.50$

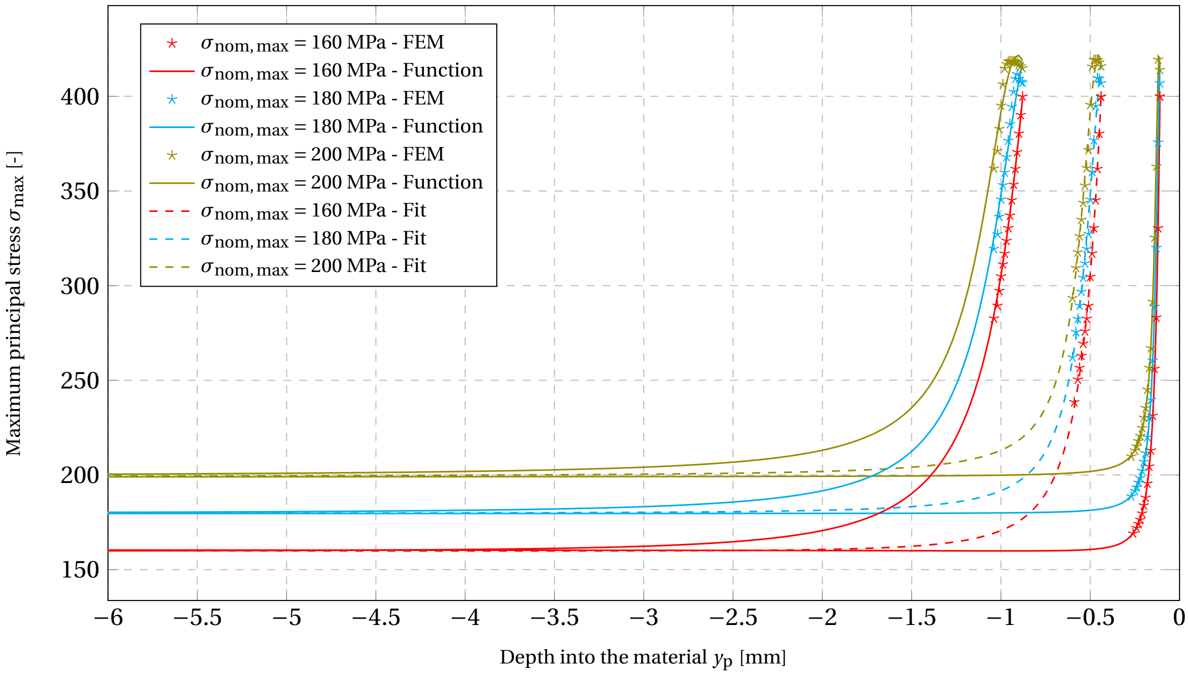

Figure C.3: Maximum principal stress along a path from the maximum strain range location into the material for $AR_{\text{p}} = 1.0$

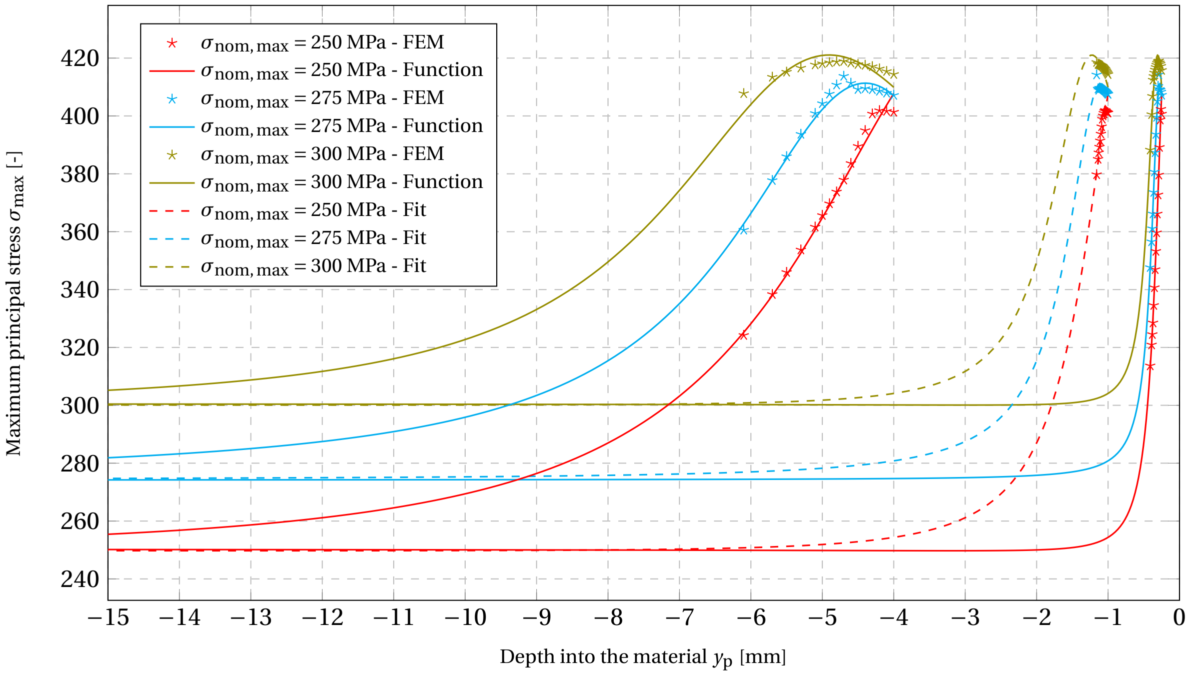

Figure C.4: Maximum principal stress along a path from the pit bottom into the material for $AR_{\text{p}} = 0.25$

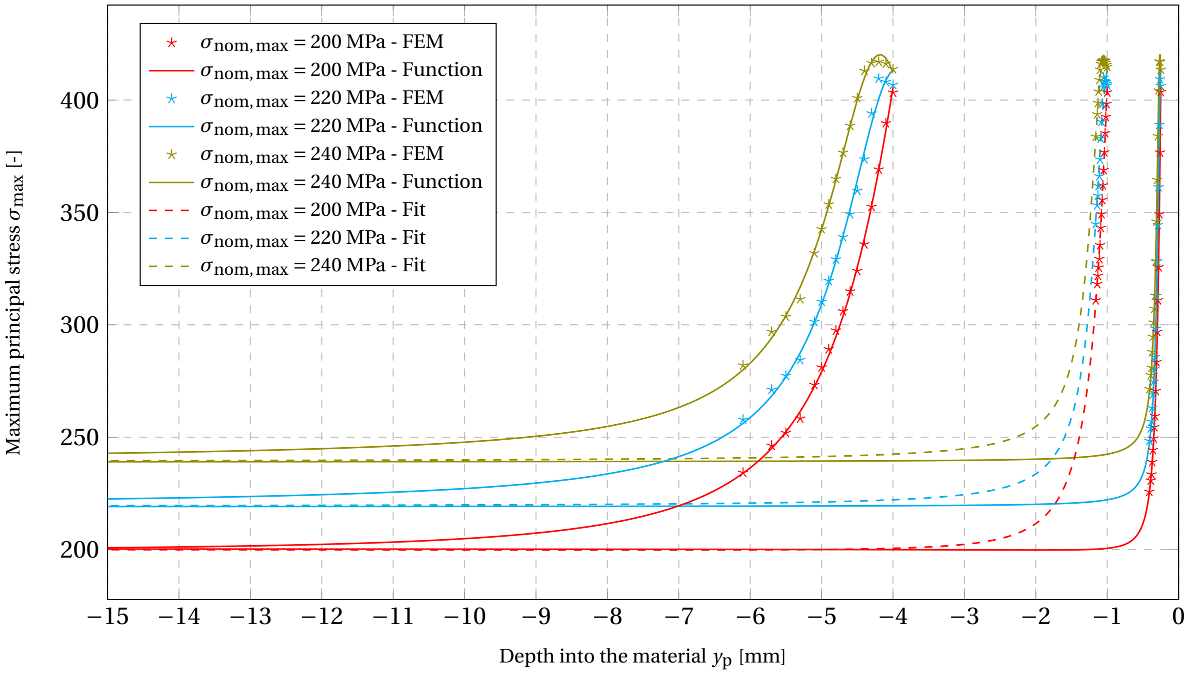

Figure C.5: Maximum principal stress along a path from the pit bottom into the material for $AR_{\text{p}} = 0.50$

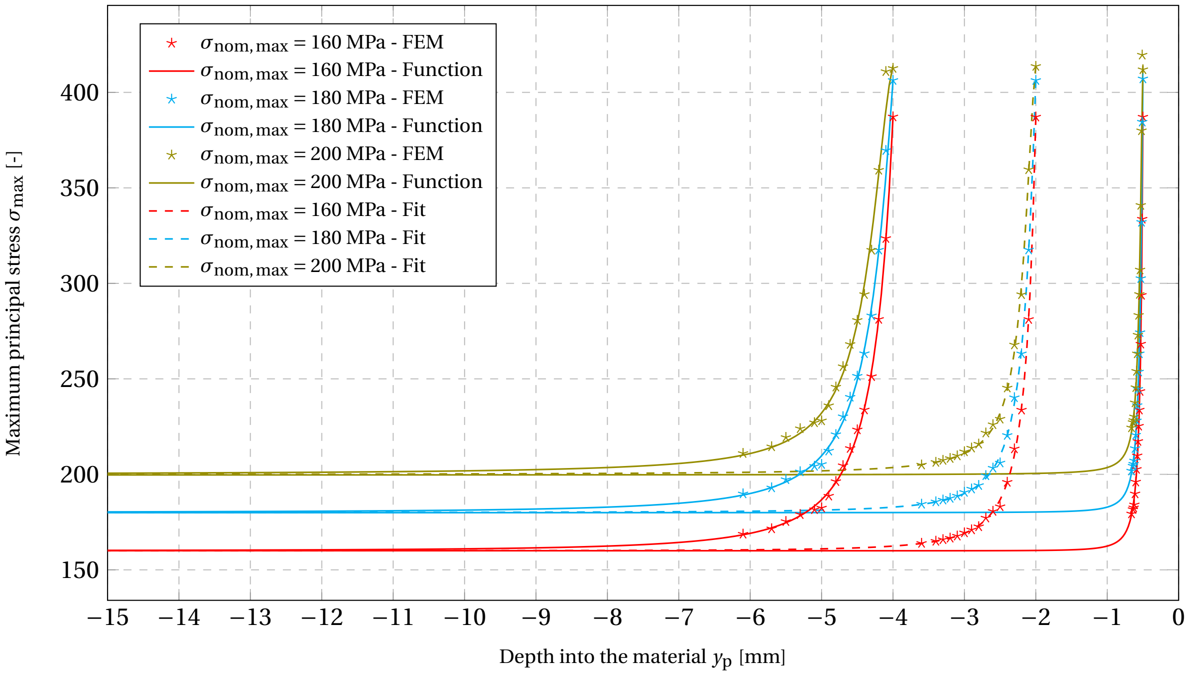

Figure C.6: Maximum principal stress along a path from the pit bottom into the material for $AR_{\text{p}} = 1.0$

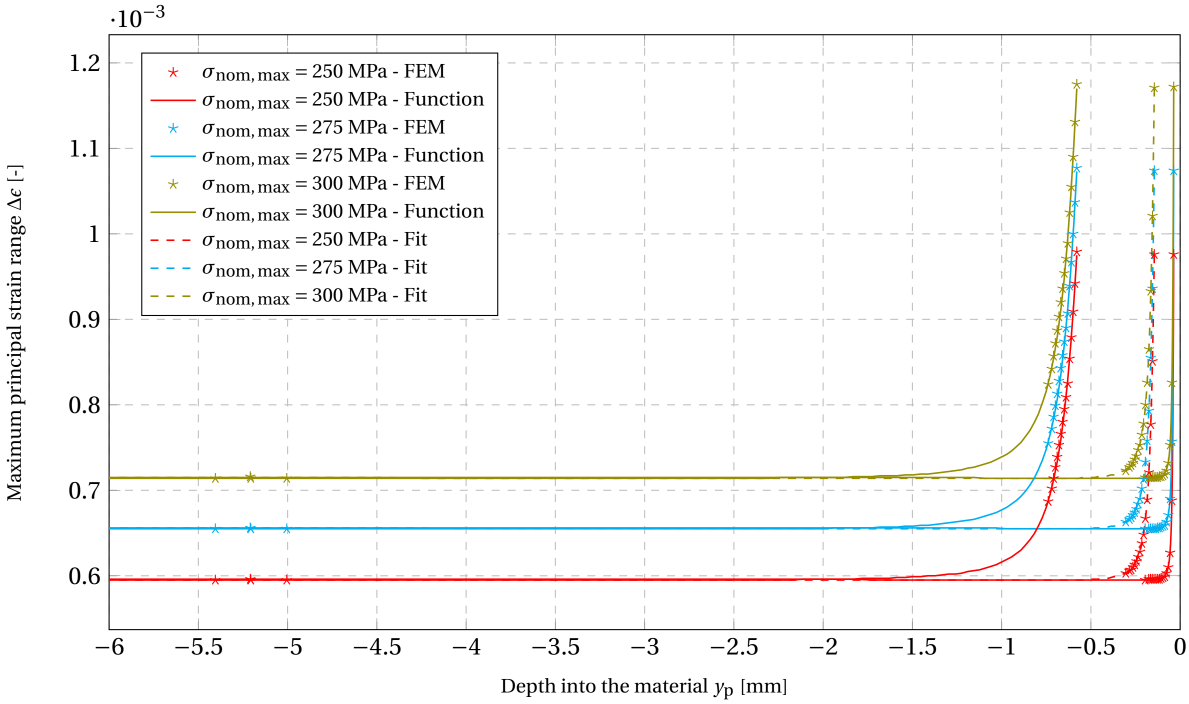

Figure C.7: Maximum principal stress along a path from the maximum strain range location into the material for $AR_p = 0.25$

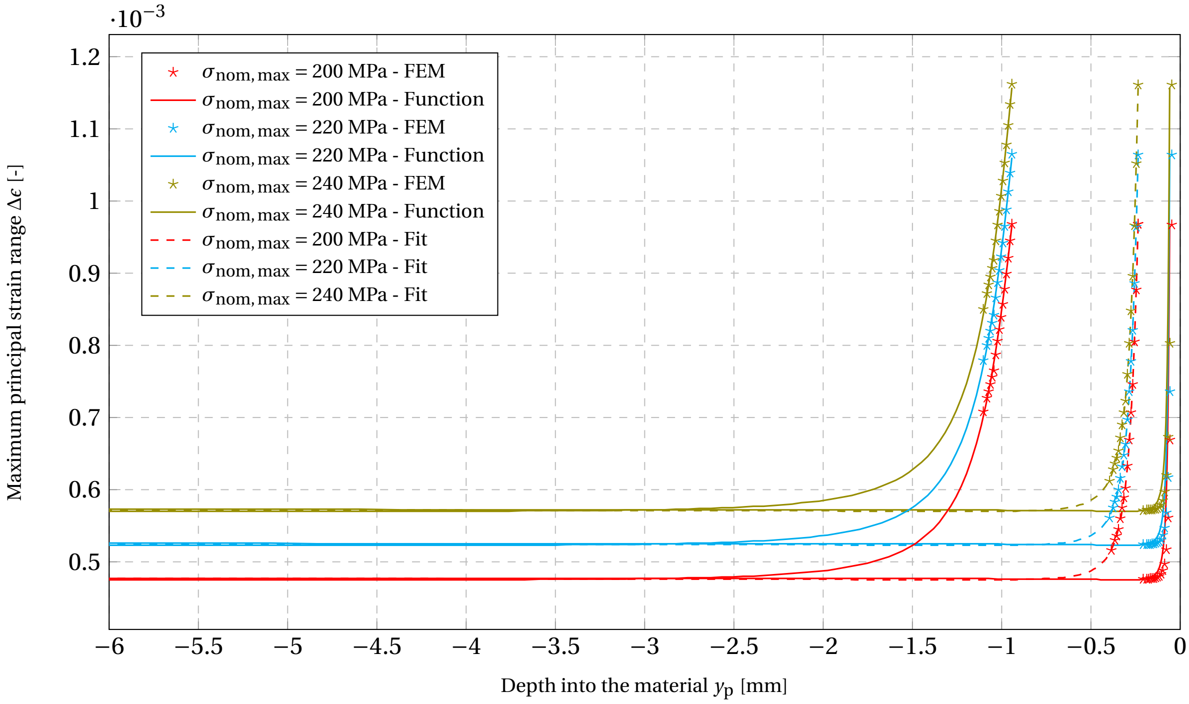

Figure C.8: Maximum principal stress along a path from the maximum strain range location into the material for $AR_p = 0.50$

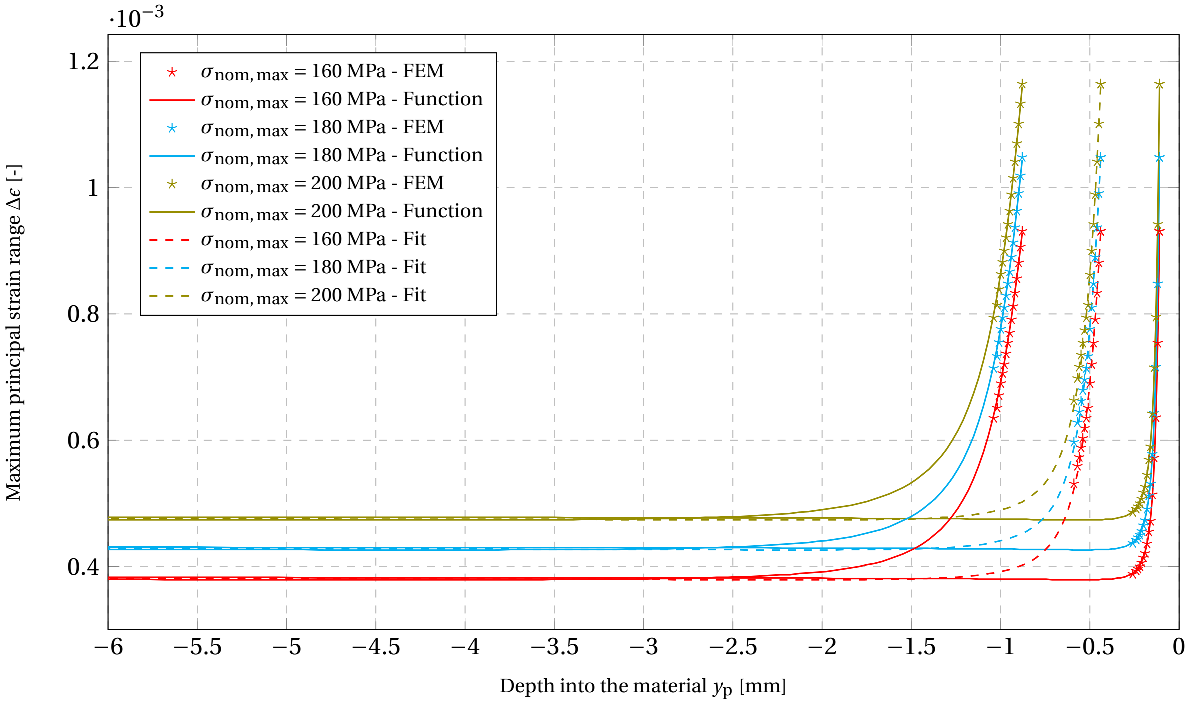

Figure C.9: Maximum principal stress along a path from the maximum strain range location into the material for $AR_p = 1.0$

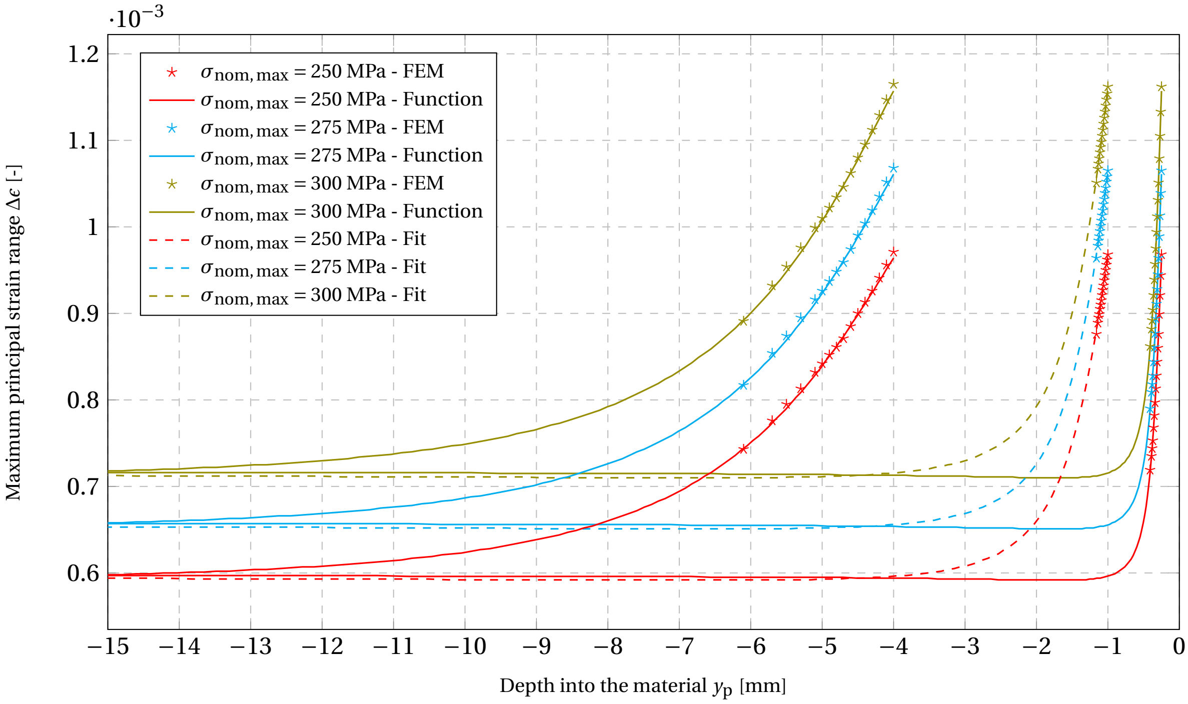

Figure C.10: Maximum principal stress along a path from the pit bottom into the material for $AR_p = 0.25$

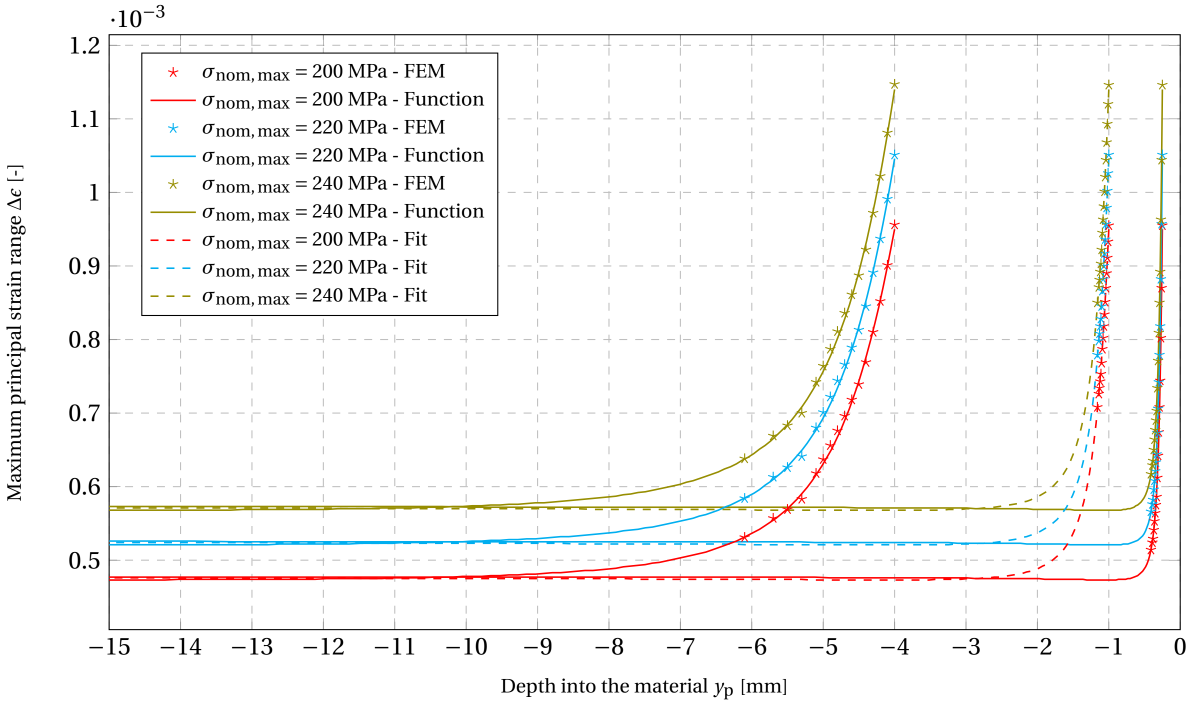

Figure C.11: Maximum principal stress along a path from the pit bottom into the material for $AR_\text{p} = 0.50$

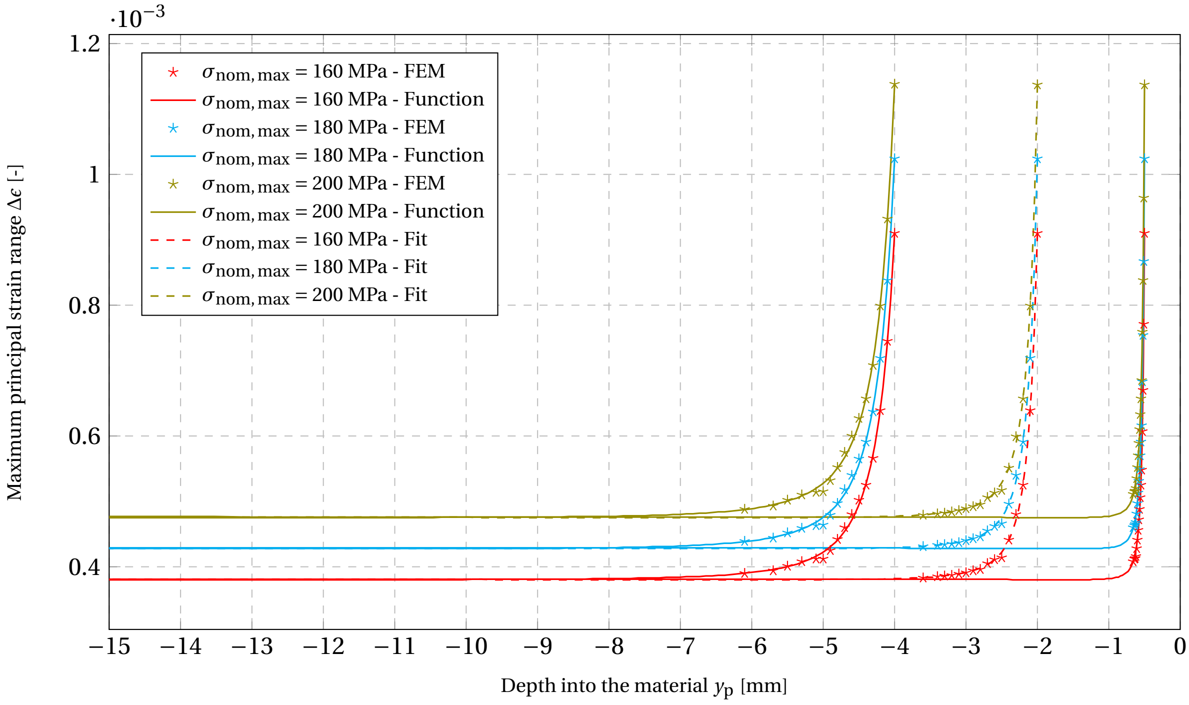

Figure C.12: Maximum principal stress along a path from the pit bottom into the material for $AR_\text{p} = 1.0$

AR_p [-]	$\Delta\sigma_\mathrm{nom}$ [MPa]	$\sigma_\mathrm{nom,\,max}$ [MPa]	Location	a_final [-]	N_i [-]	Time [years]
0.25	125.0	250.0	**Pit bottom**	**0.8127**	**7705139**	**1.22**
			Maximum strain range	1.2766	17191759	2.73
			Maximum stress	0.8158	7754178	1.23
			Minimum life	0.8158	7754178	1.23
	137.5	275.0	**Pit bottom**	**0.5229**	**3810034**	**0.60**
			Maximum strain range	0.8586	8447312	1.34
			Maximum stress	0.5264	3850059	0.61
			Minimum life	0.5274	3861028	0.61
	150.0	300.0	**Pit bottom**	**0.3588**	**2155041**	**0.34**
			Maximum strain range	0.6062	4798076	0.76
			Maximum stress	0.3674	2232215	0.35
			Minimum life	0.4645	3177972	0.35
0.5	100.0	200.0	Pit bottom	1.4216	21296034	3.38
			Maximum strain range	1.3956	20507346	3.25
			Maximum stress	1.4214	21287483	3.38
			Minimum life	**1.3908**	**20365005**	**3.23**
	110.0	220.0	Pit bottom	0.9882	10751054	1.70
			Maximum strain range	0.9725	10454573	1.66
			Maximum stress	0.9743	10488290	1.66
			Minimum life	**0.9591**	**10206531**	**1.62**
	120.0	240.0	Pit bottom	0.6944	5957344	0.94
			Maximum strain range	0.9725	10454573	1.66
			Maximum stress	0.6842	5817439	0.92
			Minimum life	**0.6739**	**5677058**	**0.90**
1.0	80.0	160.0	Pit bottom	2.2354	68834291	10.91
			Maximum strain range	**1.5886**	**26975126**	**4.28**
			Maximum stress	1.6257	28407135	4.50
			Minimum life	1.5959	27253054	4.32
	90.0	180.0	Pit bottom	1.8105	36700785	5.82
			Maximum strain range	**1.0453**	**11872869**	**1.88**
			Maximum stress	1.1793	14790605	2.35
			Minimum life	1.0658	12292924	1.95
	503.0	200.0	Pit bottom	1.3594	19451712	3.08
			Maximum strain range	**0.6897**	**5891866**	**0.93**
			Maximum stress	0.7727	7088266	1.12
			Minimum life	0.7043	6094769	0.97

Table C.3: Pit-to-crack transition results of non-linear calculations. In bold the minimum fatigue crack initiation life is indicated per applied stress range and aspect ratio.

C.3. Corrosion fatigue life results including surface roughness

This section discusses the results of the corrosion fatigue model including surface roughness in the form of a micro-pit. The calculations are performed for a corrosion pit aspect ratio of 0.50, and a micro-pit at the pit bottom only of three different sizes, where the aspect ratio of the micro-pit is constant ($AR_{\text{micro}} = 0.50$). Figures C.13 and C.14 respectively show the maximum strain range and stress path down into the material for an applied stress range of 120 MPa. Table C.4 lists the fatigue crack initiation life results corresponding to these stress and strain paths.

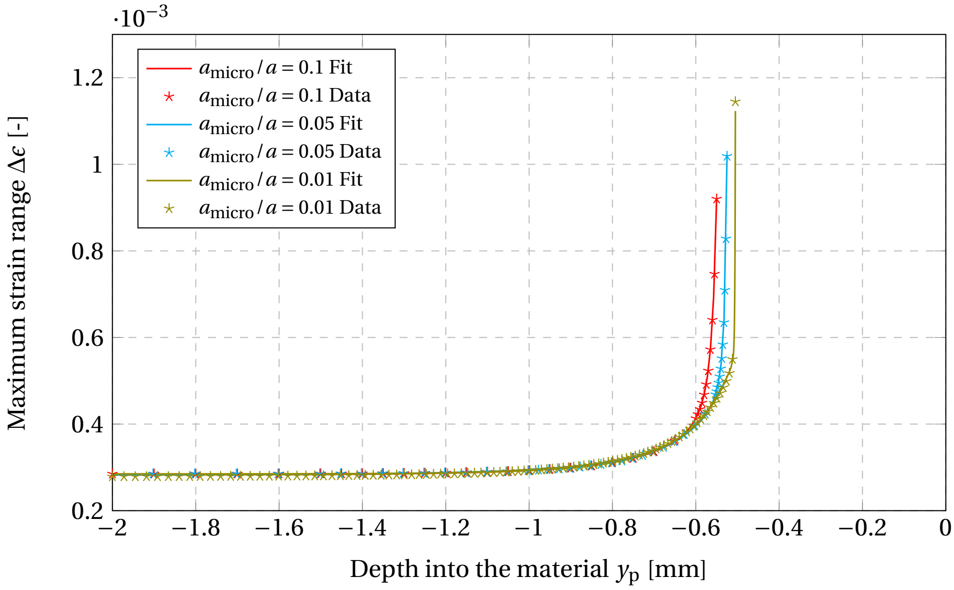

Figure C.13: Strain distribution along a path from the pit bottom into the material for a pit of aspect ratio $AR_p = 0.5$ and a pit depth $a = 0.5$ mm including and excluding a micro-pit at the pit bottom. For $\sigma_{\text{nom,max}} = 120$ MPa

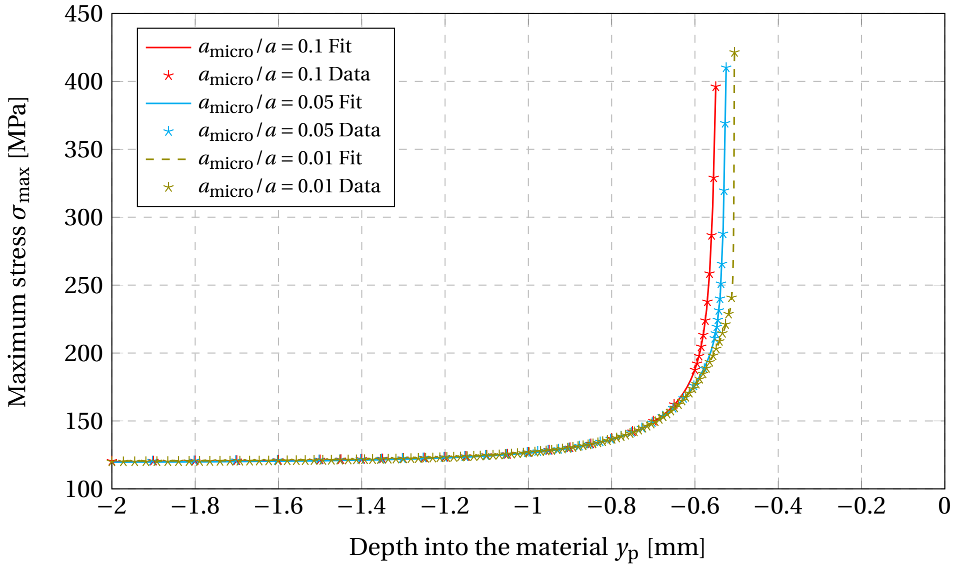

Figure C.14: Maximum stress distribution along a path from the pit bottom into the material for a pit of aspect ratio $AR_p = 0.5$ and a pit depth $a = 0.5$ mm including and excluding a micro-pit at the pit bottom. For $\sigma_{\text{nom,max}} = 120$ MPa

AR_p [-]	a_{micro}/a [-]	$\Delta\sigma_{nom}$ [MPa]	$\sigma_{nom,max}$ [MPa]	Location	a_{final} [-]	N_i [-]	Time [years]	Frequency [Hz]
0.5	0.01	37.5	75.0	Pit bottom	2.7169	260232810	41.26	0.2
		45.0	90.0	Pit bottom	2.6967	220310589	34.93	0.2
		60.0	120.0	Pit bottom	2.5597	136701057	21.67	0.2
		85.0	170.0	Pit bottom	1.6718	30284782	4.80	0.2
	0.05	37.5	75.0	Pit bottom	2.7170	149693374	23.73	0.2
		47.5	95.0	Pit bottom	2.6614	127126607	20.16	0.2
		60.0	120.0	Pit bottom	2.3954	91927113	14.57	0.2
		70.0	140.0	Pit bottom	1.9419	44132187	7.00	0.2
		85.0	170.0	Pit bottom	1.2368	16177680	2.56	0.2
	0.10	37.5	75.0	Pit bottom	2.7196	108510845	17.20	0.2
		50.0	100.0	Pit bottom	2.6637	96995696	15.38	0.2
		70.0	140.0	Pit bottom	2.0320	50254060	7.97	0.2
		85.0	170.0	Pit bottom	1.2784	17239653	2.73	0.2

Table C.4: Pit-to-crack transition results for a corrosion pit with an aspect ratio of $AR_p = 0.50$ including a micro-pit at the pit bottom.

D

Model files guide

This chapter will give guidance in the use of the developed corrosion fatigue model, including the workflow for the necessary files.

Figure D.1 shows the flowchart of figure 3.1, altered by including the corresponding scripts used to determine each step in the model. Of each of the scripts in the flowchart, a more extensive explaination is given in table D.1. Note that for the linear FEM calculations, different files are needed, than for the non-linear FEM calculations. Chapter 3 elaborates on the methods and implementations of the developed corrosion fatigue model.

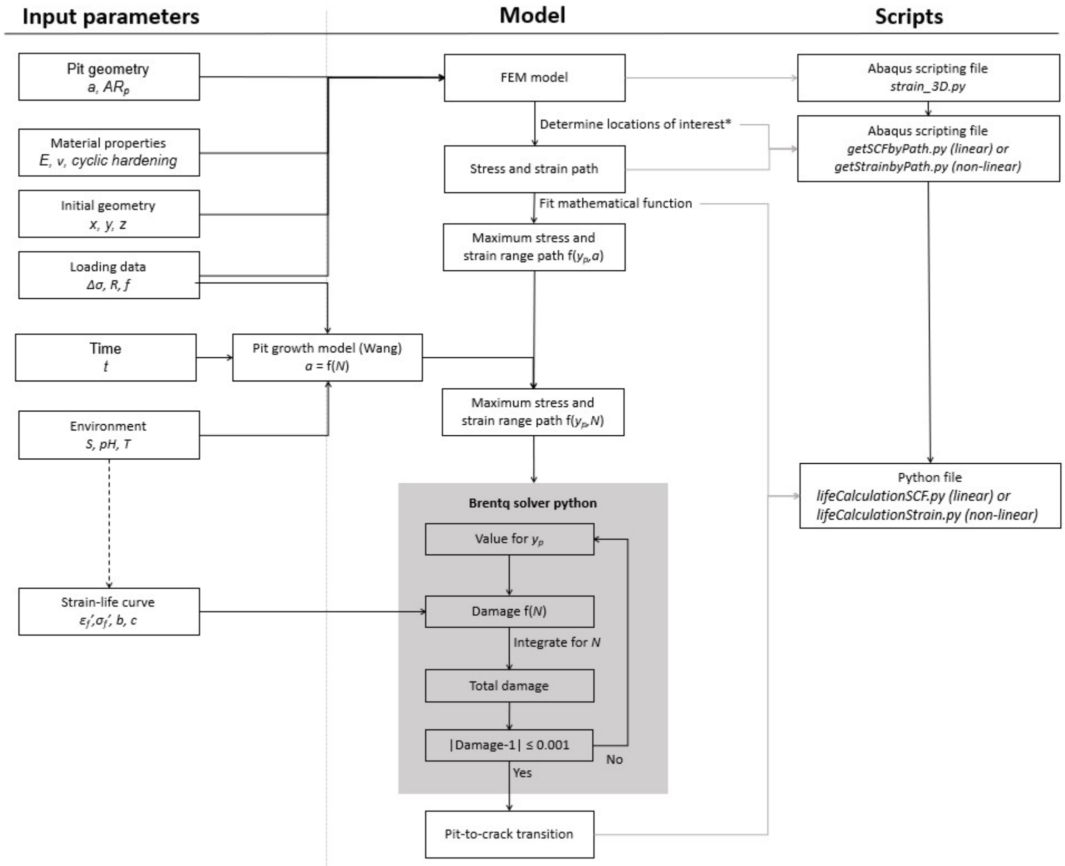

* Can also be found manually using Abaqus, and entering the locations in the script(s)

Figure D.1: Flowchart of the corrosion fatigue model including scripts

File name and type	Function	Output	Input
Abaqus scripting file *3Dmodel.py*	Creates a 3D FEM model of a rectangular plate including a corrosion pit, including mesh, loads, and boundary conditions. Creates an input (.inp) file for Abaqus calculations.	3D FEM model(s) of elliptical corrosion pits and .inp file(s) for calculations	• File storage location • Element type & size • Loading type (static/cyclic) • Calculation type (transient/direct cyclic) • Specimen size • Stress ratio & maximum applied stress (if direct cyclic) • Pit depth and width • Material behaviour parameters
Abaqus scripting file *getStrainbyPath.py*	Extracts the maximum stress and strain range for input in the strain-life equation including mean stress correction from a 3D FEM model (cyclic). The stress/strain levels are extracted from a location at the pit surface into the material. Also extracts the stress/strain distribution along the pit surface	.dat files including strain range and stress paths for all locations of interest of cyclic calculations. Also along the pit surface.	• File location of Abaqus 3D FEM model(s) • Pit depth and width • Type of stress or strain (principal, etc.) • Locations (pit bottom, maximum strain range, etc)
Abaqus scripting file *getSCFbyPath.py*	Works the same as the file getSTRAINbyPath.py, but now only for transient calculations with a static applied load of 1 MPa.	.dat files including stress paths for all locations of interest of static, transient calculations of 1 MPa. Also along the pit surface.	• File location of Abaqus 3D FEM model(s) • Pit depth and width • Type of stress or strain (principal, etc.) • Locations (pit bottom, maximum strain range, etc)
Python file *lifeCalculationSCF.py*	From the stress path, this script determines the maximum stress and strain range paths based on the stress ratio and maximum applied stress. Next, a mathematical function is fitted to these paths, and is used to determine the maximum pit depth and number of cycles until fatigue crack initiation for all locations in the corrosion pit of interest.	.dat files including fatigue crack initiation life prediction per aspect ratio and location in the corrosion pit. Also option to output .dat files including damage versus cycles curves.	• File location of .dat files including stress/strain paths • Pit depth and width • Loading type • Stress ratio & maximum applied stress • Fatigue parameters • Load frequency
Python file *lifeCalculationStrain.py*	A mathematical function is fitted to these paths, and is used to determine the maximum pit depth until fatigue crack initiation for all locations in the corrosion pit of interest.	.dat files including fatigue crack initiation life prediction per aspect ratio and location in the corrosion pit. Also option to output .dat files including damage versus cycles curves.	• File location of .dat files including stress/strain paths • Pit depth and width • Loading type • Stress ratio & maximum applied stress • Fatigue parameters • Load frequency

Table D.1: List of files used in the developed corrosion fatigue model